ANALYSIS INTO THE DECAYS OF
$$K^{\pm} \to \pi^{\pm}\mu^{+}\mu^{-} \ \text{ AND } \ B_c^{\pm} \to \phi K^{\pm} \text{ AT LHCb}$$

Kristian Zarębski

Thesis submitted for the degree of

Doctor of Philosophy

Particle Physics Group

School of Physics & Astronomy,

University of Birmingham

Abstract

This thesis outlines the contributions made by the author to the LHCbPR framework, part of the software validation and testing framework for the LHCb experiment at European Organization for Nuclear Research (CERN), and analyses into the rare decays of $K^\pm \to \pi^\pm \mu^+ \mu^-$ and $B_c^\pm \to \phi K^\pm$ with the LHCb detector.

The testing of LHCb software during development is vital to ensuring an efficient and optimal dataflow. LHCbPR allows quick and easy monitoring of the effects of software changes on the system through the orchestrated execution of a set of pre-written tests the results of which are then displayed online. Three such tests, which monitor physics processes during the development of the simulation frameworks, have been migrated by the author from being offline user run scripts to becoming fully automated within LHCbPR.

The decay of $K^\pm \to \pi^\pm \mu^+ \mu^-$, although having been observed previously by other experiments, is investigated within this thesis to determine the prospects of a first observation within a collider experiment, and for the purpose of looking into the prospects of performing a more precise measurement in the future. Analysis is performed making use of the $3.6\,\mathrm{fb}^{-1}$ collected from 13 TeV collisions at LHCb between 2015–2017, where additional improvements in triggering have been implemented to record events with lower p_T such as those of rare kaon decays. A measurement for the branching ratio of the decay of $\mathcal{B}(K^\pm \to \pi^\pm \mu^+ \mu^-) = (6.3 \pm 2.6) \times 10^{-8}$ was recorded, compatible within 1σ to the world average of $(9.4 \pm 0.6) \times 10^{-8}$. The results, although not yet competitive, hint that with the predicted levels of improvement at LHCb in Run 3, the experiment could indeed contribute to the future of kaon decay measurement.

Decays of the B_c^+ meson are yet to be well understood with very few measurements having been performed into their decay. Within this thesis is also outlined a dedicated search of the channel $B_c^\pm \rightarrow \phi K^\pm$ is performed using the $3.2\,\text{fb}^{-1}$ of Run 1 data collected between 2011 and 2012. Using theoretical prediction for the comparison of the B_c^+ meson with the more understood B^+, and the analogous channel of $B^\pm \rightarrow \phi K^\pm$ as a control, a maximum threshold of

$\mathcal{B}(B_c^\pm \rightarrow \phi K^\pm) \lesssim (9.3 \pm 4.4) \times 10^{-7}$ has been measured which matches Standard Model prediction.

Acknowledgements

Author's Contributions

The author's work consists of two separate physics analyses and the implementation of validation tools as part of the LHCb software testing framework. The GAUSS and GEANT4 packages were the frameworks within which these validation tests which carried out and then automated using the evolving LHCbPR system. Performance of these tests and their maintenance to ensure both forward and backward compatibility between software versions were an integral part of the author's responsibility.

The investigation to determine the potential for $K^{\pm} \to \pi^{\pm} \mu^+ \mu^-$ using LHCb evolved from a summer student project in 2015 using Run 1 data supervised by Dr. Francesco Dettori. The analysis was subsequently taken over by the author. The framework and tools for performing the analysis were created and tested using data from Run 1. Due to the limitations of triggering using data from both Run 1 and the first year of Run 2, the measurement of the branching ratio of $K^{\pm} \to \pi^{\pm} \mu^+ \mu^-$ was performed using 2016 and 2017 data. The author developed the event selection, using insight from related analyses and and advice from colleagues, including training, testing and evaluating the performance and stability of the multivariate classifiers. For $B_c^{\pm} \to \phi K^{\pm}$, the author presents an initial study which concludes with an estimation for the likely statistical yield for Run 1.

The pre-selection cuts for the data samples for measurements of $K^{\pm} \to \pi^{\pm} \mu^+ \mu^-$ and $B_c^{\pm} \to \phi K^{\pm}$ are defined within the LHCb software. The options defined to create

the relevant *Monte Carlo* (MC) samples were already available, with the exception of the 'TightCut' MC options written by the author, which were adapted from other analyses. Optimisations to enhance signal and suppress background were performed by the author. All offline analysis was the author's own work with advice from members of LHCb within the University of Birmingham advice and Dr. Dettori.

Contents

List of Figures

List of Tables

Glossary

BDT Boosted Decision Tree - a type of classifier consisting of a tree of cuts in chosen variables through which events are passed to categorise them.

Boole Gaudi based application used to convert simulated data into a form comparable to real data.

Brunel Gaudi based application which performs reconstruction on events using track and vertex information.

DaVinci Gaudi based application used to perform selection of candidates through stripping and decay matching.

DIRA The DIRection Angle is the angle between the direction of the reconstructed momentum of a particle and the direction between the measured primary and secondary vertices.

DOCA The distance of closest approach between two particles.

Downstream Tracks Tracks with hits in the tracking stations but not within the VELO.

EvtGen Implements QED corrections into the events generated by Pythia for B meson decays.

Gaudi Framework consisting of a Python frontend for customised running of C++ tools on data and Monte Carlo.

Gauss LHCb event simulation application for Monte Carlo production which combines the output of generators such as PYTHIA with GEANT4 within the LHCb geometry.

Geant4 GEometry ANd TRacking framework for simulating particles within materials.

HLT High Level Trigger - software trigger level.

LHCbPR LHCb Progress & Regression framework used to display the results during validation of the experiment software.

LoKi The Loops and Kinematics computational framework for obtaining properties of particles and composites in events.

Long Tracks Tracks with a decay vertex measured within the VELO and hits in the tracking stations.

Moore Gaudi based application which handles the trigger information and applies the online software based triggering.

PID Particle Identification system at LHCb.

ProbNNx A PID variable constructed via a Neural Network to describe the probability that a particle is of type x.

PS Preshower Detector used to separate out charged hadrons from electrons and photons.

Pythia Event generator used to simulate LHC collisions for Monte Carlo data.

Pythia Configurable Monte Carlo generator for the simulation of particle collisions within a collider environment.

RICH Ring Imaging Cherenkov detector in which particles are identified based on their momentum.

SPD Scintillator Pad Detector positioned prior to the calorimeters.

Stripping Pre-selection cuts applied to data before being available offline.

Trigger On Signal (TOS) Trigger event category for events which would still be triggered with only the signal candidate components.

Trigger Independent of Signal (TIS) Trigger event category for events which would still be triggered even without the signal candidate components.

Turbo Data readout system in which events are read directly from trigger lines.

VELO The LHCb Vertex Locator positioned around the beam interaction point which measures secondary decay vertices.

Chapter 1

Introduction

Since its conception in the 1960s the Standard Model (SM) of particle physics has provided a solid theory in its description of the interactions between fundamental particles. With the recent discovery of the Higgs boson at a mass of $M_H = (125.18 \pm 0.16)\,\text{GeV}/c^2$ by the ATLAS and CMS experiments at CERN [2] [3], the model is now largely complete in terms of components, and has yet to be dis-proven by experimental observation. However despite being itself complete the theory still falls short on answering some key questions, such as the reason behind the values of universal constants and understanding the physics behind why only three particle generations have been observed.

In the late 1940s the discovery of the kaon meson gave rise to the inclusion of a new subspecies of particles characterised by a property known as 'strangeness' [4]. The nomenclature refers to the observation that these particles are produced in high abundance within collision events, but possess a longer lifetime than expected. Later research deduced this property to be related to the constituents of the particles which led to postulation of the existence of the second generation of quarks.

Analysis of kaons also led to the discovery of CP violation in 1964 from the observation of neutral kaon decays. As all CP violation is not fully explained by SM theory it has sparked much interest in probing the new physics sector, and could also hold the answer to explaining another unknown, the asymmetry between matter and antimatter in the universe. In 2001 further direct evidence of CP violation was found in the decays of neutral B mesons at the BaBar and Belle experiments [5] motivating the design and construction of a dedicated hadronic b-factory as one of the four main experiments along the Large Hadron Collider (LHC), LHCb.

Due to their short lifetime decays of the charmed b-meson, B_c^+, are not as understood as those of B^+ with very few direct searches having been performed to measure these channels. The decay of $B_c^\pm \to \phi K^\pm$ is an example with there being a range of branching ratio estimates based on different theoretical models and techniques. A measurement for the analogous decay of $B^\pm \to \phi K^\pm$ has been performed by the BaBar, Belle and CDF collaborations opening up the possibility of not only using this channel as a normalisation for the rarer decay search, but also allowing for a direct comparison of the properties of B_c^+ and B^+.

After completion of Run 1 at the Large Hadron Collider (LHC) at the end of 2012, the decision was made to investigate the potential of the LHCb detector beyond the design motivations. Although the detector decay volume of LHCb is considerably less than dedicated kaon experiments such as NA62, the advanced Particle Identification (PID) system and high precision of the experiment open up the possibility of measuring kaon decays of which the Flavour Changing Neutral Current (FCNC) process of $K^\pm \to \pi^\pm \mu^+ \mu^-$ is an example under investigation. The current measurement of the channel has been performed with a fixed target setup in which a proton beam is collided with a stationary material. The higher production rates at the LHC motivate measurements also at LHCb to complement those being performed by NA62.

This thesis is presented in four main sections. In chapter 2 a general overview of the theoretical framework and mechanisms of the Standard Model is given, along with a summary of CP violation. The LHCb detector is outlined in chapter 3 with a description of all the main components and the software based tools used to perform event selection and analyses given in section 3.1. In section 3.5 the procedure for simulating the detector for the production of MC data is described, and the newly created software monitoring interface of LHCbPR2 is introduced with details given on the physics motivations and composition of the progress and regression tests maintained by the author.

Two analyses are presented within this thesis.[1] In chapter 4 the analysis into the rare strange decay of $K^{\pm} \to \pi^{\pm}\mu^{+}\mu^{-}$ is presented as contribution towards the strange physics programme at LHCb. Firstly the physics behind FCNC decays is described, addressing also the theory behind the search for Lepton Number Violating 'wrong sign' decays, in section 4.1. Then the analysis procedure into obtaining a measurement of a branching ratio for $K^{\pm} \to \pi^{\pm}\mu^{+}\mu^{-}$ using the data collected by the LHCb experiment in the years 2015–2017 is presented in section 4.2, also with reference to an initial study performed beforehand on 2011–2012 Run 1. Later in section A.1 a small study into the creation of an opposite side tagging algorithm for K^{0} mesons based on existing algorithms for B^{0} mesons is presented. The purpose being to extend the scope of LHCb research into indirect measurements of K_{L} decays.

Finally in chapter 5 the analysis of $B_{c}^{\pm} \to \phi K^{\pm}$ for the first measurement of a branching ratio is detailed using 2011–2012 data, the addition of such measurements allows a comparison to be made between the decay rates of $B_{c}^{\pm}$ channels with the

---

[1]Both of these analyses have been performed 'blinded'. This means the framework for obtaining measurements was constructed with all information relating to signal yield (i.e. mass distribution, number of signal events and parameters of fit models within the signal region) being hidden from the analyst, so as to avoid any human bias. Once the framework was tested and optimised the data were then unblinded for final measurements. Unless otherwise stated, charge conjugation is implied throughout.

analogous $B^{\pm}$ decays which have already been observed. With the availability of 2015–2017 data but lack of MC for these years, an overview of future measurement of the channel is also presented beyond Run 1.

Conclusions are then made in chapter 6 and the future of the analyses covered is addressed with reference to the upgrades to LHCb proposed for Run 3.

Chapter 2

Theoretical Framework

2.1 The Standard Model

The Standard Model of Particle Physics (SM) is the current accepted description of fundamental particles and their interactions. All particles are split into two categories defined by the *spin* principal quantum number, *fermions* having half integer spin and *bosons* integer spin.

Fermions form the 'building blocks' for all types of matter and are broken down further into *quarks* and *leptons*, they follow Fermionic statistics, and the Pauli exclusion principal which forbids any two sharing the same quantum state. In their natural state quarks are bound together into either $q\bar{q}$ *meson* (such as the kaon) or qqq *baryon* (like the proton) states. The SM is structured into three generations of fermions with increasing mass across the generations, each particle also having a corresponding anti-particle. A generation contains an 'up-like' and 'down-like' quark pair with $+\frac{2}{3}$ and $-\frac{1}{3}$ charge respectively, as well as a lepton and its respective neutrino as shown in Table 2.1. At the scale of high energy physics

currently accessible experimentally, the interactions between fermions are dominated by three of the four main fundamental forces in nature: the *weak* force, the *strong nuclear* (or *strong*) force and the *electromagnetic* force. A quantisation model of the *gravitational* force has yet to be developed, however the predicted strength in comparison to the weak force is 10^{-42} in magnitude rendering any effects to be negligible on the scales of those investigated within high energy physics.

The mediators for the three significant fundamental forces are the gauge bosons summarised in Table 2.2. The electromagnetic force, mediated by the photon, couples to charge and such processes are described by Quantum Electrodynamics (QED), examples including pair production and annihilation.

The SM is a non-Abelian gauge theory with a symmetry group in the form $SU(3)_C \otimes SU(2)_L \otimes U(1)_Y$ [6] which is spontaneously broken by the Higgs mechanism, and it is through this symmetry-breaking that fermions and the weak gauge bosons obtain their mass. The exact mechanism through which neutrinos acquire mass is still uncertain [7].

Table 2.1: The Standard Model of particle physics showing the three generations of fermions.

		Generation			Charge
		I	II	III	
Fermions	Quarks	u Up	c Charm	t Top	$+\frac{2}{3}$
		d Down	s Strange	b Bottom	$-\frac{1}{3}$
	Leptons	e Electron	μ Muon	τ Tau	-1
		ν_e Electron Neutrino	ν_μ Muon Neutrino	ν_τ Tau Neutrino	0

Table 2.2: The gauge boson mediators of the three significant forces within the Standard Model.

Gauge Boson	γ	g	$W^{\pm}/Z^0$
	Photon	Gluon	W/Z Boson
Force	Electromagnetic	Strong	Weak
Charge	0	0	$+1/0$

2.2   Quantum Chromodynamics

In 1973 physicists Harald Fritzsch, Heinrich Leutwyler and Murray Gell-Mann proposed the existence of an additional quantum number of 'color' charge as the source of the strong interaction giving rise to a new field of particle physics known as Quantum Chromodynamics (QCD) [8]. In addition the inclusion of such a property provided explanation for the existence of observed states in nature consisting of three identical quark flavours; such states on their own violating the exclusion principle. A single quark is said to carry one of three color charges labelled *blue*, *green* or *red* with an anti-quark having the opposite charge (anti-blue etc.). As there is no observation of an unbound quark state in nature, nor any direct observation of quark color, an additional constraint is that composite particles must be 'colorless' carrying a total color charge of zero. The strong force is mediated by gluons which unlike photons in QED can self couple due to their color charge leading to additional properties. The strength of these interactions is determined by the running coupling constant, α_S with the potential being in the form [9]:

$$V(r) \propto \frac{A}{r} + Br. \tag{2.1}$$

The effect is that at relatively small separations quarks repel one another, and furthermore, perturbative techniques can be employed to describe the interactions. However at larger separations the second term dominates and the quarks are attracted. At these distances the behaviour of gluons can be compared to that of an elastic

band attached to two objects, with increasing separation of the two fermions the strength of the force increases. The addition of color charge conservation restricts the interaction to pairs of quarks only. The three color charges lead to QCD being described using a Lie algebra by an SU(3) gauge group, and it is from this group that the eight gluon types are defined from the various permitted charge combinations. Note that the use of a SU(3) yields a ninth colorless singlet state [4]:

$$\frac{1}{\sqrt{3}}(r\bar{r} + g\bar{g} + b\bar{b}) \tag{2.2}$$

unaffected by SU(3) transformations. Quarks are confined together as hadrons, a requirement for these composites is that the overall color charge be neutral. An accepted postulate, supported by observation, is that all free particles formed from valance quarks are color neutral [4].

The eight gluons form an octet which arises from the symmetry and Lie algebra:

$$
\begin{array}{cc}
\frac{1}{\sqrt{2}}(r\bar{b} + b\bar{r}) & -\frac{i}{\sqrt{2}}(r\bar{b} - b\bar{r}) \\[4pt]
\frac{1}{\sqrt{2}}(r\bar{g} + g\bar{r}) & -\frac{i}{\sqrt{2}}(r\bar{g} - g\bar{r}) \\[4pt]
\frac{1}{\sqrt{2}}(b\bar{g} + g\bar{b}) & -\frac{i}{\sqrt{2}}(b\bar{g} + g\bar{b}) \\[4pt]
\frac{1}{\sqrt{2}}(r\bar{r} - b\bar{b}) & \frac{1}{\sqrt{2}}(r\bar{r} + b\bar{b} - 2g\bar{g})
\end{array}
$$

note that although two of these states appear 'colorless' they do not exhibit 'color-invariance' under SU(3) transformation.

2.3   Electroweak Unification

The electromagnetic force behaves in a manner inverse to the strong in terms of the running of the coupling constant α_{EM}. As the potential difference takes the form:

$$V(r) \propto \frac{A}{r} \tag{2.3}$$

an increase in particle separation, or decrease in energy, results in a weaker interaction strength. With increasing energy the forces of electromagnetism and weak interaction tend to the same magnitude, the exact point of this merger is derived from the vacuum expectation value for the Higgs field:

$$\frac{1}{\left(G_F\sqrt{2}\right)^{\frac{1}{2}}} \sim 250\,\text{GeV} \tag{2.4}$$

where G_F is the Fermi coupling constant. The term within the SM symmetry group of the form $SU(2)_L \otimes U(1)_Y$ is formed of the coupling to left handed fermions and weak hypercharge:

$$Y = 2(Q + T_3) \tag{2.5}$$

which consists of the electric charge Q and third component of weak isospin T_3, both of which are conserved. In the Weinberg-Salam theory the relation of the electroweak boson masses from spontaneous symmetry breaking can be described as a rotation given by the Weinberg angle θ_W from the massless boson states W^0 and B^0 to the massive bosons Z^0 and γ:

$$\begin{pmatrix} Z^0 \\ \gamma \end{pmatrix} = \begin{pmatrix} \cos\theta_w & -\sin\theta_w \\ \sin\theta_w & \cos\theta_w \end{pmatrix} \begin{pmatrix} W^0 \\ B^0 \end{pmatrix} \tag{2.6}$$

with the relation between Z^0 and the $W^\pm$ boson masses then being:

$$M_W = M_z \cos\theta_w \tag{2.7}$$

2.4   Flavour Changing Neutral Currents

Weak interactions are divided into two categories, Charged Currents where the decay involves a $W^\pm$ boson which carries charge and Neutral Currents via the exchange of a Z^0 boson. A neutral current decay which describes a change in quark flavour, known as a Flavour Changing Neutral Current (FCNC) process, is forbidden at tree level within the Standard Model. Such decays may only occur through higher order loop induced processes, such as electroweak 'penguin' diagrams or box diagrams, the quark contributions within these loops affecting the decay amplitude, or through new physics.

Through analysis of leptonic decays Nicola Cabibbo proposed the concept of quark mixing in 1963 as explanation for the observed relative amplitudes of decays between quark generations [10]. Within the Cabibbo mechanism, rather than using the physical d and s quark states, weak interactions are described by the eigenstates d' and s' in the matrix form:

$$\begin{pmatrix} d' \\ s' \end{pmatrix} = \begin{pmatrix} \cos\theta_C & \sin\theta_C \\ -\sin\theta_C & \cos\theta_C \end{pmatrix} \begin{pmatrix} d \\ s \end{pmatrix}. \tag{2.8}$$

where the probability of these interactions occurring are dependent on the Cabibbo angle θ_C [4]. However the limitations of this model became apparent when combined with the S. Glashow theory of an SU(2)×SU(1) description of electroweak lepton interactions, which further postulated the existence of the Z^0 and γ neutral vector bosons [11]. Both worked together in helping to describe lepton physics, but gave
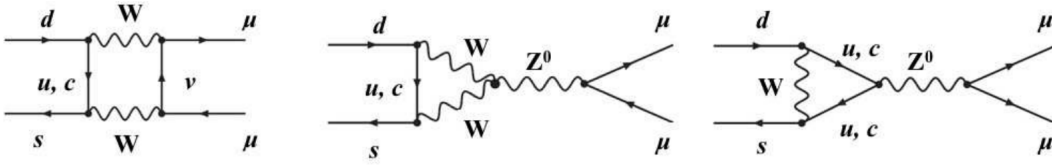
Figure 2.1: Box and loop diagrams showing the mechanism for $K_L \to \mu^+\mu^-$, the low branching ratio is due to the GIM mechanism. The matrix terms describing the c and u quark contributions interfere destructively [11].

rise to first order FCNC decays which are not observed.

The solution put forward as the GIM mechanism by S. Glashow, J. Iliopoulos and L. Maiani in 1970 postulated the existence of a third quark, which in turn introduces an additional component to the FCNC loops giving rise to a term in the amplitude matrix which has an opposite sign acting against that from the u quark. The existence of this third, at that time undiscovered, c (or charm) quark gives rise to opposite sign terms in the decay rate amplitude for processes such as $K^\pm \to \pi^\pm\mu^+\mu^-$ and $K_s \to \mu^+\mu^-$ (shown in Figure 2.1). These terms therefore reduce the branching ratio of such decays, in the case of $K_s \to \mu^+\mu^-$ the measurement being 10^{-9} [12]. Later discovery of the J/ψ charmonium state in 1974 [13,14] and further measurement of the charm quark mass of $1.27\,\text{GeV}$[1] confirmed the reduction in amplitude and concluded it to be proportional to difference in the up and charm quark masses, $m_c^2 - m_u^2$.

Not only does the GIM mechanism suppress the higher order processes, but it also leads to a weak isospin structure which forbids these decays at tree level.

Given the suppression of FCNCs, any measurement which yielded a higher than expected branching ratio for such decays would provide evidence for new physics beyond SM interpretation and would be a candidate for extension models. It is because of this that the probing the rare decay sector has become the objective for

---

[1]Quark masses are not measured directly but inferred from their impact on the observed hadron masses [12].

collider experiments such as LHCb.

2.5   The CKM Matrix

In electroweak interactions the flavour of quark changes between mother and daughter particles due to the properties of the couplings involved. The rate of these processes depends heavily on which quarks are involved. Transitions which lead to quark changes between generations, for example $t \to s$, are less likely to occur within the SM when compared to those within the same generation (e.g. $t \to b$), this constraint is known as *Cabibbo suppression*. The magnitude of all possible quark transitions can be assembled into a 3x3 unitary matrix known as the Cabibbo Kobayashi Maskawa (CKM) matrix which is the extension made by Makoto Kobayashi and Toshihide Maskawa to three quark generations of the prior two generation matrix proposed by Cabibbo. As last recorded by the PDG [1], the measured magnitudes for the components of this complex matrix were:

$$V_{CKM} = \begin{pmatrix} V_{ud} & V_{us} & V_{ub} \\ V_{cd} & V_{cs} & V_{cb} \\ V_{td} & V_{ts} & V_{tb} \end{pmatrix} \tag{2.9}$$

$$= \begin{pmatrix} 0.9745 \pm 0.0001 & 0.2245 \pm 0.0004 & 0.0037 \pm 0.0001 \\ 0.2244 \pm 0.0004 & 0.9736^{+0.0001}_{-0.0001} & 0.0421 \pm 0.0008 \\ 0.0090^{+0.0002}_{-0.0002} & 0.0413 \pm 0.0007 & 0.9991 \pm 0.0001 \end{pmatrix}. \tag{2.10}$$

The CKM matrix is a rotation matrix which transforms the mass eigenstates to

weak eigenstates and can also be expressed in terms of set of mixing angles:

$$V_{CKM} = \begin{pmatrix} c_{12}c_{13} & s_{12}c_{13} & s_{13}e^{-\delta} \\ -s_{12}c_{23} - c_{12}s_{23}s_{13}e^{i\delta} & c_{12}c_{23} - s_{12}s_{23}s_{13}e^{i\delta} & s_{23}c_{13} \\ s_{12}s_{23} - c_{12}c_{23}s_{13}e^{i\delta} & -c_{12}s_{23} - s_{12}c_{23}s_{13}e^{i\delta} & c_{23}c_{13} \end{pmatrix} \tag{2.11}$$

where $s_{ij} = \sin\theta_{ij}$, $c_{ij} = \cos\theta_{ij}$, and δ represents the phase due to violation of Charge-Parity symmetry (CP) an examination of the differences in behaviour between particle and anti-particle. This representation can be simplified when implementing an approximation deduced from the experimental observation that $s_{13} \ll s_{23} \ll s_{12} \ll 1$, to give rise to a new parameterisation of the matrix known as the *Wolfenstein parameterisation* with the terms:

$$s_{12} = \lambda, \ s_{23} = A\lambda^2, s_{13} = A\lambda^3(\rho - i\eta), \tag{2.12}$$

which expresses the matrix as:

$$V_{CKM} = \begin{pmatrix} 1 - \lambda^2/2 & \lambda & A\lambda^3(\rho - i\eta) \\ -\lambda & 1 - \lambda^2/2 & A\lambda^2 \\ A\lambda^3(1 - \rho - i\eta) & -A\lambda^2 & 1 \end{pmatrix} + \mathcal{O}(\lambda^4) \tag{2.13}$$

In the search for new physics, one line of investigation is to test the unitarity of this matrix by constructing a set of unitary triangles from its elements. If the matrix is found to not be unitary this implies that the total interaction probability is not unity, and so additional processes have not been accounted for within the SM. An example of one of these triangles is shown in Figure 2.2, where the angles α, β and γ have values which can be measured experimentally from interactions featuring the relevant quark transitions (such as meson decays) and the effects of CP violation.
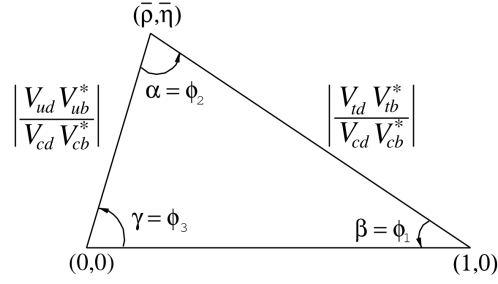
Figure 2.2: Unitary triangle created using elements of the CKM matrix [1]

2.6   CP Violation

The CP transformation is the combined effect of applying a charge conjugate C and parity symmetry P reflection. If CP symmetry is conserved the physics associated with a process, such as conservation of momentum, behaves the same before and after the symmetry has been applied.

When charge conjugation is applied to a particle we obtain, by definition, its antiparticle [4]:

$$\hat{C}|p\rangle = \pm|p\rangle = |\bar{p}\rangle, \tag{2.14}$$

hence only particles which are their own antiparticle can be eigenstates of C, for example for the π^0:

$$\hat{C}|\pi^0\rangle = \hat{C}|\frac{1}{\sqrt{2}}\left(u\bar{u} - d\bar{d}\right)\rangle \tag{2.15}$$

$$= |\frac{1}{\sqrt{2}}\left(\bar{u}u - \bar{d}d\right)\rangle \tag{2.16}$$

$$= -|\pi^0\rangle \tag{2.17}$$

C is conserved in electromagnetic and strong interactions but violated within weak interactions.

P-symmetry describes conservation of physics after a reflection of the system followed by a 180°rotation, this means that for a particle whose trajectory matches the

direction of its spin, this direction is reversed. The experiment into decays of cobalt-60 performed by C. S. Wu in 1956 provided evidence that this symmetry is also violated [15]. The expectation was that upon inversion the direction in which most of the electrons were emitted relative to the nuclear spin would be conserved, however this was not the case and an observation was instead made that the electrons were mainly emitted in the opposite direction (see Figure 2.3).

Violation of the combined CP symmetry has been observed through measurement of the rate of the decay of a particle when compared to that of its CP conjugate, with the first observation being made in $B^0 \to K^+\pi^+$ decays at BaBar and Belle [16,17].
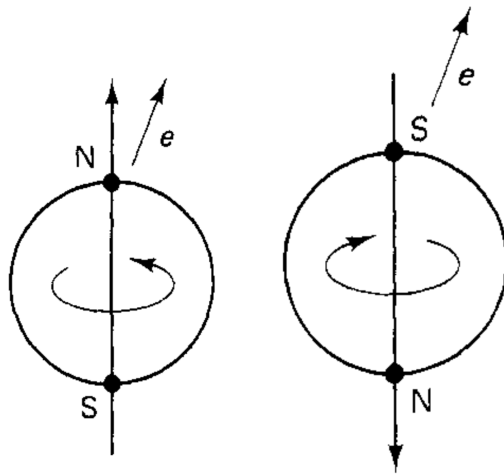
Figure 2.3: Observed parity violation in cobalt-60 decays, electrons are emitted mostly in a direction opposing expectation [4].

Chapter 3

The LHC 'beauty' experiment (LHCb) Experiment at the LHC

3.1   Collider Physics at the LHC

Searches for new physics have led to advances in particle accelerator technology with the aim being to push forward the observed energy threshold within collider experiments, such as those based along the Large Hadron Collider (LHC) at CERN in Geneva. In 2015 the LHC commenced its second phase (Run 2) of operation at an an energy of 13 TeV covering a greater expanse of phase space in searches for candidate particles with the aim being to find evidence for new physics described within theoretical predictions that extend beyond SM processes, examples including Supersymmetry and violation of Lepton Universality. The LHC facility consists of a 27 km underground acceleration ring with detectors positioned at four points where the two opposing beamlines cross. Protons are accelerated as bunches up to the required energy, initially by the Proton Synchrotron (PS) and Super Proton

Synchrotron (SPS) accelerators, before being fed into the LHC ring. The phase of proton bunches within the two beams is timed such that collisions are offset between each of the four crossing points where the detectors are located.

Two of the four detectors, ATLAS and CMS, are independently performing searches for new physics through proton-proton collisions at these higher energies and high luminosity, as well as aiming to improve prior measurements with an increasing level of statistics. The ALICE experiment is focused primarily on the study of quark-gluon plasma through the collision of lead ions, the aim being to perform measurements on conditions comparable to those during the state of our universe close to the point of formation, the 'Big Bang'. Finally the fourth experiment LHCb is aiming to find new physics through precision measurement of very rare b and c hadron decays, as well as measurements of decay channels which give evidence to the violation of the consequential symmetries of SM physics, with such violations perhaps being the key to explaining the particle-anti-particle imbalance within the universe.

More recently LHCb has ventured beyond the scope of its design looking into the physics of 'strange' particles formed from s quarks via decays in the Kaon sector as part of the 'Rare Decays' program. The current aim for these investigations are feasibility studies into the capability of the detector within this field, determining whether enhancements made to the triggering and data stream systems will allow the detector to observe particles at lower momentum thresholds. Although not dedicated to kaon physics measurement like other experiments such as NA62 [18], also at CERN, it is hoped LHCb will be able to reinforce existing measurements and aid in the related new physics searches. In addition to the search for $K^{\pm} \to \pi^{\pm}\mu^{+}\mu^{-}$ described within this thesis, LHCb has performed measurements on other Kaon decays such as $K_s^0 \to \mu^{+}\mu^{-}$ [19] [20].

3.2   The LHCb Detector

The LHCb detector, shown in Figure 3.1, is situated at Point 8 of the LHC. Unlike a typical collider experiment it has an acceptance range in only a single direction along the beam path, classed as 'forward-arm', with a pseudorapidity range of $1.6 < \eta < 4.9$ [22], where pseudorapidity is defined using the angle between the track and position z [1]:

$$\eta = -\log\left(\tan\frac{\theta}{2}\right). \tag{3.1}$$

The motivation behind this restricted coverage is the nature of b and $\bar{b}$ hadron production, such particles being produced predominantly in the same direction relative to the collision axis at high energies and pseudorapidity. A production angle plot for $b\bar{b}$ at $\sqrt{s} = 14\,\text{TeV}$ constructed using MC is shown in Figure 3.2. As the investigation of the decays of such particles is the primary purpose of the experiment, determining any differences in behaviour between particle and anti-particle, additional coverage is deemed to be unbeneficial at the cost of reduced access for maintenance and upgrade purposes, as well as financial cost.

The spectrometer is approximately 20 m in length and consists of a set of consecutive detection layers designed for high precision tracking and an optimum level of particle identification. These systems include silicon trackers, Cherenkov detectors, calorimeters and a muon system.

3.2.1   Beampipe

Within the limits of the LHCb detector the beampipe, through which the accelerated protons travel, is held at an ultra high level of vacuum to ensure the particles do not

---

[1]Within LHCb the positioning of detector modules is described using either a cylindrical or Cartesian coordinate system defined with the positive z axis being parallel to the beam line, and positive in the direction downstream of the interaction point.
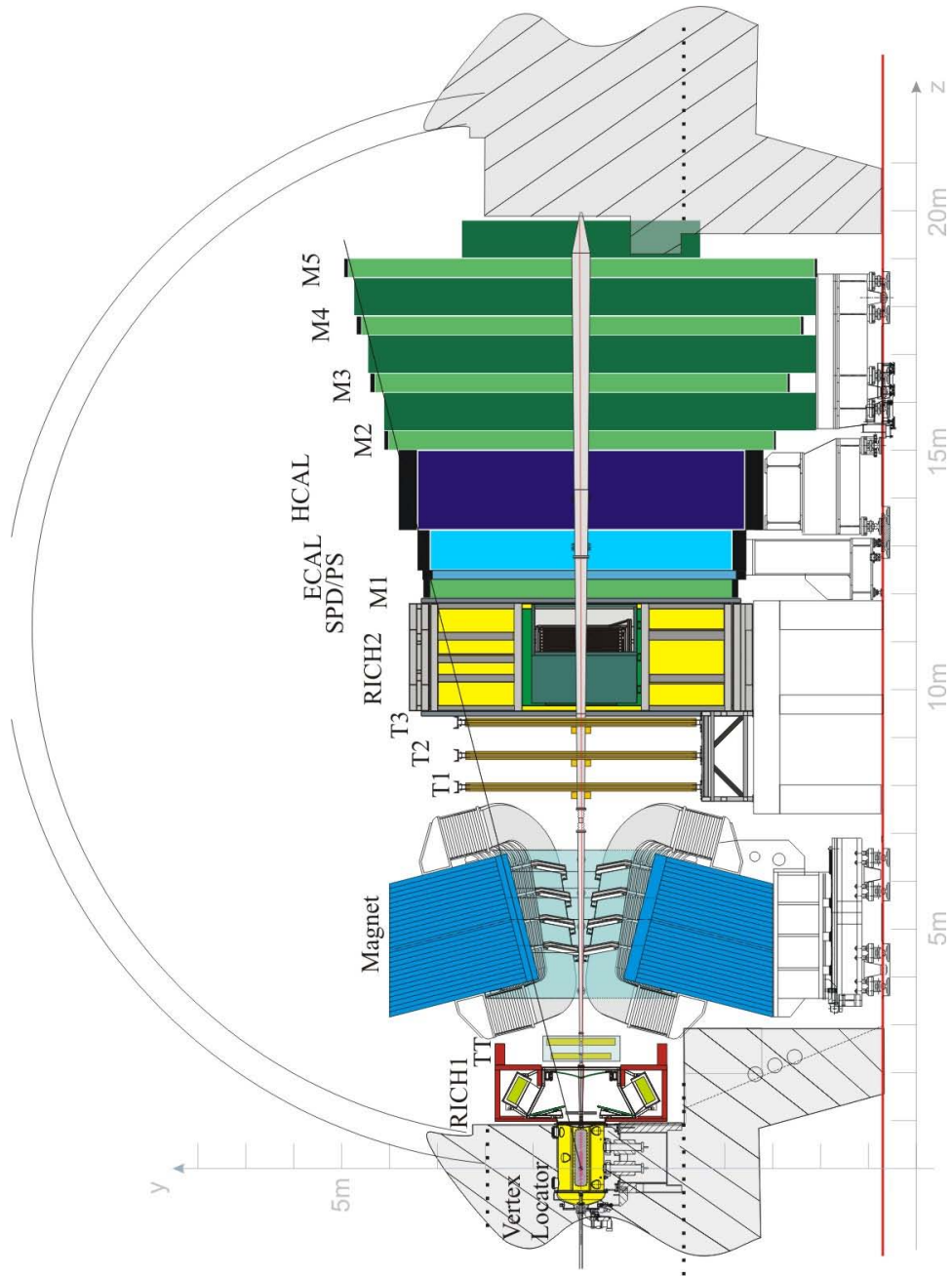
Figure 3.1: Schematic of the LHC 'beauty' experiment (LHCb) detector showing the two Ring Imaging Cherenkov (RICH) detectors, muon stations, electromagnetic and hadronic calorimeters, and the tracking system including the Vertex Locator (VELO). [21].
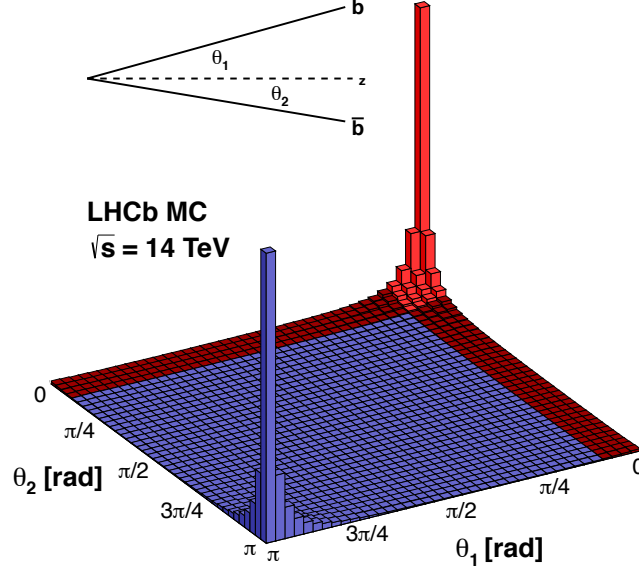
Figure 3.2: Production angle distribution for simulated $b\bar{b}$ events within LHCb at a centre of mass energy of $\sqrt{s} = 14\,\text{TeV}$ [23].

interact anywhere aside from the interaction point. The pipe is formed of four main sections which are conical in shape. The beampipe is mostly formed of beryllium due to the high transparency to particles produced within collisions, however the cost and toxicity of the metal mean usage is restricted to only the first three sections, the most downstream section being formed of stainless steel [24].

To preserve beam conditions the vacuum chamber must be periodically heated to temperatures $\sim 200\,°\text{C}$, a process known as 'baking-out'. To ensure that the beampipe remains constant in conditions, two sections with bellows (compensator sections) allow for adjustment to compensate for thermal expansion.

For protection of the LHCb tracking system from hadron flux due to possible beam misalignment, the experiment includes a Beam Conditions Monitor (BCM) [24] which is interlocked to LHC main control. On detection of misalignment or performance failure the system sends a request for a dump of the LHC beams to ensure there is

no damage to the detector components. The two BCMs are required to have a high threshold to radiation damage in order to be able to withstand the maximum possible doses resulting from such a failure, and so consist of chemical-vapour deposition diamond sensors. Each BCM positioned either side of the interaction point has eight of these sensors around the vacuum chamber.

3.2.2   Detector Magnet

The subdetectors sit downstream of a magnetic field created by two saddle-shaped coil magnets which form a rectangular yoke, these are positioned above and below the beamline at an angle matching the detector acceptance [24]. The design of magnet is chosen to ensure an integrated field of $4\,\mathrm{Tm}$ for deflection of $10\,\mathrm{m}$ tracks, providing a field below $2\,\mathrm{mT}$ for the intra-RICH regions, but maximum capacity for the region between the VELO and start of tracking. The variation of the transverse y component of the magnetic field as a function of displacement along the beam axis z is given in Figure 3.6. The magnetic field deflects the tracks of collision products altering the momentum of charged particles, and data is collected at both 'Up' and 'Down' polarities to account for asymmetries within the detector system [25]. The design was further motivated for its cost effectiveness and due to the limited space available within the experimental hall previously occupied by the DELPHI experiment [24]. To reduce the effects of stress caused by thermal expansion only one of the fifteen Aluminium-99.7 'pancake' layers which together form a single magnet coil is fixed in position, with the others being allowed to freely move within their supports. The magnet is managed by two systems: the Magnet Control System which monitors the conditions of the magnet also controlling the power supply for generation of the magnetic field, and the Magnet Safety System which ensures a discharge of the magnet if parameters fall outside of the limits of safe operation.

3.2.3   Tracking

The tracking system is formed of three main regions consisting of the VELO positioned around the proton-proton interaction point, the Silicon Tracker which consists of the Tracker Turicensis (TT) upstream from the magnet and the Inner Tracker (IT) downstream at the centre of the detector, and the Outer Tracker (OT) which is formed of straw tube detectors.

The Vertex Locator

A unique and defining part of LHCb, the VELO is able to measure to high precision the locations of secondary vertices and track trajectories. In the case of b and c hadrons these vertices are characteristically displaced from the interaction region. The VELO consists of seventeen staggered stations perpendicular to and positioned along the beam axis. Each station is formed of two consecutive semi-circular silicon layers, each measuring 8.4 cm in diameter, and wired alternately in the r and ϕ axes as shown in Figure 3.5. Acceptance requirements for the VELO are to detect particles in the LHCb pseudorapidity range (see Equation 3.1) of $1.6 < \eta < 4.9$ with primary vertices falling within $|z| < 10.6$ cm with respect to the beam interaction point. Prior to the detector are two additional planes which form the *pile-up veto system* a component of the hardware trigger system. The aim of the veto system is to reduce the level of multiple events in order to keep cuts applied within the hadronic hardware trigger as low as possible [26]. The VELO module layout is illustrated in Figure 3.3.
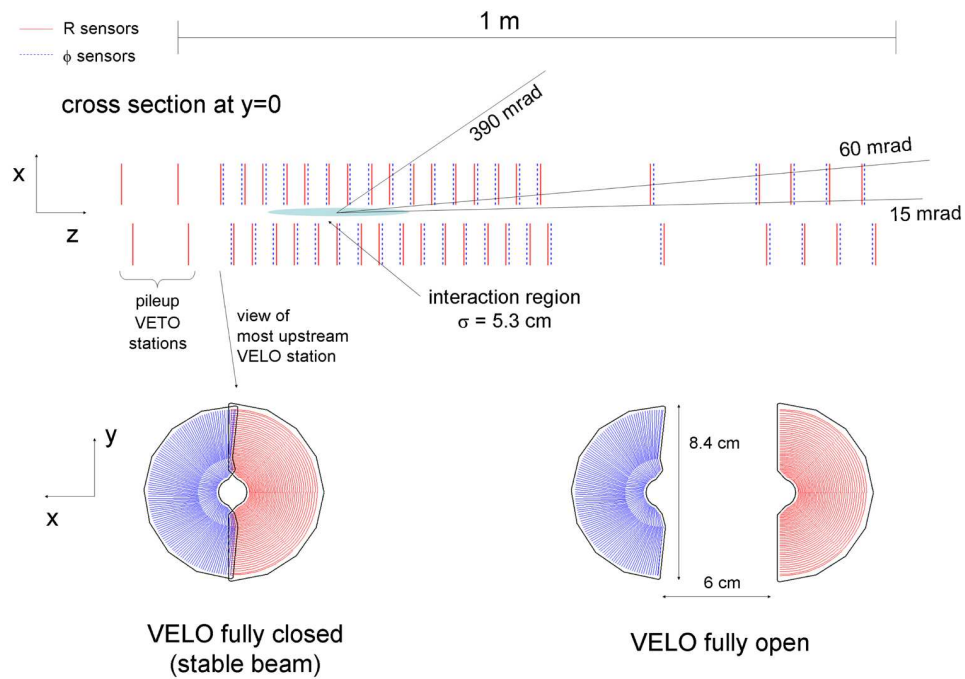
Figure 3.3: Projection of VELO in the *y-z* plane showing the pile-up veto system upstream and the spacing of the R and Φ sensors [24, fig. 5.1, p16]
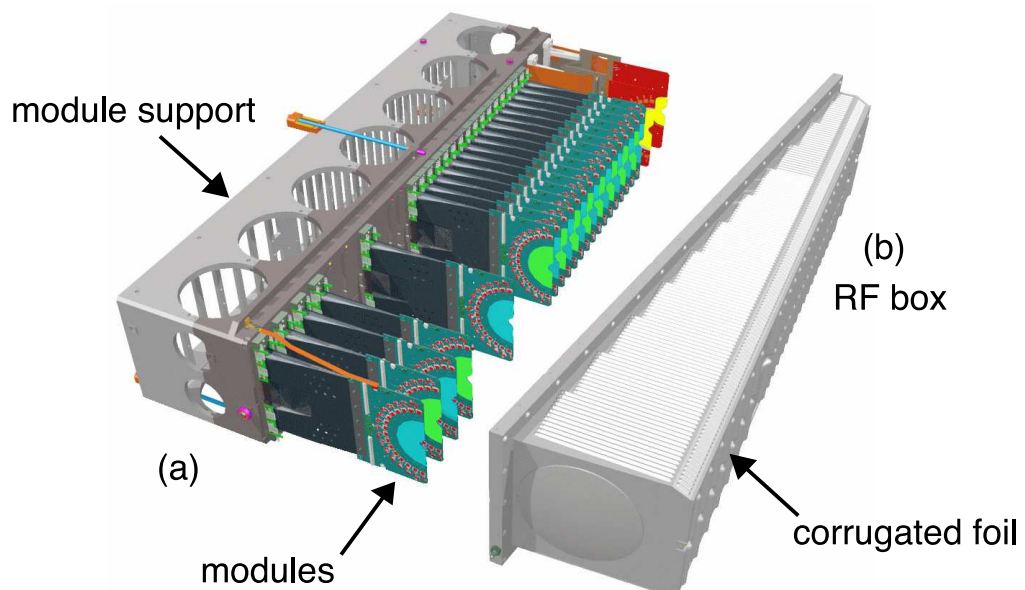
Figure 3.4: View of the VELO showing the surrounding RF foil and movement machinery [24].
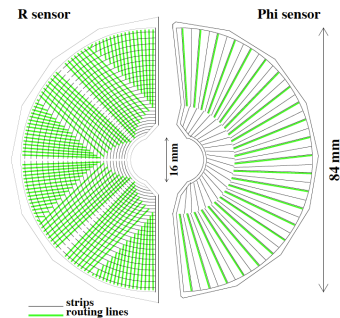
Figure 3.5: Cross section of one R-Φ station showing the orientation of wiring [27].

The subdetector sensors are surrounded by a vacuum and separated from the rest of the unit by a corrugated aluminium RF-foil (see Figure 3.4) which aims to reduce any radio wave interference on the beam. The foil prevents beam vacuum contamination via outgassing due to the VELO components and suppresses wake fields generated by its structure [28]. To account for the spread in possible beam position during filling of the LHC ring (which can be anything between $\pm 5\,\mathrm{mm}$ in both x and y axes transverse to beam direction) the two halves of the VELO are able to move outward from the beam axis by up to $30\,\mathrm{mm}$ [24]. The alignment of the VELO relative to the beam is possible due to the $10\,\mathrm{\mu m}$ accuracy of position measurement, further alignment of the constituent modules, and the backup method of a per fill software alignment. The reproducibility of the VELO between runs has been measured to be within $10\,\mathrm{\mu m}$ [27].

The software alignment method consists of four main stages: relative positional alignment of the R and Φ sensors using the distribution of residuals across them, relative alignment of the two co-moving halves of the detector by monitoring tracks within the geometrical overlap, use of residuals on the hits used for track reconstruction to find alignment within a single half, and a global alignment when compared to the other subdetectors. When a positive trigger decision is recorded data are collected by a set of Beetle ASICs [29] before being sent through a repeater system outside the VELO volume and transmitted to the Data Acquisition (DAQ) system. The whole unit is a length of just under $1\,\mathrm{m}$.

The position of the VELO at the interaction point means any particles produced which have a significantly larger lifetime than the target b and c hadrons do not decay within its volume. The tracks from such particles have a vertex beyond the VELO and are therefore labelled as 'Downstream' tracks, being detected by the tracking regions further into the detector. The alternative in which a vertex is registered is known as a 'Long' track, with both types being used within most LHCb analyses[2]. Additional track types are shown in Figure 3.6 and are either used as components of another type or for performing studies of the detector [30].
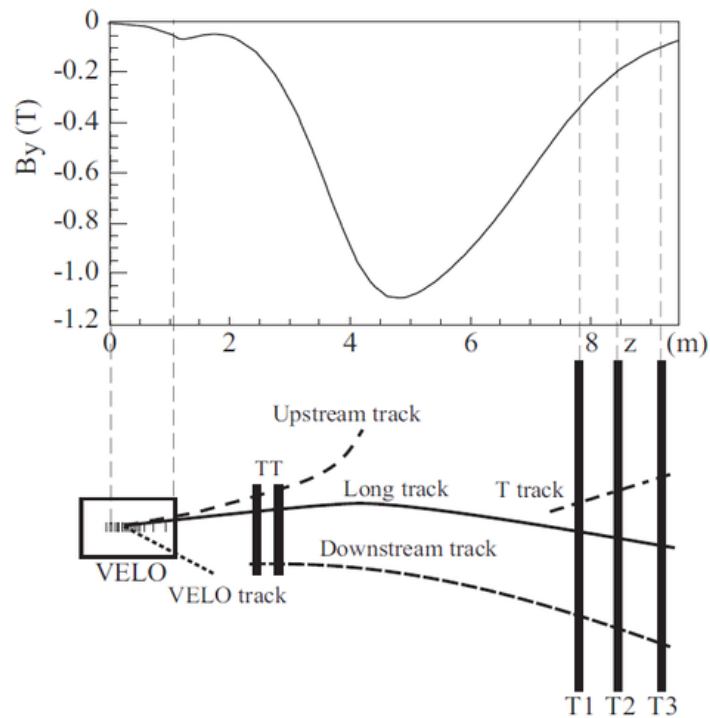
Figure 3.6: Distribution of the magnetic field and the labels given to the various types of track observed across the LHCb tracking detector [24].

The Silicon Tracker

Those tracking detectors formed of silicon based sensors are grouped under the Silicon Tracker.

---

[2]Within the analyses in this thesis only 'Long' tracks have been used as 'Downstream' tracks require additional processing with little improvement in statistics.
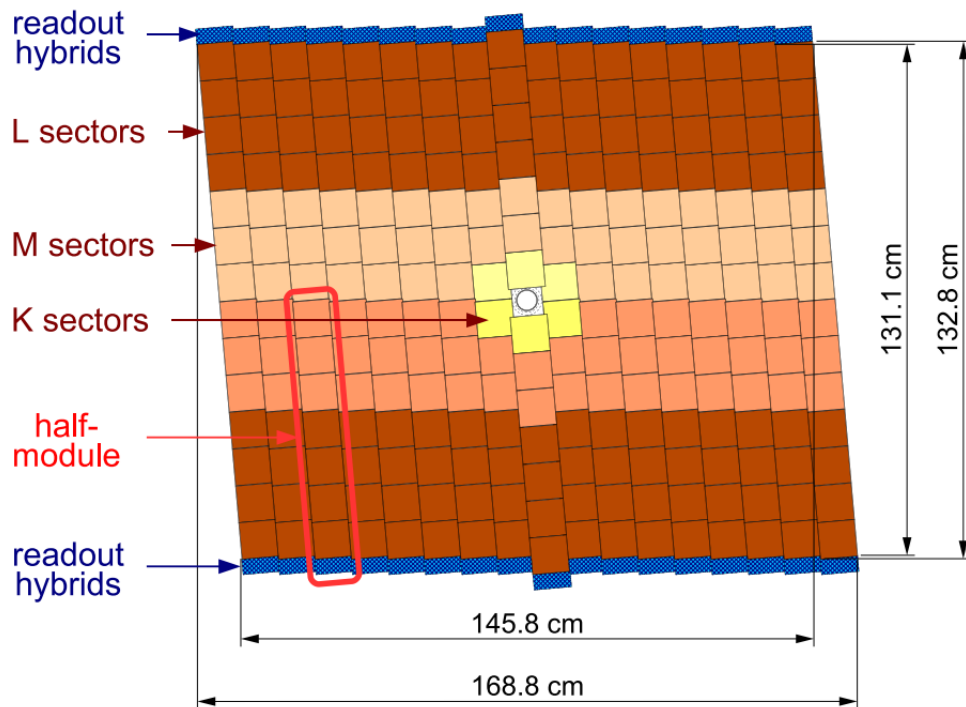
Figure 3.7: Cross section of the Tracker Turicensis (TT) showing the four layers of silicon strips [24].

The TT, shown in Figure 3.7, is positioned just before the magnet and has dimensions of 150 cm wide and 130 cm high consisting of four layers of silicon strip sensors contained within modules with readouts at each end. The layers are arranged in pairs to aid the algorithms incorporated into the process of track reconstruction. The detector is held at 5°C using C_6F_{14} gas and kept free of condensation by passing nitrogen through it. The layout is such that the modules above and below the beam pipe are divided to form two retractable regions each consisting of seven silicon sensors each. Those regions either side of the beam pipe span the full LHCb acceptance. All modules overlap in the x axis and are staggered by 1 cm in the z axis to prevent gaps in acceptance.

The IT has coverage of 120 cm wide and 40 cm high in a cross shape around the beam pipe shown in Figure 3.8 and Figure 3.9. The four regions, each consisting of seven modules, are again held at 5°C and flushed with nitrogen. Each module
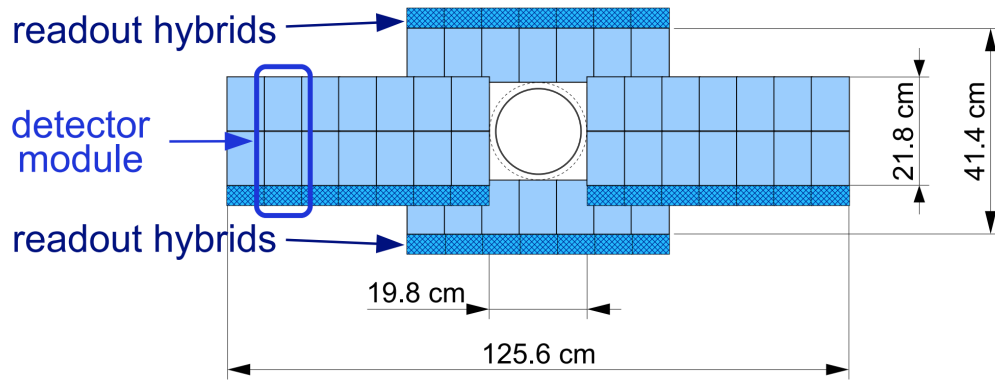
Figure 5.24: Layout of an *x* detection layer in the second IT station.

Figure 3.8: Cross section of the second Inner Tracker station [24].
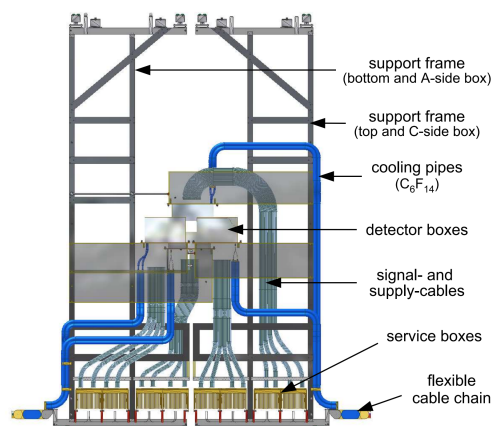
Figure 5.28: Front view of an IT detector station.

Figure 3.9: Inner Tracker detector station from front [24].

itself has one or two silicon sensors of differing thickness to the TT but the same in design, the dimensions being chosen to improve the signal/noise ratio.

Outer Tracker

Unlike the inner tracking regions, the OT is formed of drift-tube detectors. A wire runs down the centre of each 4.9 mm tube which is filled with a gas consisting of 70% Argon and 30% CO_2. A charged particle passing through these tubes knocks electrons from the inert gas to produce ions. A potential difference held between the wire and the tube wall means these ions drift towards the centre whilst the electrons move the opposite direction towards the walls. The current produced through certain tubes by a traversing particle then gives an indication of the trajectory for tracking. The drift times of the ionised particles are measured with respect to the time of the beam crossing and are then recorded for each bunch crossing being stored for the L0 trigger decision [24]. The detector is split in two vertically, each half being held on a C-frame which can be retracted for detector maintenance.

3.2.4   Calorimetry

An important part of particle identification is the calorimetry system which comprises of a Hadronic Calorimeter (HCAL) and an Electromagnetic Calorimeter (ECAL) positioned at 12.5 m and 13.3 m downstream of the interaction point, for distinguishing between electrons, photons and hadrons, and contributing to the decisions made by the L0 trigger. In addition upstream of the calorimeters is, a preshower detector (PS) which distinguishes between charged pions and electrons/photons, and a Scintillator Pad Detector (SPD) which selects charged particles [24]. The SPD and PS are separated by 2.5 radiation lengths of lead.

Within the calorimetry system, particles produced during collisions interact with charged particles and atomic nuclei for the electromagnetic and hadronic detectors respectively. The deceleration of these particles through processes such as multiple scattering and bremsstrahlung leads to energy loss through photons. These photons enter PMTss in which they collide with a photocathode formed of a photoemissive material leading to the emission of electrons. The photoelectrons are then accelerated across a potential difference to then strike a dynode to produce secondaries, the process is repeated until the current is amplified sufficiently such that it can be measured [31].

ECAL

The ECAL consists of scintillator material arranged into pads supported on a lead structure which also acts as an absorber. Scintillation light from particle interactions is read into Photo Multiplier Tubes (PMTs) via wavelength-shifting fibres, the collective name for this setup being *shashlik*. The ECAL is subdivided into three sections with increasing size of detector pads as a function of radius from the beam pipe, each pad being formed of support and detection material totalling 25 radiation lengths. The cells are also wrapped in TYVEK type 1025D black synthetic fibre to prevent any loss of scintillation light, with the choice of 4 mm scintillator material formed from polystyrene [24]. During Run 1 data taking between 2011–2012 the performance of the ECAL was measured for energy resolution:

$$\frac{\sigma_E}{E} = \frac{a}{\sqrt{E}} \oplus b \oplus c, \tag{3.2}$$

with the values of $8.5\% < a < 9.5\%$, $b \sim 0.8\%$ and 1.2 ADC counts for c [32].

HCAL

For the HCAL iron has been used as an absorber material arranged in alternating strips with scintillator material transverse to the beam [24]. The subdetector is cuboidal in shape and structured in two halves which can be separated when necessary for maintenance, each half consisting of 26 modules and, alike to the ECAL, having an inner and outer region with differing cell size. A *readout cell* within the HCAL is defined as a set of optical fibres positioned parallel to the beam axis that are connected to a single PMT located at the rear of the subdetector. To account for the higher level of light attenuation within the wavelength shifting fibres positioned further from the PMT, the optical contact with scintillator material is varied between cells.

3.2.5   RICH Detectors

The experiment has two Ring Imaging Cherenkov (RICH) detectors positioned upstream of the dipole magnet and just before the muon chambers. As a good level of PID is one of the founding objectives for LHCb, the inclusion of a system capable of distinguishing between particles such as kaons and pions in B-hadron decays is a requirement. Between the two subdetectors a large momentum range is covered with RICH1 and RICH2 covering 1–60 GeV and 15–100 GeV respectively [24].

This detection system is based on the property that a relativistic particle travelling within a medium at a speed that exceeds the speed of light within that medium causes the emission of photons in a Cherenkov light cone. The distortion of the projected ring can indicate the direction of the particle, and the angle of the cone relative to the particle direction gives a method for measuring momentum of the particle. This angle is related to the speed $\beta = v/c$ and refractive index $n(\lambda)$ of the

traversed medium [33]:

$$\cos\theta_C = \frac{1}{\beta n(\lambda)}. \tag{3.3}$$

For LHCb a series of flat and spherical mirrors are used to project the Cherenkov light into pixel based Hybrid Photon Detectors (HPDs) chosen for their sensitivity in spatial position measurement. These are held within iron containers to ensure no influence from the magnetic field. The locations of impact on the HPDs are used to reconstruct back the light cone under the assumption that point of photon emission lies midway through the detector. Although this results in a smearing of the angle for points where the emission lies elsewhere, these effects are negligible compared to the spatial resolution of the HPDs. The gas contained within each RICH is held within 50 Pa and at ambient temperature.

RICH1

The first RICH detector, shown in Figure 3.10a, is situated at a range $990 < z < 2165$ mm being positioned close to the interaction point downstream of the VELO. RICH1 covers the full angular acceptance of LHCb from ±300 mrad/±250 mrad and ±25 mrad horizontally/vertically, the lower limit defined by dimensions of the beam pipe. It contains an admixture of silica aerogel, chosen for its stability against irradiation, and perflourobutane (C_4F_{10}) gas which both act as a radiators for Cherenkov photons. C_4F_{10} has a refractive index $n \approx 1.0014$ which gives a maximum Cherenkov angle $\theta_C = 53$ mrad [34]. The HPDs are positioned above and below the gas cavity.

RICH2

The second RICH is positioned at $9500 < z < 11832$ mm close to the muon stations. It has a smaller acceptance of ± 120 mrad$/\pm 100$ mrad and ± 15 mrad horizontally/vertically owing to the requirement of a heating jacket and thermal insulation towards the procedure of 'baking out' the beam vacuum chamber. The choice of gas radiator is CF_4 for the higher momentum range under observation, and the HPDs are located parallel to the beam axis. CF_4 has a refractive index of $n \approx 1.0005$ and and gives a maximum Cherenkov angle of $\theta_C = 32$ mrad [34]. The subdetector is shown in Figure 3.10b.

(a) RICH1 [24].

(b) RICH2 [24].
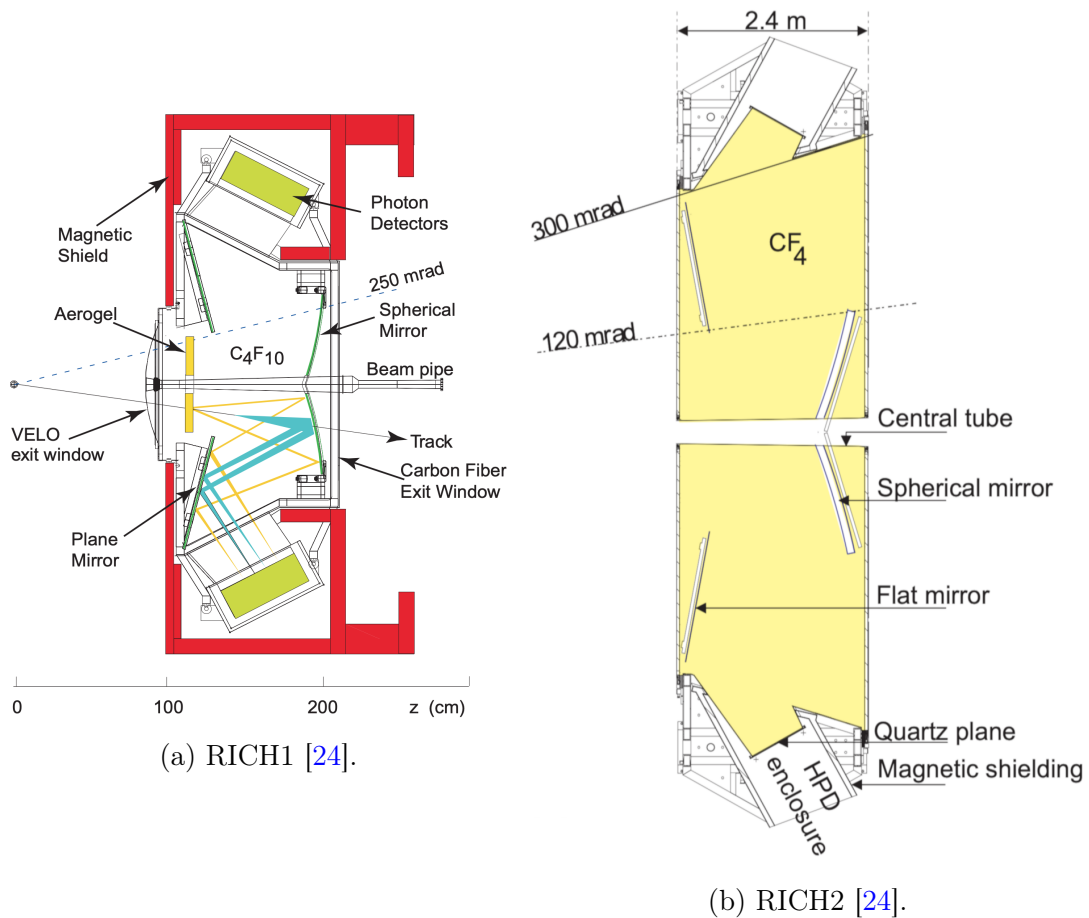
Figure 3.10: The two RICH subdetectors within LHCb situated downstream of the VELO and T1–T3 tracking stations respectively.

3.2.6   The Muon System

As part of the requirements for measurement of CP violation in the B decay sector, particularly in the *gold-plated* decays of $B_d^0 \to J/\psi(\mu^+\mu^-)K_S^0$ and $B_d^0 \to J/\psi(\mu^+\mu^-)\phi$, an efficient muon triggering and identification system are needed [24]. The Muon System in LHCb, shown in Figure 3.11, consists of five rectangular stations, the first positioned prior to the calorimeters and the latter four, separated by thick layers of iron to prevent muon penetration, at the extreme downstream end of the detector. To ensure coverage across the detector acceptance the stations radiate from the interaction point getting progressively larger transverse to the beam axis with increasing displacement in the $+z$ direction.

Stations M1–M3 are used to determine the direction of tracks having spatial resolution along the bending plane of the magnetic field (x axis). M1 downstream of the HCAL additionally improves the performance of the trigger through p_T measurement. Triggering within the muon system depends on hits being observed in all five stations. Alike to the calorimeters each station is divided into regions which are progressively larger in size and smaller in segmentation with radial distance, the scaling of the constituent muon chambers being 1:2:4:8.

The muon chambers consist of Multi Wire Proportional Chambers. As a muon enters the gas mixture of Ar, CO_2 and CF_4 it ionises it knocking electrons from the atoms.

Due to the high momenta of muons passing through LHCb the muon system is designed to record the simple binary decision `isMuon` for whether the candidate particle is a muon, this information then being passed subsequently to the trigger system. This decision is made using p_T measurements and by performing track reconstruction on the incident muons. Tracks are extrapolated from the VELO to a Field of Interest (FOI) within the stations. If the number of stations registering a

muon signal within this FOI exceeds a threshold value then the decision is recorded positive [35]. The size of the region is dependent on the momentum of the candidate and is chosen for each station referring to results taken from MC simulations [36].
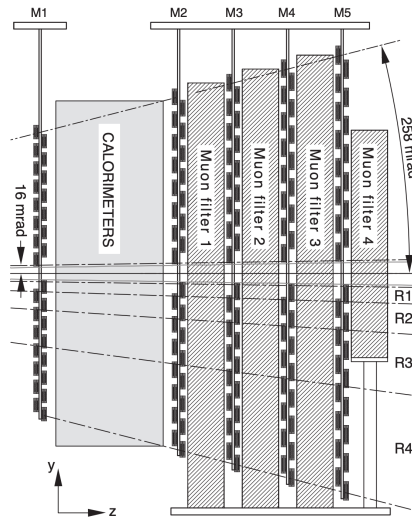
Figure 3.11: The LHCb muon chambers positioned at the extreme downstream part of the detector [24].

3.2.7   The Data Flow Process

The selection and processing of real data (and in addition generation of simulated data) is a multi-stage process which is divided between a series of applications which together form the LHCb software library. The Python frontend and C++ built tools for these applications are constructed via the Object Orientated framework *Gaudi*, which aims to provide a common infrastructure across all collaboration software [37]. At the trigger stage the process is identical for both simulated data (also known as *Monte Carlo* (MC)) and real data. To be treated identically, MC is digitised in such a way as to accurately model the behaviour of real data, the main difference being the retained 'truth' information.

Illustrated in Figure 3.12 are the various stages by which data is read into the detector and events are reconstructed using the available information collected by

the particle identification and tracking systems before then being processed into a form the analyser can work with in the form of Ntuples.

3.2.8   Triggering

The LHCb trigger has undergone significant changes between data collection at Run 1 and Run 2. Within this period the trigger system has consisted of a hardware trigger (L0) and the software based Higher Level Trigger (HLT) levels of HLT1 and HLT2 which occur one after the other. At the software level events are selected via a set of coded decisions, labelled *trigger lines*, which apply thresholds to veto out as much background as possible keeping to a minimum the volume of data to be written to disk as well as ensuring target signal efficiencies are met. In the initial design focus was held on obtaining large statistics for high momentum b and c hadron events, as such at this time there were no dedicated trigger lines for lower momentum events such as charged kaon decays. Within Run 2 such lines were incorporated alongside the addition of partial event reconstruction added to reject events as early as possible. In the future at Run 3, further improvements will be made firstly with the complete removal of the hardware trigger, then with implementation of complete event reconstruction at the software level.

Before any data is passed through the LHCb trigger system it is first constrained by the Global Event Cuts (GECs), with each L0 trigger line having a different threshold. The GECs used during data taking during Run 1 and Run 2 are given in Table 3.1 and consist on constraints on the number of SPD hits (and as such the multiplicity) of an event. These cuts are chosen based on results of investigations performed using MC to determine the thresholds within which pileup ceases to have influence on the size of an event.

LHCb is unique in its ability to trigger independently on events which fall within
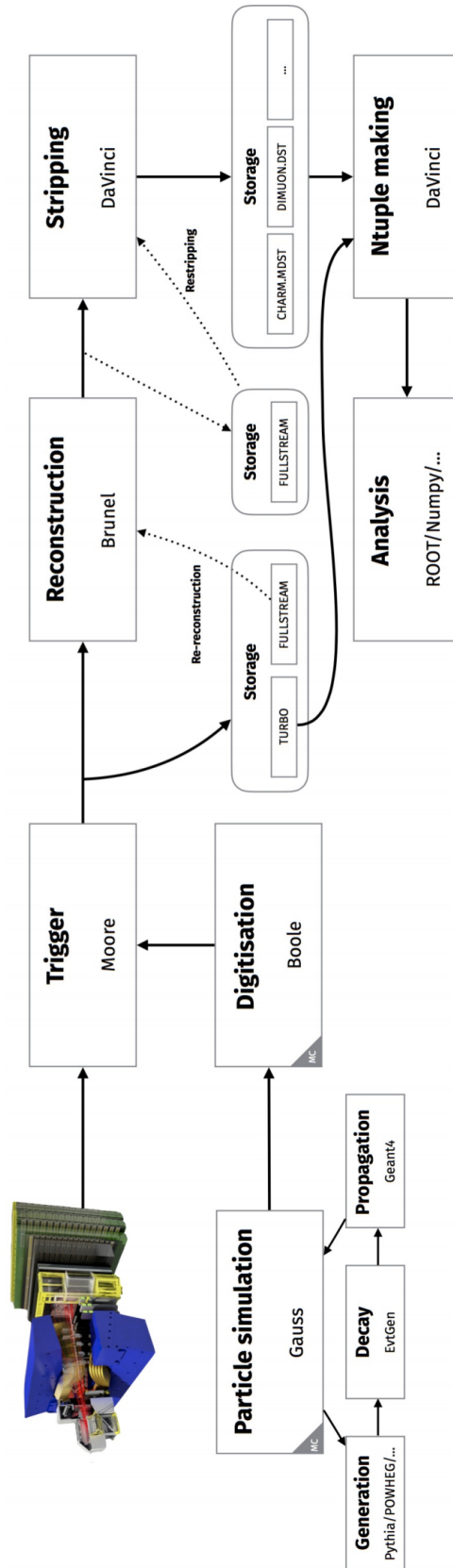
Figure 3.12: The LHCb workflow for both real and simulated data, each step has its own respective software project. MC is generated with simulation of detector response being provided by GEANT4 before then being digitised to match the form of data. Data is stored to disk at three stages allowing for re-stripping and turbo analyses [38].

(a) Run 1 system   (b) Run 2 system   (c) Future Run 3 system
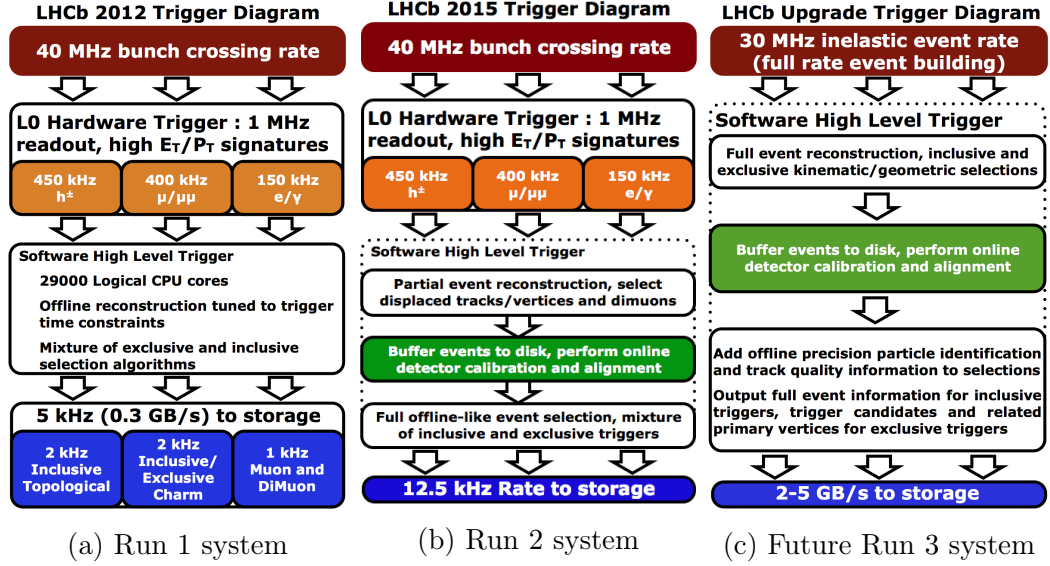
Figure 3.13: Trigger systems between Run 1 and future Run 3 where the hardware L0 will be removed and full event reconstruction will occur at the software level [39].

L0 Trigger Line	SPD Multiplicity	
	Run 1	Run 2
Hadron	< 600	< 450
Photon	< 600	< 450
Electron	< 600	< 450
Muon	< 600	< 450
Muon high p_T	none	none
DiMuon	< 900	< 900

Table 3.1: GEC cuts applied to data before it is processed by the L0 trigger [40].

two categories. The first is an event which has been triggered due to the presence by particles relating to the signal candidate, these are referred to as Trigger On Signal (TOS) events. The second category are those events which are triggered without any this requirement and so are referred to as Trigger Independent of Signal (TIS) events. In the case of charged kaon decays $K^{\pm} \to \pi^{\pm}\pi^{+}\pi^{-}$ this is a vital component in ensuring sufficient statistics for analysis as around 90% of the collected statistics fall within this additional TIS category.

A Data Driven Method for Obtaining Trigger Efficiency

The ability of LHCb to trigger on events as TIS leads to the possibility to measure trigger efficiency using real data [41]. The true efficiency is defined as:

$$\epsilon_{trig} = \frac{N_{Trig|Sel}}{N_{Sel}}, \tag{3.4}$$

where N_{Sel} and $N_{Trig|Sel}$ are the total number of events processed and accepted by the trigger respectively. As a trigger system does not store information on the events rejected ϵ_{trig} cannot be measured directly from data, however we can use the categories of TIS and TOS to obtain an estimate:

$$
\begin{aligned}
\epsilon_{trig,tistos} &= \frac{N_{Trig|Sel}}{N_{Sel}} \\
&= \frac{N_{Trig|Sel}}{N_{TIS|Sel}} \times \frac{N_{TIS|Sel}}{N_{Sel}} \\
&= \frac{N_{Trig|Sel}}{N_{TIS|Sel}} \times \epsilon_{TIS}.
\end{aligned}
$$

$N_{TIS|Sel}$ and $N_{TOS|Sel}$ being the respective TIS and TOS yields. In the assumption that it is independent of the sample taken, the TIS efficiency ϵ_{TIS} can be determined

by looking at the fraction of TOS events that are also TIS:

$$\epsilon_{TIS|TOS} \;\; = \;\; \frac{N_{TISTOS}}{N_{TOS}} \tag{3.5}$$

$$\epsilon_{TIS} \;\; \equiv \;\; \epsilon_{TIS|TOS} \tag{3.6}$$

where N_{TISTOS} represents those events which are both TIS and TOS. The validity of this assumption is studied thoroughly within Tolk et. al. (2015) [41]. Finally the efficiency can then be estimated as:

$$\epsilon_{trig,tistos} = \frac{N_{Trig|Sel}}{N_{TIS|Sel}} \times \frac{N_{TISTOS}}{N_{TOS}} \tag{3.7}$$

by recording the number of signal events within each category. This method is known as the 'TISTOS' method. The efficiency $\epsilon_{TIS|TOS}$ has a correlation, due to the trigger selections being based on transverse momentum and impact parameter cuts, with the signal sample chosen which is not negligible. This effect can however be reduced if the TISTOS calculation is performed in bins of phase space, summating the events in the ratio [41, eq. 10]:

$$\epsilon_{trig,tistos} = \frac{N_{Trig|Sel}}{\sum_i \frac{N^i_{TIS|Sel} N^i_{TOS|Sel}}{N_{TISTOS|Sel}}}, \tag{3.8}$$

examples of this are given later within the thesis is in the analyses of $K^\pm \to \pi^\pm \mu^+ \mu^-$ discussed in chapter 4 and $B_c^\pm \to \phi K^\pm$ in section 5.2.

Moore

The *Moore* application handles the implementation of the HLT1 and HLT2 software triggers [42] to both data and MC as well as the emulation of the L0 hardware trigger on MC. The configurations for the triggers are given unique identifiers known

as Trigger Configuration Keys (TCKs) [43] typically in the form of 32 or 16 bit values. Also recorded under these identifiers are the prescalings of the trigger lines run during the triggering. To ensure a fair and balanced level of statistics between analyses, given the constraint of a finite amount of data storage, some trigger lines are scaled such as to store only a fraction of events which pass them. When determining the trigger efficiency for an analysis it is therefore important to account for these factors.

3.2.9   Reconstruction with Brunel

The reconstruction of particle tracks from events is performed using the program *Brunel* another Gaudi application which is run in independent phases. These phases are built of sets of sequences one for each sub-detector which execute the reconstruction algorithms. As an input Brunel can take either real or simulated data; for MC the 'RAW' hits within the detector are digitised and the emulated trigger decisions from LHCb are applied to create an output which matches a set of real data [44]. The MC truth information is smeared using random number generators, these also being used during the digitisation process.

The reconstruction process occurs in three main steps. Within the first step initialisation takes place using information from digitisation and subdetectors depending on the data type and data taking conditions; configuration of the application then determining the order in which this information is read. The second stage contains any algorithms which require the raw reconstruction information from several subdetectors. Finally the last step is the monitoring stage which is optional and allows for customised output from the program, here histograms from the various phases can be specified as well as the output log information.

Brunel obtains its detector information from XML based databases which describe

conditions and geometry, these are updated for each run and variation in detector layout.

Track Fitting

A Kalman filter is used to account for multiple scattering in the fitting of the tracks identified within the detector [45]. A map of the materials traversed by the particles is used to perform the offline fitting. In the case of the tagging of B mesons the Impact Parameter (IP) is used in the identification procedure, this is measured as the distance of closest distance approach between the extrapolated B track and the proton-proton collision point.

The Kalman filter process consists of three main parts. The parameters of tracks within all tracking stations at a given time describe a single state. In the first stage a model is constructed to predict the values of track parameters for a new state based on those obtained measured. Within the filtering stage this model is then updated using information collected by new measurement. Finally the process is repeated in the reverse order for the remaining track states.

Two measurements performed using LHCb track objects are the Distance of Closest Approach (DOCA) and the Impact Parameter (IP). One variable used within an analysis is the maximum value of the Distance of Closest Approach (DOCA) (DOCAMAX), taking for example the decay of $K^{\pm} \to \pi^{\pm}\pi^{+}\pi^{-}$ as illustrated in Figure 3.14a, the DOCAMAX is the maximal separation between two of the pions. For the same decay the definition of the Impact Parameter (IP) is shown in Figure 3.14b and is defined with respect to each pion as the perpendicular distance between the proton-proton interaction point and the direction of the particle. Within LHCb the minimum value of the χ^2 associated with performing this measurement (minIPχ^2) is often taken as a variable for analysis, and is included within the training of classifiers for

signal-background separation in the analysis for $K^{\pm} \to \pi^{\pm}\mu^{+}\mu^{-}$.

(a) DOCAs.

(b) Impact Parameters.
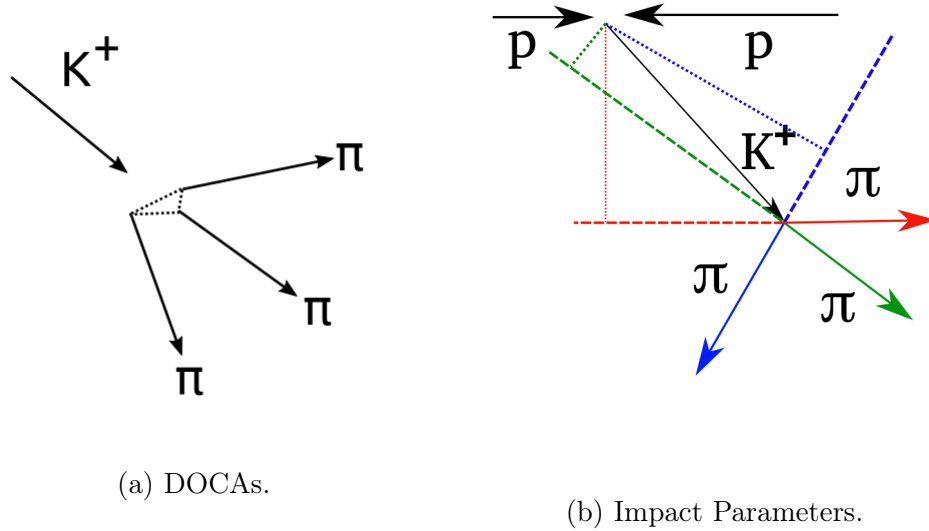
Figure 3.14: Example of measurements performed within LHCb selection for $K^{\pm} \to \pi^{\pm}\pi^{+}\pi^{-}$ showing IP and the closest distance between two particles (DOCA) for the daughter pions.

3.3   Stripping and Turbo

Since official data taking started in 2011 LHCb data has been passed through a process known as *Stripping* before being stored in bookkeeping for user access. Similar to triggering, stripping consists of a library of lines coded within Python and containing cuts to various kinematic variables, and acts as a pre-selection before offline analysis. The purpose of stripping is to filter out candidates for prospective analyses as early as possible, thereby reducing the required disk space for storage. A library of such lines has been written for the investigation of rare kaon decays with dedicated lines being included for $K^{\pm} \to \pi^{\pm}\mu^{+}\mu^{-}$, $K^{\pm} \to \pi^{\mp}\mu^{+}\mu^{+}$ and $K^{\pm} \to \pi^{\pm}\pi^{+}\pi^{-}$, as well as analyses into the B_c sector including $B_c^{\pm} \to \phi K^{\pm}$. To ensure an analyst need only deal with data relevant to their analysis, the output of a stripping is grouped into collections known as *streams*, for example, the *Semileptonic* stream holds events relevant to decays in the form $h \to h l^{+}\nu_l$.

As of 2016 data taking information relating to the quality of the offline reconstruction has been made available within the trigger, a decision was therefore made to develop a new data stream whereby analysis could be performed directly at the software trigger level on abundant decay modes without the need for the time consuming stripping process. Within the method, named 'Turbo', events are processed by a new application *Tesla* which organises the data into a form which can then be directly accessed for analyses [46]. As only events which pass a given Turbo line are kept, the storage usage is reduced to 10% of that required for the full data stream; as such it is expected that at Run 3 most analyses will be performed using the Turbo stream, with only those requiring complete candidates using the full data stream via stripping. Due to Turbo lines having not yet been written the concept has not been exploited in the analyses within this thesis. However with an improvement in trigger performance expected after the upgrade at Run 3, the L0 being removed completely, with the added higher luminosity running, such a method of selection is likely to form the future preferred choice for kaon physics analyses at LHCb.

3.3.1   Offline Selection with DaVinci

Offline selection is performed using the LHCb application *DaVinci*. The user is able to construct a python script to call tools which interpret the events recorded within the data file output of stripping and produce a tree object stored in a ROOT file from which the events can be interpreted.

The utility upon which the operation of performing selection is built is called the Loops & Kinematics (LoKi) framework and is designed to be a simple method for performing analysis on the fly during ROOT file creation. A DaVinci tool common to most analyses is the *DecayTreeTuple* which aims to select candidates from stripping lines by interpreting a decay descriptor. Behind the scenes LoKi

Decay Finder algorithms apply cuts to candidates to determine whether or not they satisfy the constraints of this description forming the main part of offline selection. Taking as examples the decays featured within this thesis, the decay descriptors for $K^\pm \to \pi^\pm \mu^+ \mu^-$, $K^\pm \to \pi^\pm \pi^+ \pi^-$, $B_c^\pm \to \phi K^\pm$ and $B^\pm \to \phi K^\pm$ are shown in Table 3.2. The notation of `CC` refers to the requirement of selection on both the decay and the charge conjugate analogous anti-particle decay. The events selected by DecayTreeTuple are passed through a set of default tools which obtain properties of the events such as vertex fits on tracks, invariant mass and momentum information. By default only information with respect to the mother particle of the decay is stored, however additional particles can be tagged and labelled using the `^` syntax within the descriptor as shown. Additional tools can be included to add further properties. *TupleToolTISTOS* returns the Boolean decisions of whether an event passed a given set of trigger lines, this forms a vital part of determining the trigger efficiency of a decay for each of the three levels. For access to the NeuralNet-based PID decisions (see section 3.4), geometrical variables such as vertex position and impact parameters, and reconstruction of tracks *TupleToolANNPID*, *TupleToolGeometry* and *TupleToolReco* can be appended to DecayTreeTuple respectively. The variables created by these tuple tools can add strength to a classifier in separation of signal from background.

Table 3.2: Decay descriptors used within DaVinci for performing decay selections. The `^` tags additional particles to be processed by the DaVinci algorithms.

Decay	Decay Descriptor
$K^\pm \to \pi^\pm \mu^+ \mu^-$	`[K+ -> ^pi+ ^mu+ ^mu-]CC`
$K^\pm \to \pi^\pm \pi^+ \pi^-$	`[K+ -> pi+ pi+ pi-]CC`
$B_c^\pm \to \phi K^\pm$	`[B_c+ -> phi(1020) K+]CC`
$B^\pm \to \phi K^\pm$	`[B+ -> phi(1020) K+]CC`

3.4   The Particle Identification System

For the purpose of precision measurement LHCb has an advanced PID system. Information taken from the two RICH detectors and muon system is combined via a neural network to create a set of probability variables, labelled `ProbNN`, for the particles p, π, K, μ and e. The resolving power of the RICH system can be seen in Figure 3.15 which shows the difference in the relationship between Cherenkov angle and particle momentum within the C_4F_{10} radiator.
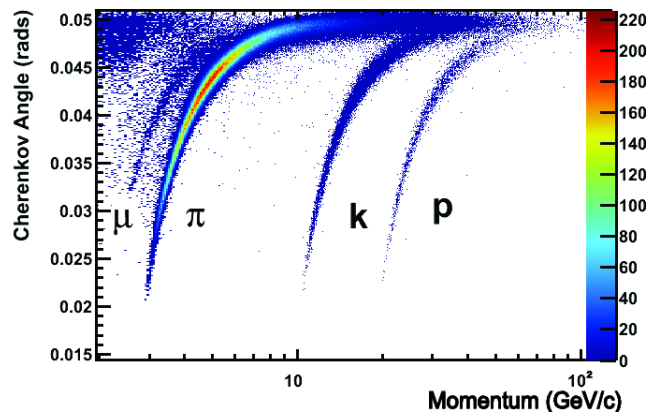
Figure 3.15: Reconstructed Cherenkov angle within the RICH system as a function of particle momentum obtained from $\sim$2% of isolated tracks selected from data [47].

In simulated data the distributions of these variables require calibration to more accurately describe the data. The *MeerkatPID* package which is stored under the *Urania* LHCb software project performs this calibration via one of two methods *PIDGen* or *PIDCorr*. For faster availability of calibration samples PIDGen does not preserve correlations between variables, therefore the time taken to produce calibration samples is faster than PIDCorr and so they are more readily available for each year of MC. However for analyses where these correlations are required (e.g. in the training of a classifier) PIDCorr samples must be used as these more accurately model the real data. Both methods make use of the software *Meerkat*, a C++ library built on top of ROOT which performs kernel density estimates (a method which

does not rely on parameterisation to estimate a probability distribution function) in multiple dimensions [48]. The estimation is performed using a binned kernel density for better computational time and lower memory usage.

For both methods the variables of η, p_T and N_{tr} (the pseudorapidity, transverse momentum and number of tracks for each event respectively) are used to construct a normalised Probability Distribution Function (PDF) representing the distribution of the PID variable:

$$P(x|\eta, p_T, N_{tr}) = \int_{-\infty}^{x} f(t|\eta, p_T, N_{tr})dt, . \tag{3.9}$$

In the case of PIDGen a new dataset of the variable is then generated by randomly selecting values of x using the inverse $P^{-1}(y)$ within the range $[0, 1]$, the original variable contained within MC is discarded.

For PIDCorr the process is very different. The MC variable x_{MC} is kept and the probabilities are extracted using Equation 3.9. An probability function is then obtained from the calibration data sample and the inverse P^{-1}_{Data} is applied as a correction to x_{MC}:

$$x_{corr} = P^{-1}_{Data}(P_{MC}(x_{MC}|\eta, p_T, N_{tr})|\eta, p_T, N_{tr}). \tag{3.10}$$

Meerkat is used to obtain the four-dimensional PDF after the distributions describing the input variables have been made more uniform. An example showing the distributions of the variable `ProbNNmu` for the channel of $K^{\pm} \to \pi^{\pm}\mu^+\mu^-$ before and after correction using the approach of PIDGen is shown in Figure 3.16.
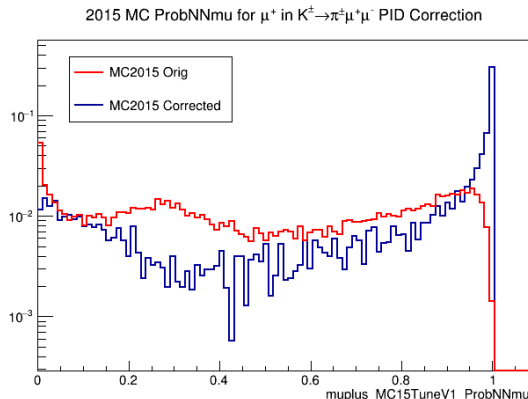
Figure 3.16: The PID variable `ProbNNmu` applied to μ^+ within $K^\pm \to \pi^\pm \mu^+ \mu^-$ 2015 Monte Carlo before in the MC before and after reprocessing using PIDGen. Clear after correction is the expected peak at a probability of 1.

3.5   Simulating LHCb Data

For the production of MC samples, contained within the LHCb Software Framework is a 'wrapper' application known as GAUSS which contains both the event generation process and the emulation of detector response to event particles carried out by the GEANT4 framework. GAUSS applies any cuts, such as keeping only events which fall within the LHCb geometry, as well as detector conditions stored in databases. Events created by GAUSS are stored to file before being passed through the later stages of simulation and subsequently the stages of data flow including triggering and stripping.

3.5.1   Event Generation

In general MC production at LHCb begins with generator programs such as PYTHIA, a standalone generator of high energy physics events written in C++. Its use has covered a wide range of studies including production cross sections, and samples created to determine detector capability in new physics searches.

Simulation of the decay of heavy flavour particles such as B and D mesons is

handled using EVTGEN. The framework builds on top of the PYTHIA libraries incorporating the PHOTOS algorithm, which is used for QED corrections to the decays of resonances [49]. Within EVTGEN new decays are added as submodules labelled as models [50]. Unlike other event generators the production process is centred around decay amplitudes as opposed to probability. Decay chains are simulated using the amplitudes at each stage. In addition EVTGEN also includes CP violation and $B^0 \bar{B}^0$ mixing using the properties of particle mass and decay width.

Although there are many types of MC defined within the framework, the most commonly requested for analyses at LHCb is *Phase Space* MC (`PHSP`) where particles are generated from the phase space, and spins of the parent and daughter particles are averaged. Whether or not a generated decay chain is a valid production and hence should be stored is decided via an accept-reject algorithm based on the probability obtained from the decay amplitude. To save having to regenerate the kinematics from phase space for a whole decay chain if this probability is inadequate, the chain is created in stages as a set of sub-decays.

For those events consisting of B_c decays a generator called BCVEGPY was constructed in FORTRAN in order to be compatible with PYTHIA 6. The package is used to simulate the hadronic decays using processes of the form $gg \to B_c(B_c^*) + b + c$ [51]. The MC productions for $B_c^\pm \to \phi K^\pm$ in the outlined B_c analysis in this thesis have been created using the package.

With the increasing requirement in production statistics for LHCb, methods for reducing CPU usage have been introduced into the MC generation process of which the *ReDecay* module is an example. Within ReDecay a complete event is generated which includes both the signal particle, let's say for example a B_c^+, and the rest of the event. The position of the production vertex and four-momentum vector for the B_c^+ are then recorded. The as yet undecayed signal particle is then removed from

the event, and the rest of the event (ROE) passed through GEANT4 to simulate detector response, the information, including MC truth information and energy deposits within the calorimeters, then being written to disk. Then using the held information on B_c^+ vertex and four-momentum, new B_c^+ particles are generated and allowed to decay within GEANT4, the position and decay mode being allowed to vary. These generated signal decays are then merged with the same stored ROE information [52]. On average the rate of simulation of such decays is increased by a factor ~ 30 in production time.

3.5.2   The Modelling of LHCb Physics with GEANT4

GEANT4 is designed to simulate particle response to media as well as model the physics processes surrounding the initial interaction and those of any daughters produced as a result. The framework has been incorporated into various analyses including accelerator physics, medical studies and applications in astrophysical analyses [53]. A representation of the experiment environment is constructed using the implemented geometry classes; in the case of LHCb the full detector is modelled, the sub-detectors and support structure all being included to allow run conditions to be simulated as accurately as possible. As each element is defined as a separate physical volume they can be switched on or off depending on the properties of the investigation. This is very useful towards the research and development process as part of detector upgrading, and for comparing the effects of different detector configurations.

The simulated physics processes and their probability of occurrence are all described within special classes called *physics lists*; these are based on models describing, for example, elastic and inelastic hadronic processes, Coulomb scattering and pair production for electromagnetic processes. They are combined into a single class to describe physics within different energy ranges. A fine tuned selection of these

models is then used to accurately model behaviour within the detector. As an example, in LHCb simulation validation the physics lists implemented are customised versions of *FTFP_BERT* and *QGSP_BERT* set to model behaviour in the detector. Both lists use the *Bertini* intra-nuclear model [54] but at different kinetic energy thresholds of below 5 and 9.9 GeV respectively. In the latter list the *Low Energy Parameterised* (LEP) model is implemented at a range of 9.5 to 25 GeV, and then gradually superceded by the *Quark-Gluon-String* and, precompound and evaporation models (QGSP) [55], at energies greater than 12 GeV. For FTFP_BERT the *Fritiof* model is used at energies above 4 GeV followed by a combination of Precompound and *Reggeon* cascade models (giving FTFP) [56]. Within each overlap region the probability of selecting between the conflicting models varies linearly with increasing energy.

For performing simulated measurements of the properties of particle interactions with various media, GEANT4 includes a *ParticleGun* class which allows the placement of a particle source within the geometry. Amongst the parameters available at initialisation are the choice of particle, the direction and the momentum/energy. A event is generated in which a single particle is fired into a geometry and the simulated information of vertices and primary particles is then stored for later interpretation by the LHCb reconstruction and analysis framework.

GEANT4 4 is pre-configured for LHCb simulation with additional physics lists and the detector geometry being implemented within a custom build of the software. This is coupled with the event generation process to form the Gaudi based program 'GAUSS' which acts as a 'wrapper' also adding the capability for further options to be defined by the user via simple Python based scripts. At runtime the production steps, including in addition the emulation of the L0 hardware trigger, are then automated by the application [57]. GAUSS is used predominantly in the production of Monte Carlo for analyses, however it also acts as an important asset in the

proposal and development of future upgrades at LHCb; including the design of new hardware components and the optimisation of software level triggering, providing a way of measuring the efficiency and the response of the detector as a whole with such modifications.

The properties of decays to be simulated are defined in special configuration files known as *DecFiles* where a decay descriptor is given along with any cuts to be applied at generation level. GAUSS parses these options during the production.

3.5.3   Digitisation with Boole

The Gaudi application *Boole* performs the digitisation process of converting MC data to be equivalent to 'raw format' real data that has been obtained by the detector, emulating the response of the detector and readout electronics.

3.6   LHCb Software Monitoring (LHCbPR2)

To ensure continuity in LHCb software if any modifications are made to the constituent applications, a system of 'nightly' building of the software is orchestrated by the continuous integration client *Jenkins*. Jenkins is able to fetch any pending changes from the relevant repositories and re-build the software displaying results for review on a daily basis in the form of `lhcbnightlies`. However such results can only provide information on compilation/coding errors. The LHCbPR2 (LHCb Progress and Regression v2) framework has been designed as a tool for monitoring changes relating to software output; a set of benchmark tests have been created as minimal examples from which a comparison can be made using numerical data. The Birmingham LHCb group are among those responsible for maintaining the tests relating to GAUSS

and GEANT4. These tests include the monitoring of radiation and interaction length information across the sub-detectors within LHCb, and a simulated investigation into the hadronic cross-sections and multiplicities for various sample materials. Results are displayed within a web based frontend in which histograms produced by the tests can be directly compared between build versions under different environments. This is particularly important for the migration between GEANT4 version 9 to 10, as well as the move from CMT to CMake for compilation.

The three tests outlined in the following sections were implemented into LHCbPR by the author and maintained to ensure compatibility with each software version. Each test is based on an existing simulation which has been adapted and modified to allow for a range of parameters and automated running. The choice of these parameters and the conditions/geometries within the tests have been selected based on close consultation with the simulation group.

3.6.1   Radiation Length & Absorption Test

As the principal method by which events are recorded in a particle detector is the interaction of collision products with a material, such as silicon within the tracker, the response of LHCb to such particles needs to be understood.

In addition to energy loss through ionisation, a particle passing through a medium is subject to multiple deflections due to Coulomb scattering from the constituent atomic nuclei. The distribution of the deflection angles is Gaussian following the convention of the central limit theorem [58]. The width of this distribution is dependent on the particle momentum as well as a property of the material known as *radiation length*, X_0. The acceleration and deceleration from the force induced by the electromagnetic fields leads to loss of energy through photon radiation, a process known as *bremsstrahlung*, this process typically occurs with electrons.

For the case of relativistic electrons the rate of energy loss is given by:

$$-\frac{\mathrm{d}E}{\mathrm{d}x} \approx \frac{E}{X_0},$$

(3.11)

where E is the energy of the electron, when integrated this gives:

$$E \approx E_0 e^{-x/X_0},$$

(3.12)

thus X_0 is defined as the distance in which the energy of the particle drops by a factor e [59].

Yung-Su Tsai defines the unit radiation length of a material [60] to be:

$$X_0 = \frac{716.405\mathrm{A}}{\left[Z^2(\mathrm{L}_{rad} - \mathrm{f}) + Z\mathrm{L}'_{rad}\right]}$$

(3.13)

with Z being the atomic number of the material element, where the expressions L_{rad} and L'_{rad} are the radiation logarithms $\ln\left(AZ^{-1/3}\right)$ and $\ln\left(BZ^{-2/3}\right)$ respectively (with the values of A and B depending on the model choice) and f is the Coulomb correction. The radiation lengths of typical materials within the LHCb detector obtained experimentally are given in Table 3.3.

Table 3.3: Calculated values of radiation lengths for typical materials within the LHCb detector [61].

Element	Z	$X_0/\mathrm{g} \cdot \mathrm{cm}^{-2}$
Al	13	26.9815
Si	14	28.0855
Ar	18	39.948
Fe	28	58.6934
Pb	82	207.2
CO_2	-	36.2

Within the simulation process for generating Monte Carlo, the particles from each simulated collision are passed through GEANT4 which emulates behaviour according to the properties of the traversed materials as read from a database.

Another property of interest is the *nuclear interaction length*, the mean distance traversed by a hadronic particle before undergoing a nuclear interaction within the detector material. At relativistic limits this can be defined as either the absorption length:

$$l_a = 1/n\sigma_{inel}, \tag{3.14}$$

where n is the number density and σ_{inel} is the inelastic cross-section, or as the collision length:

$$l_c = 1/n\sigma_{tot}, \tag{3.15}$$

σ_{tot} being the total cross-section, as at these energies $l_a \approx l_c$ [59]. The quantity analogous to radiation length is the nuclear interaction length, λ_I, the depth within a material at which the number of charged particles drops by a factor e.

(a) All other scoring planes shown in situ.

(b) The VELO shown alongside Scoring Plane 1.
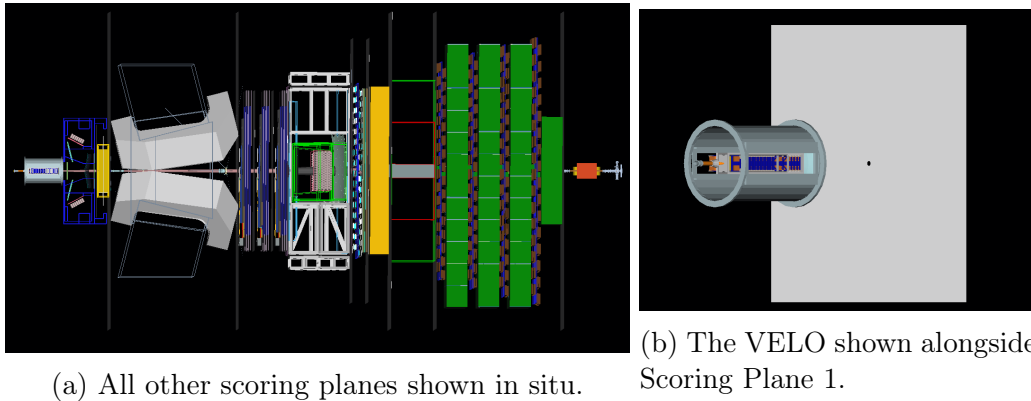
Figure 3.17: Visual images of the detector and scoring planes created using the *Panoramix* project within LHCb software.

Included as part of GAUSS benchmarking is the *RadLength* test; this runs a simulation of 50,000 events in which a particle gun fires a single muon neutrino, due to the low interaction probability with matter, at intervals along the beam axis within a modified version of the LHCb GEANT4 geometry. These neutrinos are generated at random with an energy of $50\,\text{GeV}$ within a plane defined by the azimuthal angle ϕ and a pseudorapidity range $\eta[2, 5]$. For the first part of this test a measurement of the number of radiation and nuclear interaction lengths after each sub-detector is

recorded. GEANT4 collects information using unphysical geometric objects known as scoring planes which are added to the geometry to mark out locations for which measurements should be taken during the simulation. The test is executed in two parts.

A simulation in GEANT4 consists of a set of special classes used to define the various phases of setup and automation. The *G4SteppingAction* class provides a method for extracting information from a simulation at a given point during its execution. In the case of the RadLength test this is information relating to the properties of the volume traversed by a simulated particle between each of the scoring planes, with the class having access to the simulation state before and after the motion. The test is built around the LHCb custom `RadLengthColl` tool which performs the simple calculation of dividing the displacement/step size by the radiation/interaction length of the traversed region. For the first part of the test, the difference in value before and after a sub-detector is recorded as a 'Plane-to-Plane' measurement, and the overall number of radiation/interaction lengths up to a sub-detector boundary is measured as a 'Cumulative' measurement. Results are then used to construct a set of two dimensional profile histograms for each sub-detector plotted within the $\eta - -\phi$ plane, as well as graphs displaying the cumulative number of lengths as a function of z, η and the ID of each scoring plane. Example profiles for the VELO are shown in Figure 3.18, the most abundant region being the location of sections of the beam pipe and the RF foil. As the VELO is located around the collision centre, it is the most irradiated part of the LHCb detector.

The second part of the test consists of an additional scan performed across the VELO positioning the particle source at intervals of 10 mm along the z axis and moving downstream. This time the LHCb geometry is stripped back to only the VELO and first scoring plane, with the average number of the radiation/interaction lengths being recorded at a point just downstream of the sub-detector, the results of

the scan are shown in Figure 3.19. The errors on the data points are calculated from the RMS values normalised to the entries in the histogram bin for each distance. The results of the full test are displayed online within the LHCbPR2 webpages to be compared for different builds of Gauss.
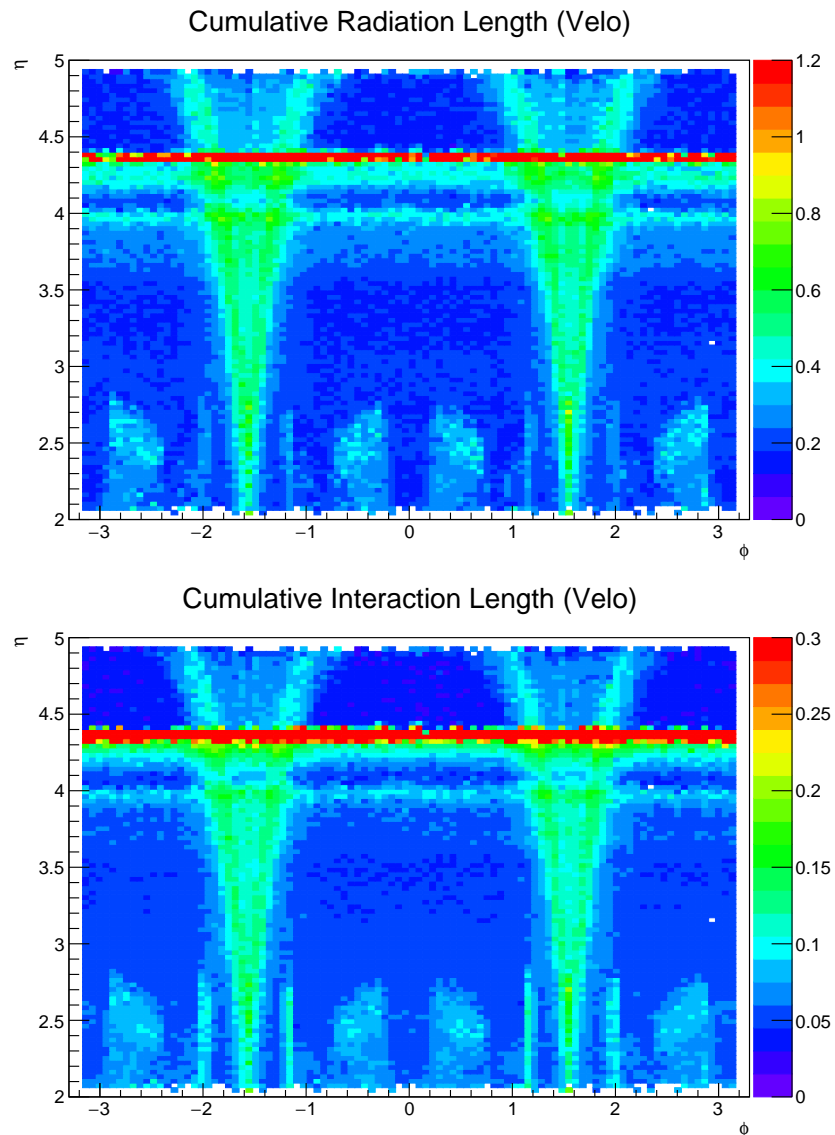
Figure 3.18: Binned profiles of the number of radiation and interaction lengths across the whole VELO projected in the $\eta - \phi$ plane.
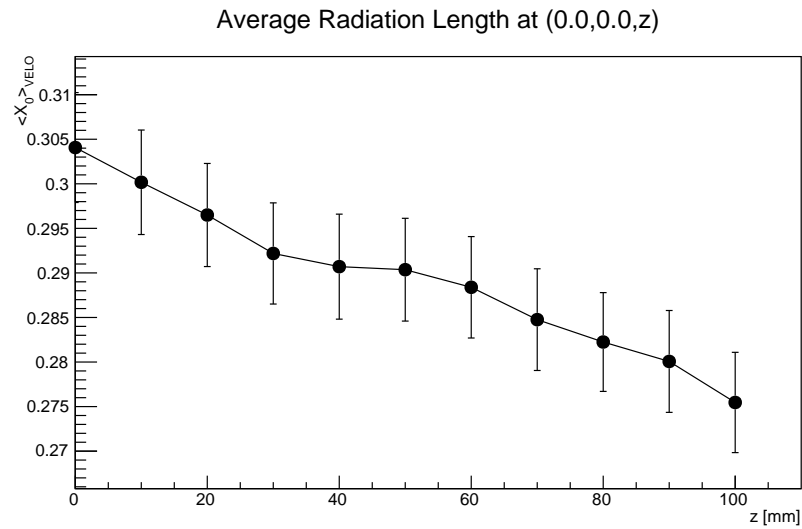
(a) Average number of radiation lengths.
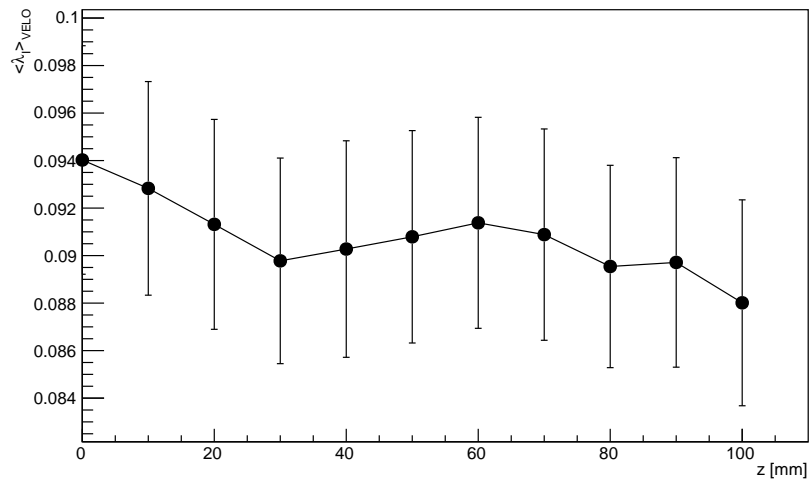
(b) Average number of interaction lengths.

Figure 3.19: Radiation and interaction length scans of the VELO with average readings taken after positioning the particle gun at 10 mm intervals in the z direction performed within Gauss.

3.6.2   Hadronic Multiplicity & Cross Section Test

As a measure of consistency between the standalone GEANT4 physics databases and simulations conducted through GAUSS, a test is included to obtain the multiplicities and cross-sections for various particles traversing beryllium, aluminium and silicon, materials abundant within LHCb. In contrast to the RadLength test, the geometry in this case is a simple block of material positioned perpendicular to the beam axis at z positions matching those of the relevant sub-detector components. A particle gun is created from which $K^{\pm}$, $\pi^{\pm}$ and $p^{\pm}$ particles are fired at energies within a logarithmic range of between 1 and 100 GeV. The GEANT4 physics lists of QGSP_BERT and FTFP_BERT are used to compare the simulation of physics processes by the different underlying models, these lists being chosen by LHCb during the development of GAUSS. Furthermore the effect of material thickness is also observed by iterating through values of 1, 5 and 10 mm. Within GAUSS is the `GaussTargetMultiplicity` tool built around the `G4TrackingAction` class which gives a 'preview' of a particle's trajectory information once a GEANT4 step has completed. The tool monitors the daughters produced by the interactions during the simulation and logs the categories of inelastic/elastic collision and neutral/charged daughters by looking at the process type, adding entries to data trees which are written to file. The abundance within each category is obtained by iterating through these daughters to determine the fraction of events which have at least one inelastic/elastic collision, these fraction then being labelled as the relevant cross-section.

The definition of multiplicity within the test is the number of secondary particles produced, with the exception of heavy nuclei which are not counted. Taking the examples shown in Figure 3.20 we see, as expected, that pions fired at higher energies towards a 10 mm beryllium target induce a higher rate of hadron production. Also evident is the subtle deviation between the QGSP_BERT and FTFP_BERT models for these energies due to different methods used to simulate physics within each.

Inelastic Probability of Interaction in 10 mm of Aluminium
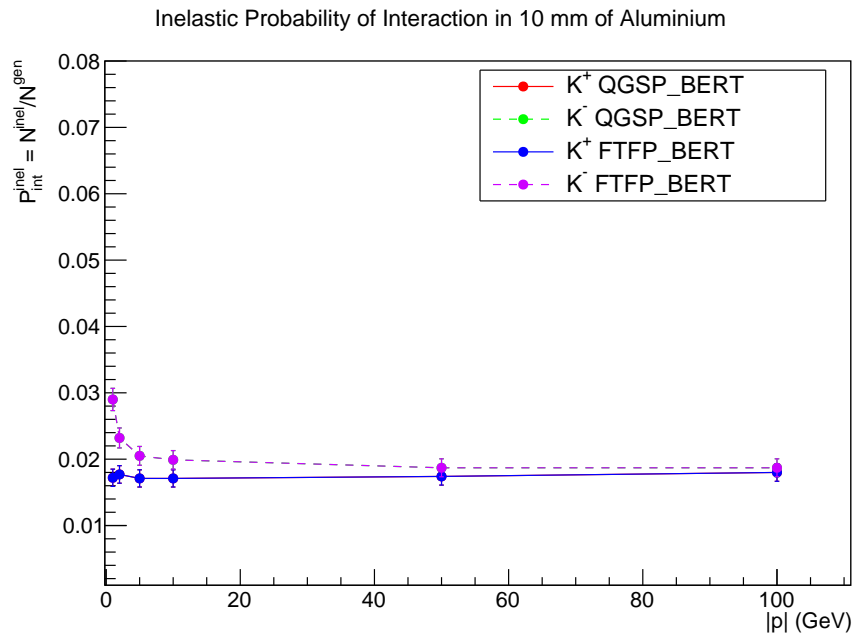
(a) The inelastic probability of interaction for kaons hitting a 10 mm aluminium target.

Multiplicity of Secondaries in 10 mm of Beryllium
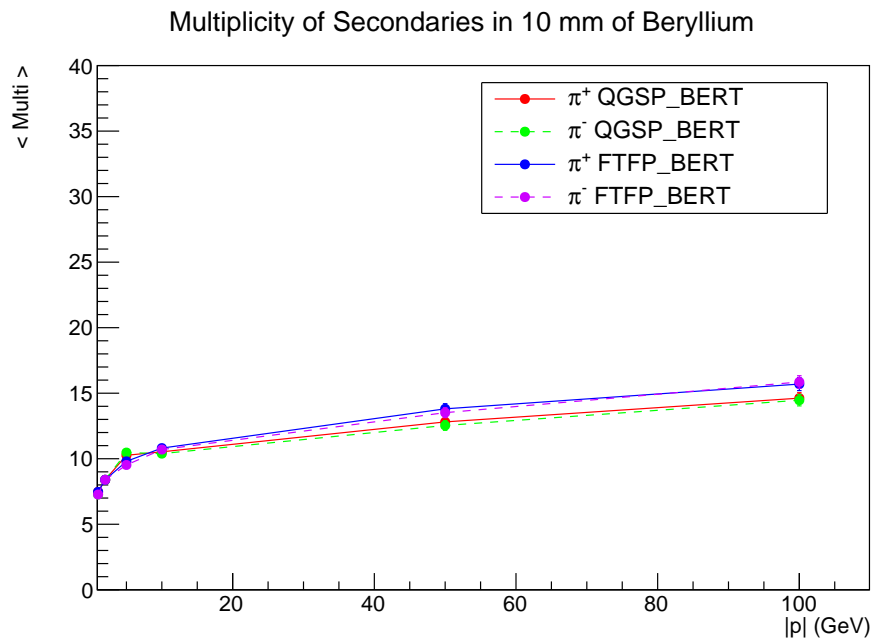
(b) The multiplicity of secondaries produced when firing pions at a 10 mm beryllium target.

Figure 3.20: Examples plots from the Hadronic Cross Section & Multiplicity test. An increasing energy leads to a reduced inelastic collision probability and increased hadronic multiplicity, the exact relationship depending on the choice of physics list used within GEANT4.

3.6.3   Gamma to DiLepton Conversion Test

In 1928 Paul Dirac put forward the Dirac equation and later postulated the existence of a particle with mass equivalent to that of the electron but with opposite charge [62], the positron. This was later confirmed with the discovery by Carl D. Anderson in 1932 [63]. The process of *pair production* is the event whereby a photon with energy greater than twice the mass of a particle is converted to a particle-anti-particle pair in the presence of a nucleus. The nuclear interaction satisfies the requirement for conservation of energy and momentum, if no nucleus was present this would imply a rest frame where the photon momentum is zero. The photon interacts with the electromagnetic field of the nucleus and is recoiled (see figure Figure 3.21). 2D histograms showing relations between the separation angle between the two leptons produced and their invariant mass at different energies are shown in Figure 3.22.
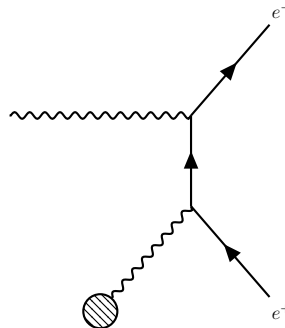
Figure 3.21: Feynman diagram showing the pair production process in the presence of a nucleus.

To simulate pair production of muons and electrons within the RF foil of the VELO, a new test has been created based on the existing standalone example *TestEm6* included within GEANT4 [64]. A particle gun firing photons at energies in the range 1 to 100 GeV is directed at a 300 μm target of aluminium. For those events whereby an electron or muon pair is produced through gamma conversion, the properties of invariant mass of the pair M_{ll}, angle between the momenta of the two leptons in the l^+ rest frame $\theta_{p_{l+},p_{l-}}$, and the fraction of photon energy for each lepton are

recorded. Unlike the previous tests, TestEm6 contains a custom physics list with a stripped down selection of electromagnetic processes requiring only those related to conversion. In addition, due to the very low probability of gamma to dimuon conversion, the cross section for this process can be artificially increased using the purpose built command contained within the list. For the purpose of this analysis the default factor of 1000 already chosen within the existing test was utilised, the effect on the probability of a $\gamma \to \mu^+\mu^-$ is shown in Table 3.4. Results from the test show clearly the correlation between $\theta_{p_{l+},p_{l-}}$ and M_{ll}, as expected an increase in energy leads to smaller angular separation angle with a smaller separation between electrons compared to the heavier muons.

Table 3.4: The probability of a $\gamma \to \mu^+\mu^-$ event for a given energy with and without the factor 1000 increase in the process cross section.

Energy/GeV	$P(\gamma \to \mu^+\mu^-)$	
	σ	$\sigma \times 10^3$
10	$(7.00 \pm 2.65) \times 10^{-6}$	$(7.61 \pm 0.01) \times 10^{-3}$
100	$(2.30 \pm 0.48) \times 10^{-5}$	$(1.76 \pm 0.01) \times 10^{-2}$
1000	$(3.10 \pm 0.56) \times 10^{-5}$	$(2.80 \pm 0.01) \times 10^{-2}$

3.6.4   Summary

The purpose of these three tests is to act as benchmark tests to ensure compatibility between different versions of GEANT4 and GAUSS by analysing various simulated physical processes both within the LHCb geometry and simpler single material geometries. The implementation of these tests into the LHCbPR framework by the author has allowed faster observation to be made into not only the effects of software alterations but also changes to the LHCb geometry itself as part of investigations towards future detector upgrades. With techniques in software and workflow altering regularly over time this provides an effective way of being able to implement the latest in software technology. A better understanding of properties such as radiation length and particle production within materials aides in the development of upgrades.

(a) 10 GeV, $\gamma \to \mu\mu$

(b) 10 GeV, $\gamma \to ee$

(c) 100 GeV, $\gamma \to \mu\mu$

(d) 100 GeV, $\gamma \to ee$

(e) 1000 GeV, $\gamma \to \mu\mu$

(f) 1000 GeV, $\gamma \to ee$
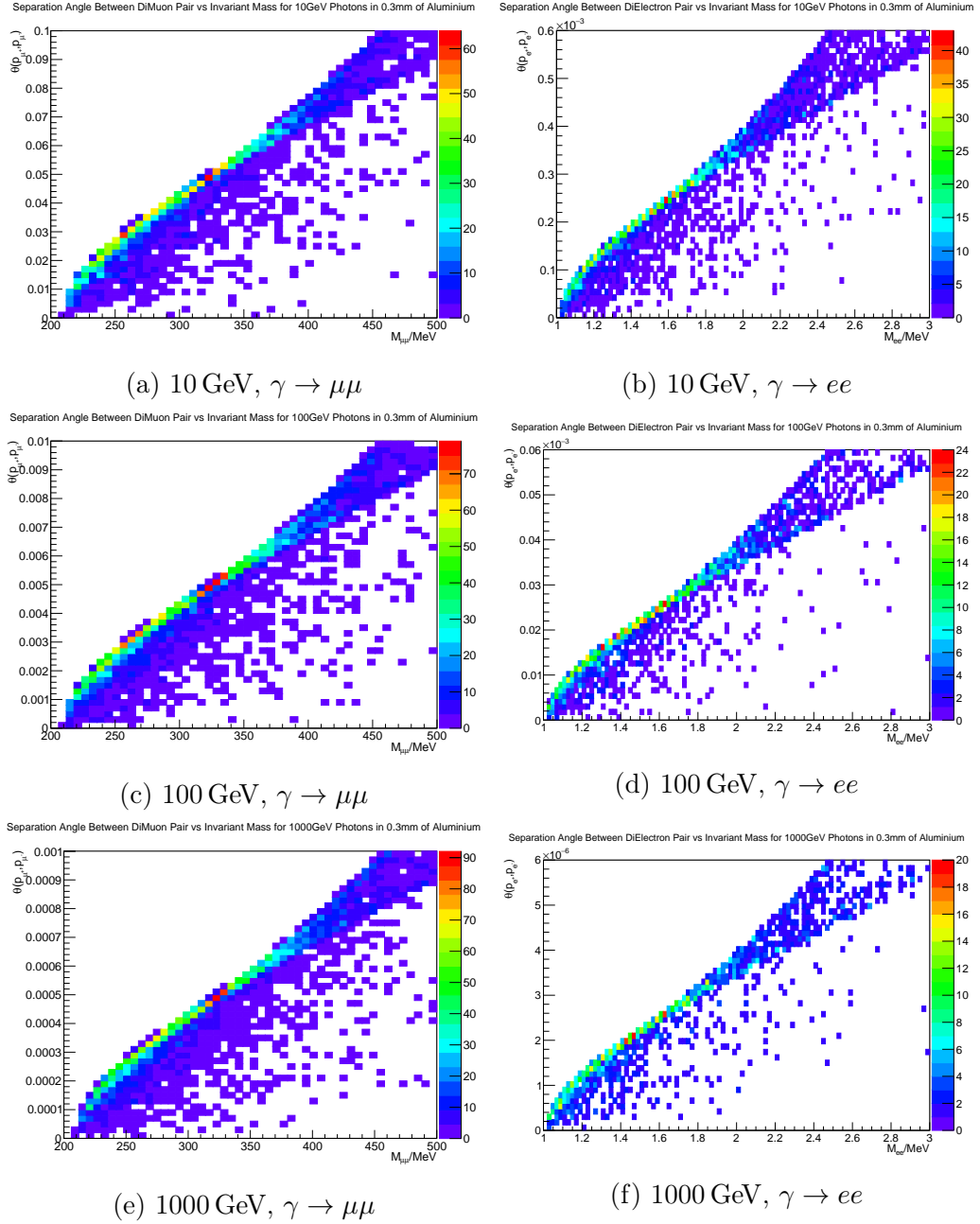
Figure 3.22: Histograms showing separation angle between the two lepton momenta in their rest frame vs invariant mass in dilepton production simulated in GEANT4.

Chapter 4

Kaon Physics at LHCb

4.1 Strange Physics

Particles containing an s quark exhibit a property known as 'strangeness', a quantum number initially introduced as a means of explaining the unusual behaviour of these hadrons which are produced via strong interactions but decay weakly. Kaons are strange mesons formed of combinations of a single strange quark with a first generation (u or d) quark.

The neutral kaon system is formed of two mass eigenstates K^0 and $\bar{K}^0$ which have strangeness of -1 and +1 respectively. Under CP transformation they transform one into other:

$$CP\left|K^0\right\rangle = -\left|\bar{K}^0\right\rangle \tag{4.1}$$

and assuming conservation of CP symmetry can be combined linearly to form the

two CP eigenstates:

$$K_1 = \frac{1}{\sqrt{2}}(\left|K^0\right\rangle - \left|\bar{K}^0\right\rangle) \tag{4.2}$$

$$K_2 = \frac{1}{\sqrt{2}}(\left|K^0\right\rangle + \left|\bar{K}^0\right\rangle). \tag{4.3}$$

Applying the CP operator, we see that K_1 and K_2 are CP even and CP odd respectively:

$$CP\left|K_1\right\rangle = +\left|K_1\right\rangle$$

$$CP\left|K_2\right\rangle = -\left|K_2\right\rangle.$$

For kaons the most probable weak decays are those involving pions, with the CP conserving decays of $K_1 \to \pi\pi$ and $K_2 \to \pi\pi\pi$ dominating, the mass change within the decay, hence the number of daughter pions, affects the decay rate giving rise to the lifetime eigenstates of K_S ('K-short') and K_L ('K-long') respectively.

In 1964 violation of CP symmetry was observed for the first time in the Fitch-Cronin experiment [65]. The expectation was that given a long enough decay volume, a beam of pure K_L could be produced with all K_S mesons decaying away due to the factor 100 difference in lifetime. However instead a non-zero contribution of $K_S \to \pi\pi$ decays was observed suggesting that either the symmetry was directly violated or that K_L and K_S are actually superpositions of K_1 and K_2 in the form:

$$\left|K_{S,L}\right\rangle = \frac{1}{\sqrt{1 - |\bar{\epsilon}|^2}}\left(\left|K_1\right\rangle \mp \left|K_2\right\rangle\right) \tag{4.4}$$

with CP conservation when $\bar{\epsilon} = 0$. Measurement of the decays of $K^0 \to \pi^- l^+ \nu_l$ and $\bar{K}^0 \to \pi^+ l^- \bar{\nu}_l$ provides a test of $\bar{\epsilon}$. These channels have the property of only being possible through the decay of K^0 or $\bar{K}^0$ but not both [66]. The parameter δ_L,

defined as [67]:

$$\delta_L \equiv \frac{\Gamma(K_L \to l^+\nu_l) - \Gamma(K_L \to l^-\bar{\nu}_l)}{\Gamma(K_L \to l^+\nu_l) + \Gamma(K_Lb \to l^-\bar{\nu}_l)}, \tag{4.5}$$

is a measurable quantity from which the real part of $\bar{\epsilon}$ can be deduced as:

$$\delta = \frac{2\mathrm{Re}(\bar{\epsilon})}{(1 + |\bar{\epsilon}|^2)} \tag{4.6}$$

with the non-zero experimental measurement of:

$$\delta = (3.32 \pm 0.06) \times 10^{-3} \tag{4.7}$$

confirming $\bar{\epsilon} \neq 0$ and CP to be violated.

Investigation into direct CP violation has been performed by the NA48 collaboration [68] through measurement of the ratio:

$$R = \left| \frac{K_L \to \pi^+\pi^-}{K_S \to \pi^+\pi^-} \right|^2 \tag{4.8}$$

$$\simeq 1 - 6\mathcal{R}e\left(\epsilon'/\epsilon\right) \tag{4.9}$$

with CP conservation being the case of $\epsilon' = 0$. The current accepted result deduced from measurement and fits is:

$$\mathcal{R}e\left(\epsilon'/\epsilon\right) = (1.66 \pm 0.23) \times 10^{-3} \tag{4.10}$$

4.1.1 $K^\pm \to \pi^\pm \ell^+ \ell^-$ Decays

The leptonic kaon decays $K^\pm \to \pi^\pm \ell^+ \ell^-$ are useful in deducing precisely the combined magnitude of the CKM matrix parameters V_{td} and V_{ts} (see section 2.5), as well as determining the low-energy structure in QCD, and also for searches into CP violation. These decays are dominated by the long distance γ-exchange mechanism

$K^{\pm} \to \pi^{\pm}\gamma^*$, the exchange of a single virtual photon under the condition of CP invariance [69], which is logarithmically dependent on the quark masses. This dominance is evident in the sensitivity of these decays to the light quark mass. The short-distance contributions of Z^0/γ and $W-W$ exchange are negligible in the calculation of a branching ratio for the decays [70].
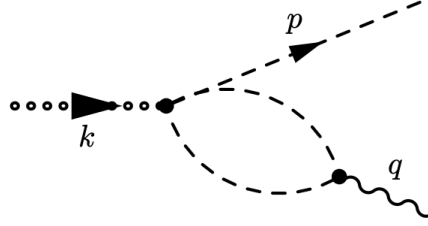
Figure 4.1: Single loop contribution in Chiral Perturbation Theory (ChPT) for $K^{\pm} \to \pi^{\pm}\ell^+\ell^-$ decays, the momenta of kaon, pion and photon being represented by k, p and q respectively [70]

The single virtual photon exchange results in the dilepton invariant mass $z = (M_{ll}/M_K)^2$ spectra [71]:

$$\frac{\mathrm{d}\Gamma}{\mathrm{d}z} = \frac{\alpha^2 M_K}{12\pi(4\pi)^4}\lambda^{3/2}(1, z, r_{\pi}^2)\sqrt{1 - 4\frac{r_l^2}{z}}\left(1 + 2\frac{r_l^2}{z}\right)|W(z)|^2, \qquad (4.11)$$

where:

$$r_X = m_X/M_K \qquad (4.12)$$

$$r_{l}, \pi = m_{l,\pi}/M_K \qquad (4.13)$$

$$\lambda(a, b, c) = a^2 + b^2 + c^2 - 2(ab + ac + bc) \qquad (4.14)$$

$$4r_l^2 \leq z \leq (1 - r_{\pi})^2 \qquad (4.15)$$

$W(z)$ are form factors in the complex plane, and α is the fine structure constant. At low energies the degrees of freedom are no longer fundamental particles but hadrons due to the available energy being insufficient to break apart the constituent partons.

The running of the strong coupling constant leads to quark confinement at low energy tending towards an asymptotic freedom as the energy increases; the large value of this coupling means that at the point of confinement the perturbative approach to QCD is no longer valid and the system can no longer be described using the perturbative expansions within Quantum Field Theory (QFT) [72]. As the relevant QCD partition function is as yet unsolved, an effective field theory known as Chiral Perturbation Theory (ChPT) is often chosen to describe the dynamics. An effective field theory contains terms from the parent theory but these are then collected in terms of like powers (a process known as 'power ordering') and assigned a degree of importance with those terms deemed negligible being temporarily ignored. In ChPT this ordering is performed on expansions of momenta and quark masses, and is based on symmetry of the QCD Lagrangian which is of the form $SU(3)_L \times SU(3)_R \times U(1)_V$ within the limit of the u, d and s being zero. It is the spontaneous breaking of this symmetry to $SU(3)_V \times U(1)_V$ which leads to the eight Goldstone bosons (with $U(1)_V$ arising from baryon number conservation) [73].

In the chiral expansion, those terms of the lowest order $\mathcal{O}(E^2)$ vanish due to the conservation of electromagnetic current, however the Next to Leading Order (NLO) contribution contains components from kaon and pion loops, and therefore does not vanish, countering the $\mathcal{O}(E^4)$ terms [74].

For the single photon exchange the amplitude of $K^\pm \to \pi^\pm \ell^+ \ell^-$ decays can be described in terms of the form factor $W(z)$ found in Equation 4.11. This can be parameterised under ChPT in the form [70, 71]:

$$W_+(z) = G_F M_K^2 W_+^{pol}(z) + V_+^{\pi\pi}(z) \tag{4.16}$$

with $W_+^{pol}(z) = a_+ + b_+ z$ describing the contribution of high mass states as a low order polynomial for the case of a charged kaon, and the term $V_+^{\pi\pi}(z)$ describing

effects from $\gamma^* \rightarrow \pi\pi$, this can be calculated using the $K^\pm \rightarrow \pi^\pm\pi^+\pi^-$ vertex illustrated in Figure 4.2. Comparisons between this parameterisation and data for $K^\pm \rightarrow \pi^\pm\ell^+\ell^-$ channels lead to large corrections which are are being theoretically addressed using the technique of lattice QCD [70]. The hadronic uncertainties for these decays are addressed within ChPT using the parameters a and b which are known as Low Energy Constants (LECs), with years being spent by theorists in understanding their nature. Some LECs are calculated phenomenologically by comparing ChPT with the Standard Model, others are obtained from low energy data by examining scattering and kaon processes. The use of lattice QCD has strengthened prediction of LEC values which has led to better precision in semileptonic compared to non-leptonic decays [69]. For $K^\pm \rightarrow \pi^\pm e^+e^-$, data from the results
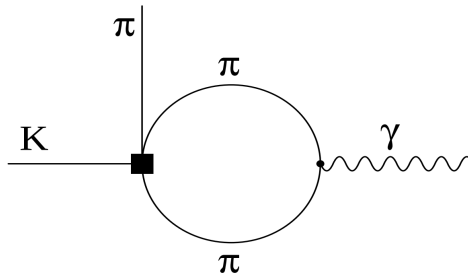
Figure 4.2: The $K^\pm \rightarrow \pi^\pm\pi^+\pi^-$ contribution to $K \rightarrow \pi\gamma^*$ vertex used in calculation of the Chiral Perturbation Theory (ChPT) form factor $W(z)$ [71].

collected by the NA48/2 and E865 collaborations have been used to determine the parameters a and b which are found to contradict theoretical expectation from chiral counting of $b < a$, there in addition being no explanation for why $|a/b| \sim 1$ [74]. The parameters, estimated on the basis of different experimental results, are shown in Table 4.1. When these data are combined with those for $K^\pm \rightarrow \pi^\pm\mu^+\mu^-$ an additional measurement of the ratio $R_{K^\pm}$ can be performed defined as:

$$R_{K^\pm} = \mathcal{B}(K^\pm \rightarrow \pi^\pm\mu^+\mu^-)/\mathcal{B}(K^\pm \rightarrow \pi^\pm e^+e^-) \qquad (4.17)$$

this ratio is a sensitive test for Lepton Universality Violation with the SM expectation

being for $R_{K^{\pm}} \sim 1$; the current average obtained by the PDG from multiple experiments is found to be 0.313(71) [74].

Table 4.1: Results obtained from NA48/2 and E865 data for the parameters in the parameterisation of the form factor $V(z)$ [74].

Experiment	a_+	b_+
$[e^+e^-, \text{E865}]$	-0.573(23)	-0.662(57)
$[e^+e^-, \text{NA48/2}]$	-0.535(20)	-0.771(65)
$[\mu^+\mu^-, \text{NA48/2}]$	-0.40(10)	-1.10(21)

4.1.2   The Rare Strange Decay of $K^{\pm} \to \pi^{\pm}\mu^+\mu^-$

The decay of $K^{\pm} \to \pi^{\pm}\mu^+\mu^-$ is one of several kaon channels being investigated as part of prospects analyses within the strange physics programme at LHCb [75]. Although the detector is not optimised for long lived particles such as $K^{\pm}$, the investigation forms a benchmark study into the capability of collider experiments in strange physics. With ChPT a theoretical prediction for the decay rate has
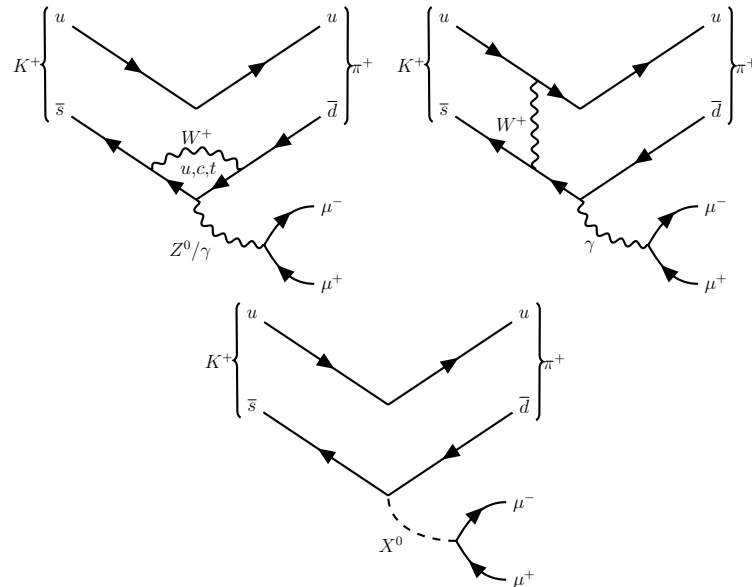
Figure 4.3: Examples of Feynman diagrams for $K^{\pm} \to \pi^{\pm}\mu^+\mu^-$ showing (Top Left)the SM short distance electroweak 'penguin' contribution, (Top Right)the long distance contribution and (Bottom)a possible contribution from new physics.

been made by S. Friot et. al. (2004, 2005) [76, 77] using the measurement of the

invariant mass distribution and the rate of $K^\pm \to \pi^\pm e^+ e^-$ recorded by the E865 experiment [78] to obtain:

$$\mathcal{B}(K^\pm \to \pi^\pm \mu^+ \mu^-) = (8.7 \pm 2.9) \times 10^{-8}, \tag{4.18}$$

and alternatively by Dubnickova et. al. (2006) [79] via parameterisation of the rate of $K^\pm \to \pi^\pm \ell^+ \ell^-$ decays in terms of the intermediate resonances from the ChPT expansion, giving a rate of:

$$\mathcal{B}(K^\pm \to \pi^\pm \mu^+ \mu^-) = (1.2 \pm 0.3) \times 10^{-7}. \tag{4.19}$$

Experimentally the current branching ratio measurement average is [12]:

$$\mathcal{B}(K^\pm \to \pi^\pm \mu^+ \mu^-) = (9.4 \pm 0.6) \times 10^{-8}, \tag{4.20}$$

with the main contribution being the latest measurement by the NA48/2 collaboration [80]:

$$\mathcal{B}(K^\pm \to \pi^\pm \mu^+ \mu^-) = (9.62 \pm 0.21_{\text{stat}} \pm 0.11_{\text{syst}} \pm 0.07_{\text{ext}}) \times 10^{-8}, \tag{4.21}$$

the third component of uncertainty arising from the use of $K^\pm \to \pi^\pm \pi^+ \pi^-$ as a normalisation channel. The fit performed to all measurements recorded in the Particle Data Group listings (PDG) thus far is shown in Figure 4.4. As well as a better understanding of ChPT, when phenomenological predictions for such measurements improve, results from experiment could help place constraints on new physics.
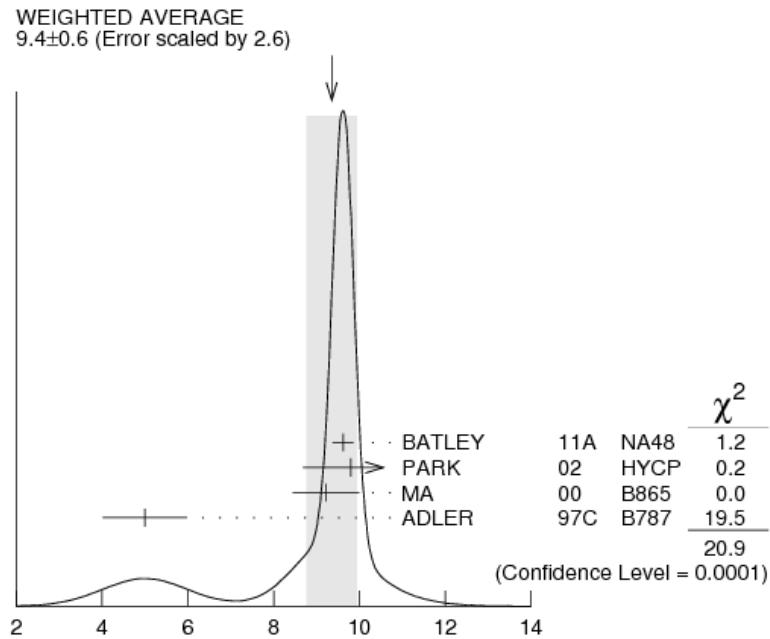
Figure 4.4: Fit to all PDG recorded experimental measurements of the $K^\pm \to \pi^\pm \mu^+ \mu^-$ branching ratio [12].

4.1.3 Heavy Neutrino Physics

Currently the existence of right handed chiral states for all particles has been confirmed, the measured non-zero neutrino mass goes on to imply that such states must exist also for neutrinos. A possibility is that rather than neutrinos and antineutrinos being two separate particle species (Dirac particles), they are in fact Majorana particles where both particle and anti-particle are a single state. This could explain why so far only left handed neutrinos and right handed neutrinos have been observed. Direct observation of these right handed states could provide further evidence towards an understanding of why neutrino mixing occurs, and give rise to extensions to the SM Langrangian, an example of which is the Neutrino Minimal Standard Model (νMSM) [81].

Alongside the rare channel is the prospect of measurement of the analogous Lepton Number Violating mode $K^\pm \to \pi^\mp \mu^+ \mu^+$ which has been theorised - among other

models - through the process shown in Figure 4.5 if the existence of Majorana neutrinos can be justified. the current limit as set by the NA48/2 experiment is:

$$\mathcal{B}(K^{\mp} \to \pi^{\mp}\mu^{+}\mu^{+}) < 1.1 \times 10^{-9}, \tag{4.22}$$

at a 90% Confidence Level [12].
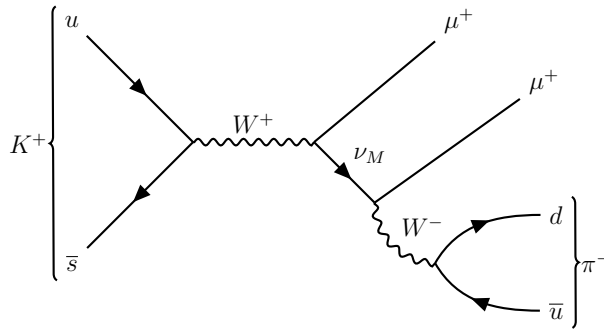
Figure 4.5: Candidate Feynman diagram for the 'wrong sign' decay $K^{\pm} \to \pi^{\mp}\mu^{+}\mu^{+}$ via Majorana heavy neutrinos.

The νMSM extension, if proven, could also provide answers to the question of what are the constituents of dark matter, as well as help explain the cause behind the apparent asymmetry of baryons in the universe.

Central to these theories is the 'seesaw' mechanism which proposes the existence of three 'heavy' partners to every flavour of light neutrino each having a mass that lies within the eV to GUT scale. This can be described quantitatively as:

$$m_L = -m_D M_R^{-1} m_D^T \tag{4.23}$$

where m_L, m_D and M_R are the masses of the observed light neutrino states, the neutrino Dirac matrix, and the Majorana mass matrix for the heavy neutrino states (which obey the Majorana condition $\nu = \bar{\nu}$) respectively [82].

Although such a measurement is not reported as part of the analysis outlined

within this thesis, with further statistics as planned for Run 3 of LHCb data taking, and the increased sensitivity due to the introduction of more dedicated triggering, the experiment could play a critical role in more precise measurement of $K^\pm \to \pi^\pm \mu^+ \mu^-$, comparing with further refined theoretical predictions to test for possible new physics.

4.2   Prospects for $K^\pm \to \pi^\pm \mu^+ \mu^-$ at LHCb

Analysis into $K^\pm \to \pi^\pm \mu^+ \mu^-$ has been performed on the $4\,\mathrm{fb}^{-1}$ of long tracks data taken between the years 2015 and 2017. The $K^\pm$ lifetime of $(1.238 \pm 0.002) \times 10^{-8}\,\mathrm{s}$ [12] gives a mean decay distance $\beta\gamma c\tau$ of $172\,\mathrm{m}$ at the average $p_z(K^\pm)$ of $22\,\mathrm{GeV}$ (see section A.3), additional coverage beyond the VELO to the first tracking station extends the decay volume from 1 to $8\,\mathrm{m}$:

$$\beta\gamma c\tau \quad = \quad \frac{p_z}{M}c\tau \tag{4.24}$$

$$= \quad 171.8 \tag{4.25}$$

$$\tag{4.26}$$

$$\frac{\int_0^{z_2} e^{x/\beta\gamma c\tau}}{\int_0^{z_1} e^{z_1/\beta\gamma c\tau}} \quad = \quad \frac{e^{8/172} - 1}{e^{1/172} - 1} \tag{4.27}$$

$$= \quad 8.2 \tag{4.28}$$

improving the number of predicted events by a factor ~ 10 if down tracks are included. However the choice was made to use only long tracks due to the complex requirement of performing track extrapolations when using down tracks, with a factor 10 increase in statistics still meaning any result would not yet be competitive in precision. Within LHCb, decays in which the longitudinal component of momentum for the mother particle greatly exceeds the transverse are labelled as being 'soft' with $K^\pm \to \pi^\pm \mu^+ \mu^-$ falling within this category. At Run 1 optimisations had not yet been

made in triggering to efficiently capture these decays. As such the decision was made to use the $3\,\mathrm{fb}^{-1}$ of data collected between 2011–2012 as a means of preparing and testing the scripts and methods which would then ultimately be used on the Run 2 data when available. Where appropriate, reference to this former study and its results are made within the report of this investigation to support the choice of analysis workflow.

New trigger lines designed to complement searches for rare decays in strange physics were implemented in Run 2. Within HLT1 and HLT2 two lines, `Hlt1DiMuonNoL0` and `Hlt2DiMuonSoft` respectively, were added to introduce inclusive selection on dimuon candidates [83]. The selections widen scope to capture lower p_T and longer lifetime (when compared to the b and c hadrons typical to LHCb selection) events to account for these decays as shown in Figure 4.6.
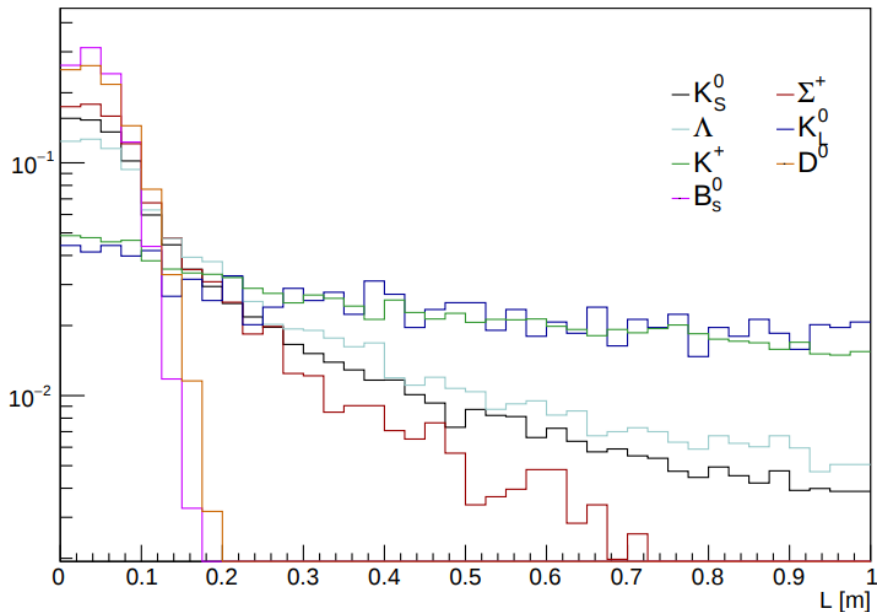
Figure 4.6: Distributions of the distances traversed by strange and heavy flavour hadrons within LHCb pp collisions [83].

At the time of writing configurations for creating Monte Carlo for 2017 data were still under development adding possible delay to the analysis. The choice was therefore made to request samples for the available configurations for 2015 and 2016 MC,

there being notable differences in kinematic variable and invariant mass distributions between these years, and then testing the assumption that there was no significant variation in the same distributions between 2016 and 2017. The test was carried out by making direct comparisons between key variables within both data sets via a method known as *sWeighting* which is discussed in subsection 4.2.1.

As a proxy for monitoring the effect on $K^{\pm} \to \pi^{\pm}\mu^{+}\mu^{-}$ of triggering, reconstruction and cuts within LHCb, the similar channel of $K^{\pm} \to \pi^{\pm}\pi^{+}\pi^{-}$ was processed in parallel, additionally providing a means of reducing systematic effects by acting as a normalisation channel. It has a branching ratio of [12]:

$$\mathcal{B}(K^{\pm} \to \pi^{\pm}\pi^{+}\pi^{-}) = (5.583 \pm 0.024) \times 10^{-2}, \tag{4.29}$$

and forms a candidate of background in many analyses including $K^{\pm} \to \pi^{\pm}\mu^{+}\mu^{-}$. In the case of this analysis the misidentification of pions as muons leads to a peaking background under the rare decay selection, this misID peak is further investigated in subsection 4.2.4. The $K^{\pm} \to \pi^{\pm}\pi^{+}\pi^{-}$ efficiencies and measured signal yields are utilised in the determination of a single event sensitivity for $K^{\pm} \to \pi^{\pm}\mu^{+}\mu^{-}$ from which an expected yield is derived, when combined with the measured background within the signal region a predicted signal significance is obtained which forms the figure of merit during optimisation of the blinded stage of the analysis. The components of this single event sensitivity taken from both Monte Carlo and data are addressed in subsection 4.2.2.

To minimise background a multivariate analysis technique known as a *boosted decision tree* has been employed with a set of discriminant variables chosen for their high level of background suppression with minimal loss of signal efficiency. Further cuts take advantage of the detector's advanced particle identification system by constraining the probability of misidentification to again reduce the level of combinatorial background.

The methodology and choice of figure of merit are also described within subsection 4.2.2.

The systematics of this study are outlined from subsection 4.2.10 onwards, along with the results from a set of pseudoexperiments performed to ensure the final PDF was capable of fitting the complete data set once unblinding had been approved. Finally results are presented and discussed in relation to Standard Model expectation.

4.2.1   Monte Carlo and Data Samples

The data for this analysis was obtained under three Stripping versions: 24, 28r1 and 29r2 for 2015, 2016 and 2017 data respectively. Stripping lines `KPiMuMuLine` and `KPiPiPiMassMeasLine` are used for selection of $K^{\pm} \to \pi^{\pm}\mu^{+}\mu^{-}$ and $K^{\pm} \to \pi^{\pm}\pi^{+}\pi^{-}$ candidates prior to offline analysis. These lines contain cuts listed in Table 4.2 to place constraints on the $K^{\pm}$ vertex fits and momentum of daughter particles. Due to the large volume of $K^{\pm} \to \pi^{\pm}\pi^{+}\pi^{-}$ decays oberved by LHCb some variables contain tighter thresholds within the `KPiPiPiMassMeasLine`. The variables for which these thresholds are applied are:

- $p(\pi)/p(\mu)$ - Momentum of pions/muons, a lower threshold is set due to the high momentum of kaon decays.

- Track $\chi^2/\mathrm{ndf}(\mu/\pi)$ - χ^2 from fits to tracks obtained from hits within the detector, a constraint is applied to ensure the tracks are good candidates for the decay structure.

- Track ProbGhost - Probability that a track is due to ghosting within the detector, this is kept low to reduce background.

- MinIPχ^2 - The minimum value from the χ^2 of the track impact parameter.

- M_{l_1,l_2} - The invariant mass of two of the daughter leptons.

- $M_{K^\pm}$ - Mass of the identified kaon mother constraining this again reduces background.

- $K^\pm$ DOCAMAX - The distance of closest approach for any pair of daughter tracks, keeping this low ensures a good level of compatibility between the tracks and the decay vertex.

- $K^\pm$ Vtxχ^2 - Vertex χ^2 obtained from fitting the kaon decay vertex.

- $K^\pm$ Vtxχ^2 Distance - χ^2 distance of the kaon from the primary vertex.

- $K^\pm$ IPχ^2 - impact parameter χ^2 with respect to the kaon primary vertex. An upper limit cuts out any candidates with poor compatibility after fitting.

Additional selections are made under DaVinci (see subsection 3.3.1) with the events being read as particles from the `Leptonic` data stream. Candidate events are required to have non-zero transverse momentum to ensure they pass outside of the beam-pipe volume, and a cut is applied on the $K^\pm$ mass to be within an interval of the average measurement as recorded within the PDG. The events are mainly captured by the HLT due to the low p_T the majority being TIS at the L0 level. At HLT1 and HLT2 dedicated trigger lines exist which are designed to select low mass dimuon decays and include a line specifically for $K^\pm \to \pi^\pm \mu^+ \mu^-$. Further information on triggering and the resultant efficiencies is given in subsection 4.2.6. For the normalisation channel a combination of TIS lines is used for all trigger levels.

Due to the high branching ratio of $K^\pm \to \pi^\pm \pi^+ \pi^-$, the decay regularly forms a background under selections for other LHCb analyses, as a result any alterations in selection towards optimising for these channels would have an effect on the $K^\pm \to$

Table 4.2: Selections applied within stripping to $K^\pm \to \pi^\pm \mu^+ \mu^-$ and $K^\pm \to \pi^\pm \pi^+ \pi^-$ data and MC.

KPiMuMuLine	KPiPiPiMassMeasLine
$p(\pi) > 1\,\text{GeV}$	$p(\pi) > 1\,\text{GeV}$
$p(\mu) > 3\,\text{GeV}$	-
Track $\chi^2/\text{ndf}(\mu/\pi) < 3$	Track $\chi^2/\text{ndf}(\pi) < 5$
Track ProbGhost$(\pi/\mu) < 0.3$	Track ProbGhost$(\pi) < 0.4$
MinIPχ^2PV$(\pi/\mu) > 9$	MinIPχ^2PV$(\pi) > 25$
$M_{\mu^+,\mu m} < 1.5\,\text{GeV}$	$M_{\pi^+,\pi^-} < 1.5\,\text{GeV}$
$M_{K^\pm} \in [394, 594]\,\text{MeV}$	$M_{K^\pm} \in [444, 544]\,\text{MeV}$
$K^\pm$ DOCAMAX $< 3\text{mm}$	$K^\pm$ DOCAMAX $< 2\text{mm}$
$p_T(K^\pm) > 100\,\text{MeV}$	$p_T(K^\pm) > 300\,\text{MeV}$
$K^\pm$ DIRA > 0.98	$K^\pm$ DIRA > 0.9998
$K^\pm$ Vtx $\chi^2 < 25$	$K^\pm$ Vtx $\chi^2 < 10$
$K^\pm$ Vtxχ^2 Distance > 36	$K^\pm$ Vtxχ^2 Distance > 100
$K^\pm$ IP$\chi^2 < 25$	$K^\pm$ IP$\chi^2 < 25$

$\pi^\pm \pi^+ \pi^-$ background. This then explains the apparent increase in background level and loss of exponential-like sidebands within the combinatorial component between 2015 and 2016 evident in the invariant mass distributions shown in Table 4.3. This difference in background motivated separate handling of each sample when creating classifiers to this combinatorial background from signal. To avoid any human bias from false optimisation due to a perceived signal, the signal region for $K^\pm \to \pi^\pm \mu^+ \mu^-$ was kept blinded for the duration of the workflow development.

A notable feature in the distribution of the invariant mass of $K^\pm \to \pi^\pm \mu^+ \mu^-$ is the peak at 440 MeV which is due to the misidentification of two pions in $K^\pm \to \pi^\pm \pi^+ \pi^-$ as two muons. In order to perform a fit on this distribution a fair range either side of the signal region must be included, any cuts greatly compromising the fit quality. Therefore due to its location the misID peak must be included in the construction of a probability distribution function (PDF), with a $K^\pm \to \pi^\pm \mu^+ \mu^-$ yield then obtained from the signal component. Details of the fitting procedure are given in subsection 4.2.7.

For simulated data an assumption was firstly made that the distributions of kinematic

$$K^{\pm} \to \pi^{\pm}\mu^{+}\mu^{-} \qquad\qquad K^{\pm} \to \pi^{\pm}\pi^{+}\pi^{-}$$

2015 Stripping24

2016 Stripping28r1

2017 Stripping29r2
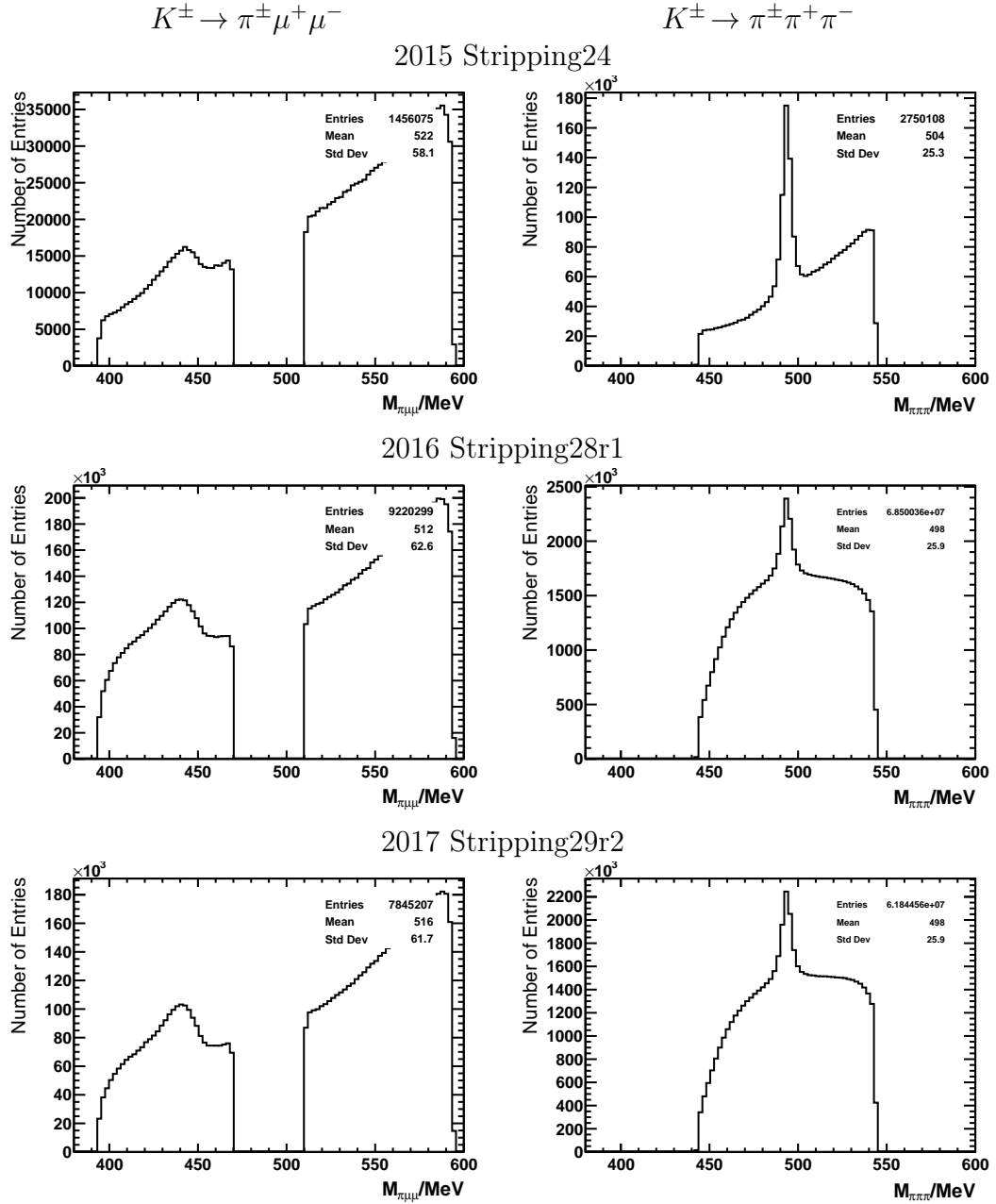
Table 4.3: Invariant mass distributions obtained after pre-selection from the chosen Stripping lines for $K^{\pm} \to \pi^{\pm}\mu^{+}\mu^{-}$ and $K^{\pm} \to \pi^{\pm}\pi^{+}\pi^{-}$ mass hypotheses between 2015–2017.

variables, such as the χ^2 of vertex fit of the $K^\pm$, are identical for 2016 and 2017 data, this was then tested. Requests were made for production of $K^\pm \to \pi^\pm \mu^+ \mu^-$ and $K^\pm \to \pi^\pm \pi^+ \pi^-$ MC for 2015 and 2016, ensuring statistics were generated for both magnetic field polarities (MagUp/MagDown). Once these samples were available, the assumption of compatibility between 2016 and 2017, along with the validity of the MC, was verified using the method of *sWeighting* on the 2017 data. This forms part of the $_s\mathcal{P}lot$ method which allows an estimation to be made for the distribution of an underlying component within a dataset by weighting the data [84].

The mechanism behind sWeighting is to determine probabilistically whether an event is more signal or background like using the information taken from a fit. Using $K^\pm \to \pi^\pm \pi^+ \pi^-$ for the verification of MC the yields obtained for the components of the PDF (the details of which can be found in subsection 4.2.7) after fitting to invariant mass are used to construct weights applied to different regions of the phase space. The $_s\mathcal{P}lot$ object is unable to know specifically whether an event is signal or background like. Instead the constructed weights act to remove from the data sample the fraction of events that are classed as background by the fit, changing the shape of the distribution to cut away as a fraction of the total data the background when these weights are applied. Shown in Figure 4.7 are examples for distributions of variables selected as candidates for a classifier, the comparison is made between 2016 and 2017 data, and 2016 MC. These examples consist of the End Vertex χ^2 ($\mathrm{EV}\chi^2$) obtained from fits to the kaon decay vertex, the transverse momentum (p_T), the flight distance downstream in the positive z direction through the detector (δz) of the $K^\pm$, and the cosine of the angle between the momentum vector of the $K^\pm$ and the vector obtained from the three daughters. As can be seen from the figure there is qualitative agreement between the MC and data.

In addition to sWeighting a second check was performed later in which the ratio of the number of events within the $K^\pm \to \pi^\pm \pi^+ \pi^-$ signal peak were compared to the
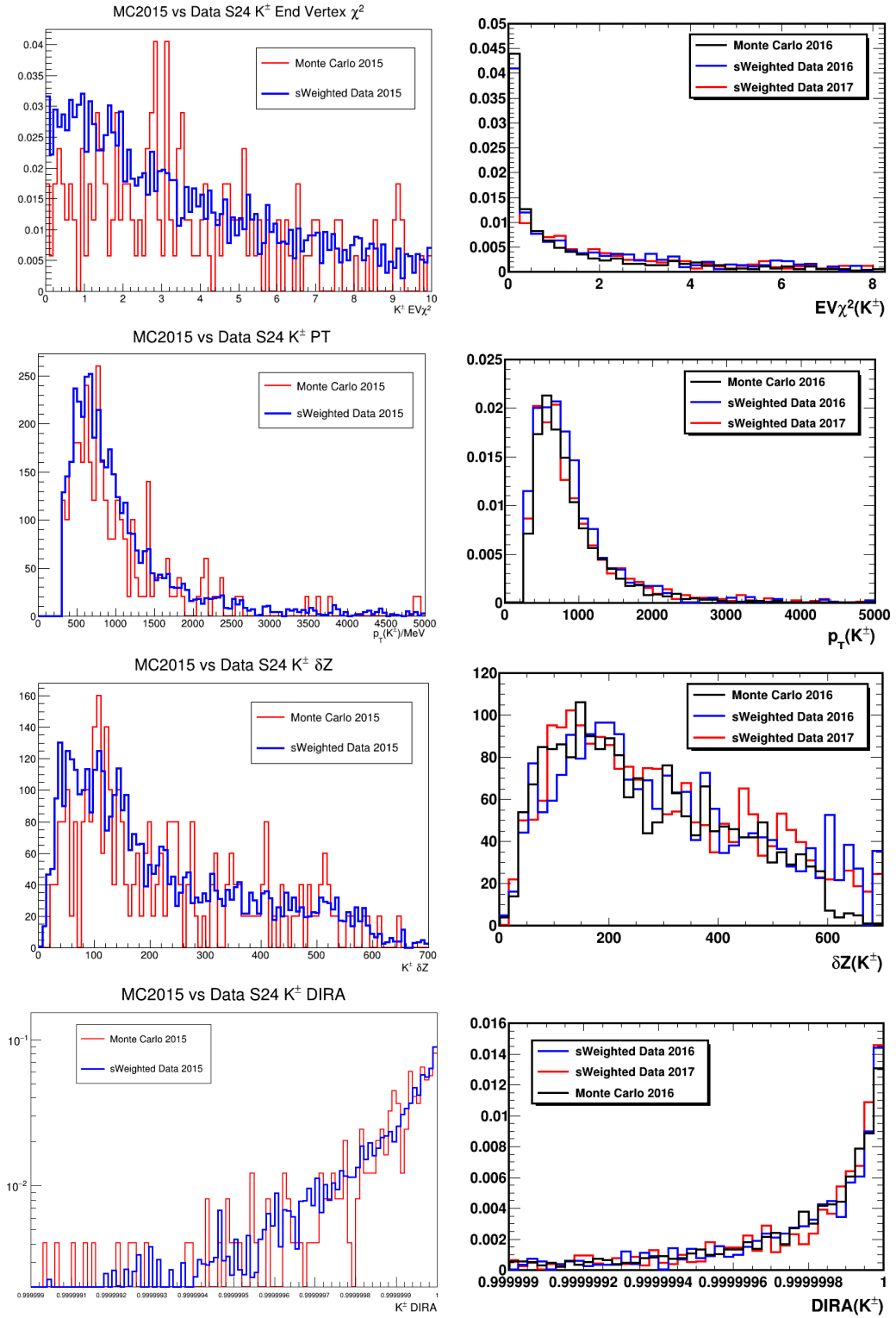
Figure 4.7: Comparison of MC with sWeighted data samples in various kinematic variables, the results show good agreement both validating the MC and supporting the assumption that no separate 2017 MC is required.

yield of the misID peak within data after all cuts as a check between the two stripping selections, outlined in subsection 4.2.8. The ratio obtained for 2016 data is used to form a prediction for the misID yield in 2017, the comparison is shown in Table 4.4. The compatibility between the prediction and observation gives evidence to there being the same kinematic behaviour as well as compatible efficiencies between the two years.

Table 4.4: Number of events from $K^\pm \to \pi^\pm\pi^+\pi^-$ decays misidentified as $K^\pm \to \pi^\pm\mu^+\mu^-$ for 2017 data predicted by scaling the signal yield using the ratio of $N_{\pi\pi\pi}/N_{misID}$ from 2016 data, compared to true measurement from the data itself, all selection and offline cuts are applied.

$N_{misID,2017}$	
N_{pred}	N_{data}
287 ± 23	335 ± 31

The MC requests include additional cuts defined within the relevant DecFiles which are applied at the generation stage. Implementation of these cuts ensures a large proportion of the events passed the trigger cuts, and that the decay vertex of the $K^\pm$ fell within the VELO volume. The cuts included the `DaughtersInLHCb` constraint, which only accepts events whereby the daughter particles fall within the detector acceptance, and additional cuts applied using the *GenCutTool* (included within the LoKi library), shown in Table 4.5. The combined effect of all these cuts on the yield of $K^\pm \to \pi^\pm\mu^+\mu^-$ MC within acceptance is illustrated in Figure 4.8.

Table 4.5: Cuts applied in addition to `DaughtersInLHCb` at generation level in the production of MC samples for 2015 and 2016. The symbols EV_i represent the coordinates of the decay vertices.

Cuts	
$K^\pm$	π/μ
$((EV_x)^2 + (EV_y)^2) < 1m^2$	$\theta \in [0.005, 0.400]$
$p_z > 0\text{MeV}$	$\eta \in [1.95, 5.05]$
$EV_z \in [-0.1, 2.27]m$	$p > 1.5\,\text{GeV}$
$p_T > 90\text{MeV}$	$p_T > 50\text{MeV}$

In order to maximise statistics after the pre-selection cuts applied by stripping, the samples were also *filtered*; an additional step to constrain candidates further.
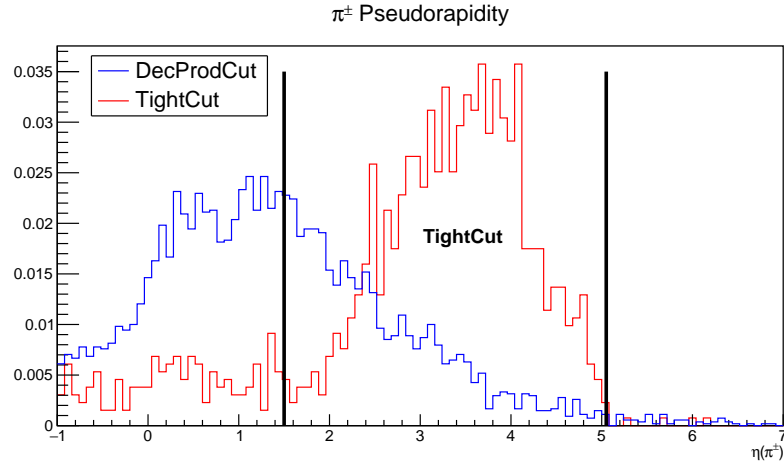
(a) Cut to the pseudorapidity, η.
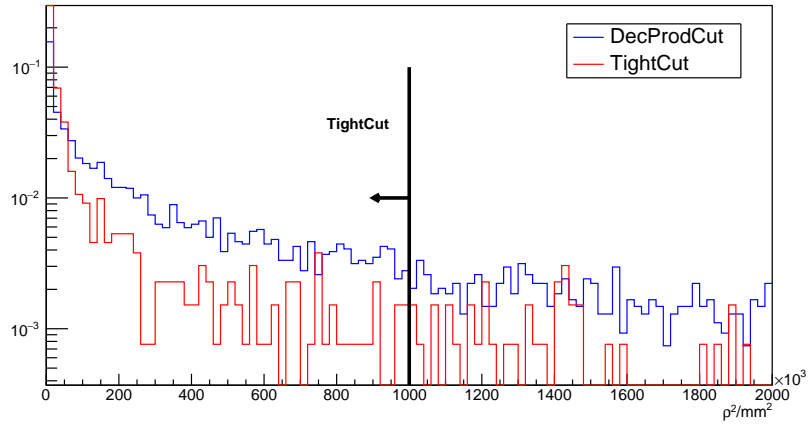
(b) Cut to the ρ end vertex parameter.
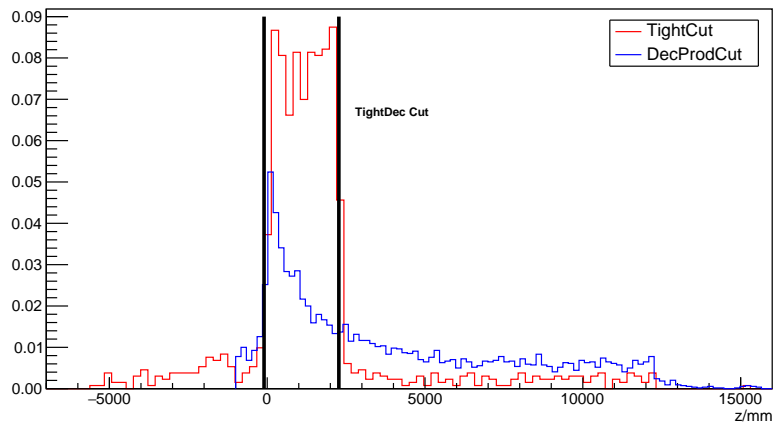
(c) Cut to the end vertex z position.

Figure 4.8: Comparison of two sets of generation cuts, the first, DecProd, constraining daughters to fallwithin LHCb and the second, TightCut, adding in addition the cuts within Table 4.5 defined using the GenCutTool, the black lines representing the thresholds defined within these cuts.

For both $K^\pm \to \pi^\pm \mu^+ \mu^-$ and $K^\pm \to \pi^\pm \pi^+ \pi^-$ the filtering consisted of MC truth matching whereby the daughters of the generated decay are compared to those configured at generation, and any reconstructed composite objects are confirmed to match the stated parent particle. What is left is a relatively background-free sample of the decay. The algorithms exploited for the matching are also contained within the LoKi framework, the selection is applied using the `mcMatch` functor on a relevant decay descriptor as shown in Table 4.6 and the particle objects used to reconstruct the decay are then read from container objects filled during the production.

Table 4.6: LoKi based MC truth matching requires a decay descriptor from which daughter and parent info is obtained. The string describes the channel to select on which includes the allowance of an arbitrary number of additional photons (ignoring intermediate resonance states) within the event represented by the use of '==>' syntax.

$K^\pm \to \pi^\pm \mu^+ \mu^-$	$K^\pm \to \pi^\pm \pi^+ \pi^-$
`mcMatch('[K+ ==> pi+ mu- mu+ ]CC')`	`mcMatch('[K+ ==> pi+ pi- pi+ ]CC')`

Due to the poor modelling of the ProbNN variables with LHCb MC (see section 3.4), to accurately deduce the efficiencies of any cuts to these variables which describe the probability of a particle being identified under a given particle ID, new distributions in these variables are generated from models in data using PIDGen. The process is performed on both rare and normalisation MC samples.

4.2.2   Single Event Sensitivity and Figure of Merit

The analysis is performed with the signal region of the invariant mass, $M_{\pi\mu\mu} \in [485, 505]$ MeV, blinded from visual interpretation by the analyst. To ensure an optimal choice of cut values and in order to determine a prediction of detector sensitivity in measurement of the rare decay whilst blinded, the single event sensitivity $\alpha_{\pi\mu\mu}$ defined as:

$$\alpha_{\pi\mu\mu} = \frac{1}{N_{\pi\pi\pi}} \frac{\epsilon^{\pi\pi\pi}}{\epsilon^{\pi\mu\mu}} \mathcal{B}(K^\pm \to \pi^\pm \pi^+ \pi^-) \tag{4.30}$$

is determined. Here $N_{\pi\pi\pi}$ is defined as the measured number of signal events for $K^{\pm} \to \pi^{\pm}\pi^{+}\pi^{-}$, and $\epsilon^{\pi\pi\pi}$ and $\epsilon^{\pi\mu\mu}$ are the efficiencies of $K^{\pm} \to \pi^{\pm}\pi^{+}\pi^{-}$ and $K^{\pm} \to \pi^{\pm}\mu^{+}\mu^{-}$ respectively. An estimate for the predicted number of rare decay events $N_{\pi\mu\mu}$ can be obtained using the current accepted branching ratio measurement as:

$$N_{\pi\mu\mu} \sim \frac{\mathcal{B}(K^{\pm} \to \pi^{\pm}\mu^{+}\mu^{-})}{\alpha_{\pi\mu\mu}}. \tag{4.31}$$

Fitting to the sidebands of the $K^{\pm} \to \pi^{\pm}\mu^{+}\mu^{-}$ background to determine the number of background events within the signal region, the figure of merit optimised throughout this analysis is the significance defined as:

$$Z = \frac{N_{\pi\mu\mu}}{\sqrt{N_{bkg}}}, \tag{4.32}$$

the aim being to balance a high signal yield with a good level of background suppression.

The efficiency for each channel can be broken down into components which are deduced either from MC or data:

$$\epsilon = \epsilon_{acc} \cdot \epsilon_{reco} \cdot \epsilon_{sel} \cdot \epsilon_{trig} \cdot \epsilon_{cut}. \tag{4.33}$$

Here ϵ_{acc} is the acceptance efficiency, the fraction of events which fall within the geometric acceptance of the LHCb detector with reference to the number generated by simulation. The reconstruction efficiency, ϵ_{reco} is the fraction of those events passing LHCb acceptance which are successfully reconstructed from tracks and vertices. Finally ϵ_{sel} is the selection efficiency on reconstructed candidates which includes both the selections performed by the analyst (see subsection 3.3.1), and the pre-selections performed within the Stripping process (described in section 3.3). All these efficiencies are determined from Monte Carlo. The efficiency of the LHCb

trigger system ϵ_{trig} is obtained using MC for the software trigger stages (HLT), and the data driven TISTOS method outlined in section 3.2.8 for the L0 hardware trigger. Finally, the efficiency of any additional cuts such as those applied via classifier trainings and constraints on the PID variables fall under ϵ_{cut}. The choices for these cuts will be addressed in the sections to follow.

4.2.3   Efficiencies from Monte Carlo

Within a MC production the simulated events are passed through the same stages in the data flow as real data. However unlike real data the information for the efficiency of these stages can be determined just for the channel being investigated.

For the generation level (or acceptance cuts) the efficiencies are summarised in Table 4.7 and are taken from the production tables produced by the MC liaisons. The low efficiency reflects the long lifetime of the $K^\pm$ leading to most particles decaying downstream of the detector.

The efficiencies relating to the filtering process are given in Table 4.8 and show the fraction of events identified via truth matching as real $K^\pm \to \pi^\pm \mu^+ \mu^-$ and $K^\pm \to \pi^\pm \pi^+ \pi^-$ decay candidates.

Table 4.7: Acceptance efficiencies for 2015 and 2016 MC in $K^\pm \to \pi^\pm \mu^+ \mu^-$ and $K^\pm \to \pi^\pm \pi^+ \pi^-$.

	$K^\pm \to \pi^\pm \mu^+ \mu^-$	$K^\pm \to \pi^\pm \pi^+ \pi^-$
$\epsilon_{gen,2015}$	$(1.5048 \pm 0.0036) \times 10^{-3}$	$(1.9337 \pm 0.0045) \times 10^{-3}$
$\epsilon_{gen,2016}$	$(1.5070 \pm 0.0040) \times 10^{-3}$	$(1.9333 \pm 0.0049) \times 10^{-3}$

Table 4.8: Filtering efficiencies for 2015 and 2016 MC in $K^\pm \to \pi^\pm \mu^+ \mu^-$ and $K^\pm \to \pi^\pm \pi^+ \pi^-$.

	$K^\pm \to \pi^\pm \mu^+ \mu^-$	$K^\pm \to \pi^\pm \pi^+ \pi^-$
$\epsilon_{filt,2015}$	$(5.41 \pm 0.02) \times 10^{-2}$	$(3.70 \pm 0.01) \times 10^{-2}$
$\epsilon_{filt,2016}$	$(5.65 \pm 0.02) \times 10^{-2}$	$(3.87 \pm 0.01) \times 10^{-2}$

4.2.4   Candidate Backgrounds

The most dominant background contribution comes from the double misidentification of pions as muons from $K^\pm \to \pi^\pm\pi^+\pi^-$ and is evident in all data samples as a peak within the invariant mass distribution. The reconstructed invariant mass distribution for this misid has a maximum at $\sim$440 MeV with a small leakage into the signal region.

In addition to $K^\pm \to \pi^\pm\pi^+\pi^-$ other kaon decay channels were investigated under the $K^\pm \to \pi^\pm\mu^+\mu^-$ selection as potential sources of peaking backgrounds. The study was performed during the pre-Run 2 analysis of Run 1 data by requesting samples of MC for the channels given in Table 4.9. These channels were previously identified as potential backgrounds in an analysis carried out within the NA48/2 collaboration also into $K^\pm \to \pi^\pm\mu^+\mu^-$ [85].

Table 4.9: Additional Kaon modes investigated as potential background using Run 1 MC.

	Requested Events	Branching Ratio
$K^\pm \to \pi^+\pi^-\mu^\pm\nu_\mu$	2×10^6	$(1.4 \pm 0.9) \times 10^{-5}$
$K^\pm \to \pi^+\pi^-e^\pm\nu_e$	2×10^6	$(4.25 \pm 0.02) \times 10^{-5}$
$K^\pm \to \mu^+\mu^-\mu^\pm\nu_\mu$	2×10^5	$< 4.1 \times 10^{-7}$
$K^\pm \to \mu^+\mu^-e^\pm\nu_e$	2×10^5	$(1.7 \pm 0.5) \times 10^{-8}$

The selection was applied to 2011 and 2012 MC, the resultant invariant mass distributions are shown in Figure 4.9. These show no peaking component but rather an exponential or near-uniform distribution. Using the measured number of $K^\pm \to \pi^\pm\pi^+\pi^-$ obtained from the data fits for Run 2, the yields for each of these channels were predicted:

$$N_{K^\pm \to X} \sim N_{\pi\pi\pi} \frac{\epsilon^{K^\pm X}}{\epsilon^{\pi\pi\pi}} \frac{\mathcal{B}(K^\pm \to X)}{\mathcal{B}(K^\pm \to \pi^\pm\pi^+\pi^-)} \tag{4.34}$$

and are given in Table 4.10. From the results it was concluded that if such channels

are subject to misidentification by LHCb, they would still not form part of the $K^\pm \to$ $\pi^\pm \mu^+ \mu^-$ combinatorial background component. When later compared with final background yields (see subsection 4.2.9) which are ~ 100 events, the misID fraction due to these channels would be at the highest $\sim 10^{-3}$ given the yield predictions for these candidates.

Table 4.10: Predicted yields for candidate background $K^\pm$ channels in 2015–2017. The uncertainties come from the uncertainties in the efficiencies and the branching ratios for each.

	2015	2016	2017
$K^\pm \to \mu^+\mu^-\mu^\pm\nu_\mu$	$(7.6 \pm 2.3) \times 10^{-4}$	$(9.2 \pm 2.8) \times 10^{-3}$	$(9.8 \pm 3.0) \times 10^{-3}$
$K^\pm \to \mu^+\mu^-e^\pm\nu_e$	$(1.2 \pm 0.6) \times 10^{-5}$	$(1.4 \pm 0.7) \times 10^{-4}$	$(1.5 \pm 0.8) \times 10^{-4}$
$K^\pm \to e^\pm\pi^+\pi^-\nu_e$	$(1.03 \pm 0.29) \times 10^{-2}$	$(1.24 \pm 0.34) \times 10^{-1}$	$(1.3 \pm 0.4) \times 10^{-1}$
$K^\pm \to \mu^\pm\pi^+\pi^-\nu_\mu$	$(4.4 \pm 3.1) \times 10^{-3}$	$(5 \pm 4) \times 10^{-2}$	$(6 \pm 4) \times 10^{-2}$

(a) $K^\pm \to \pi^+\pi^-\mu^\pm\nu_\mu$

(b) $K^\pm \to \pi^+\pi^-e^\pm\nu_e$

(c) $K^\pm \to \mu^+\mu^-\mu^\pm\nu_\mu$

(d) $K^\pm \to \mu^+\mu^-e^\pm\nu_e$
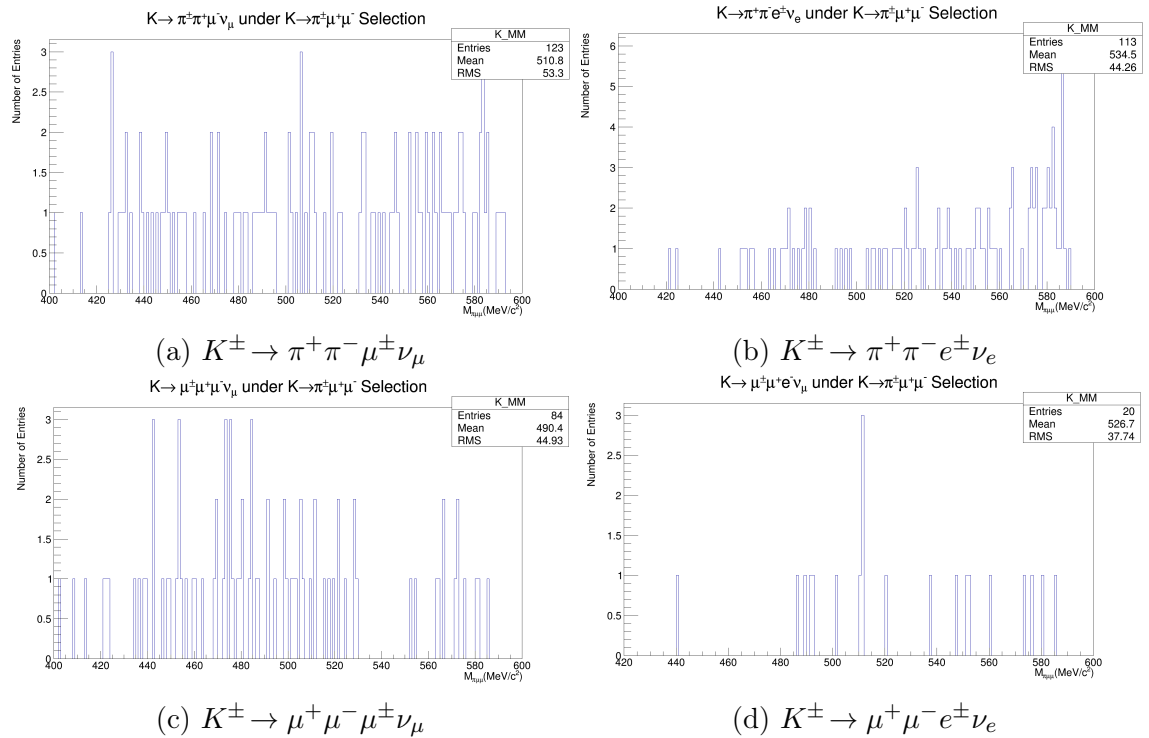
Figure 4.9: Resultant distributions in reconstructed invariant mass $M_{\pi\mu\mu}$ when applying $K^\pm \to \pi^\pm\mu^+\mu^-$ selection on the MC for the channels in Table 4.9.

For more general searches of prospective background channels the selection for $K^\pm \to \pi^\pm\mu^+\mu^-$ was also applied to samples of minimum bias (40 million events) and b-inclusive MC (4 million events), the latter consisting of decays of b-hadrons

only; as LHCb is optimised for observation of such decays it was important to verify that any contribution is also purely combinatorial. As none of the events for minimum bias passed the selection for the available level of statistics, results are instead shown for $K^{\pm} \to \pi^{\pm}\pi^{+}\pi^{-}$ in Figure 4.10. The invariant mass distributions are compatible with the exponential-like upper sideband for $K^{\pm} \to \pi^{\pm}\mu^{+}\mu^{-}$, and so the status of any contribution from such channels within data background was concluded to be combinatorial.
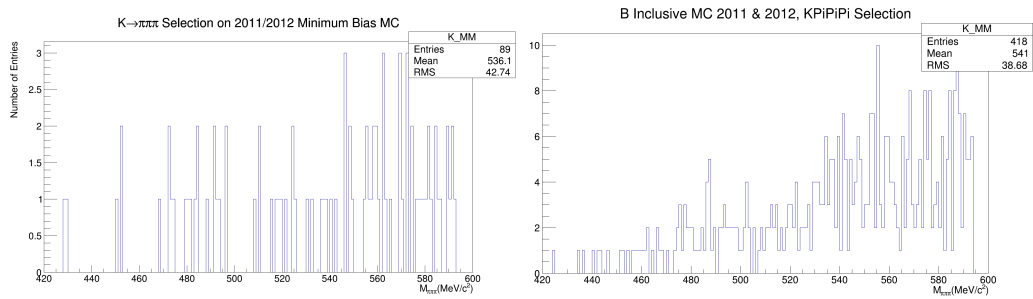
Figure 4.10: $K^{\pm} \to \pi^{\pm}\mu^{+}\mu^{-}$ selection applied to 2011 and 2012 minimum bias (Left) and b-inclusive (Right) MC.

Further investigations were performed using the DaVinci tool *TupleToolMCBackgroundInfo* on samples of Run 1 MC the details for which can be found in section A.4. After cuts are applied from a trained classifier a large proportion of the background events are suppressed, those surviving these cuts are dominantly 'ghost' events, these contain at least one particle which has been mistaken to be part of the event but is actually due to effects within the detector material, and are reduced further by the cuts to `ProbNNghost` variables within this analysis.

4.2.5   Suppression of Background

To suppress the combinatorial background for both $K^{\pm} \to \pi^{\pm}\mu^{+}\mu^{-}$ and $K^{\pm} \to \pi^{\pm}\pi^{+}\pi^{-}$ a series of cuts are applied offline. Firstly a cut is applied to remove the component of background due to clone events where a daughter particle is selected

twice, once as its own sister (sisters sharing the same origin vertex). The cut places a constraint on the angular separation between each pair of the three daughters ensuring the tracks are distinguishable. In order to determine an optimal cut value for this variable which yielded the best signal significance with high signal efficiency, $K^{\pm} \to \pi^{\pm}\pi^{+}\pi^{-}$ data and MC were monitored for various cut values as shown in Figure 4.11. Applying this cut to the two samples of available MC the
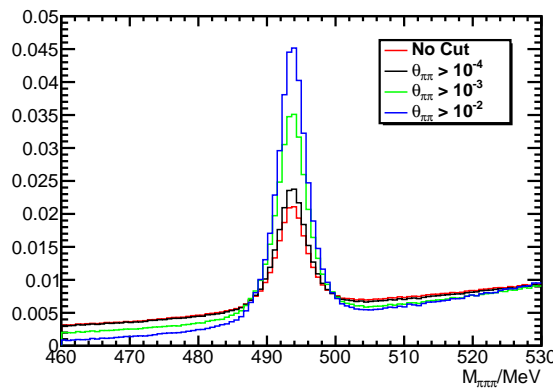
Figure 4.11: Invariant mass distribution for $K^{\pm} \to \pi^{\pm}\pi^{+}\pi^{-}$ 2015 S24 Data showing the sensitivity of the signal/background distribution with respect to cutting on the θ_{ij} (in this case for two pions) variable.

Table 4.11: Efficiency of θ_{ij} cuts on 2015 S24 Data and Monte Carlo.

$\theta_{ij} > x$	$\epsilon_{cut,data}$	$\frac{N_S}{\sqrt{N_S+N_B}}$	$\epsilon_{cut,MC}$
10^{-2}	0.649 ± 0.011	115 ± 1	0.741 ± 0.003
10^{-3}	0.954 ± 0.015	130 ± 1	0.991 ± 0.001
10^{-4}	0.964 ± 0.016	113 ± 1	0.998 ± 0.001

efficiencies defined in Table 4.12 are measured. For this analysis a cut value of $\theta_{ij} > 10^{-3}$ was chosen based on both the high efficiency of $\sim 95\%$ and the higher signal significance when compared to tighter and looser cuts.

Table 4.12: Efficiency of angle cut θ_{ij} when applied to 2015 and 2016 signal MC.

	$K^{\pm} \to \pi^{\pm}\mu^{+}\mu^{-}$	$K^{\pm} \to \pi^{\pm}\pi^{+}\pi^{-}$
$\epsilon_{cut,2015}$	0.991 ± 0.001	0.988 ± 0.001
$\epsilon_{cut,2016}$	0.989 ± 0.005	0.978 ± 0.005

Secondly cuts are applied to suppress the effect of 'ghosting' within the detector

where a track is falsely measured where none occurred. Within LHCb neural networks are trained using pattern recognition algorithms which utilise information such as the number of hits within the VELO and χ^2 measures of track fit variables [86] to deduce the probability that the event is due to ghosting.

Using signal significance as a figure of merit an optimal cut of `ProbNNghost < 0.4` has been chosen using the maximum of a scan performed by cutting on this variable across all three daughters, these scans are shown in Figure 4.12 and the efficiencies of these cuts on MC are given in Table 4.13.

(a) Scan for $\pi^{\pm}$.

(b) Scan for π^{+}.

(c) Scan for π^{-}.
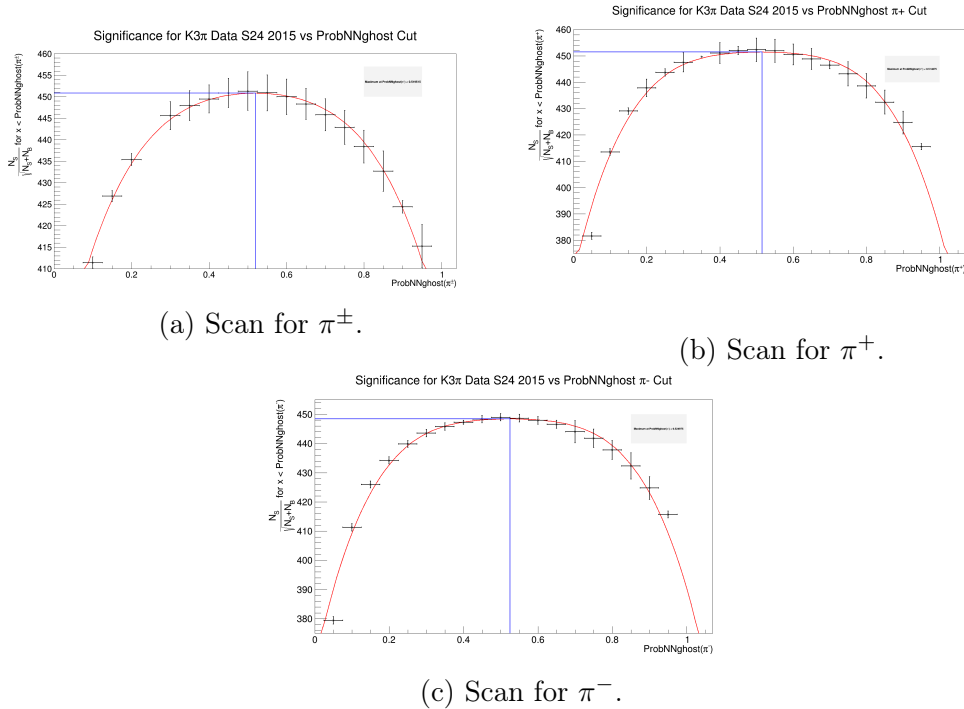
Figure 4.12: Scans in signal significance across `ProbNNghost` variables in 2015 $K^{\pm} \rightarrow \pi^{\pm}\pi^{+}\pi^{-}$ data.

Table 4.13: Efficiencies for the `ProbNNghost < 0.4` cut on π/μ in each Monte Carlo sample. The differences between 2015 and 2016 MC are due to the change in trigger selections showing improvement between the years. Uncertainties come from the MC statistics.

	$K^{\pm} \rightarrow \pi^{\pm}\mu^{+}\mu^{-}$	$K^{\pm} \rightarrow \pi^{\pm}\pi^{+}\pi^{-}$
$\epsilon_{Ghost,2015}$	0.783 ± 0.003	0.784 ± 0.003
$\epsilon_{Ghost,2016}$	0.919 ± 0.002	0.858 ± 0.002
$\epsilon_{Ghost,2017}$	0.919 ± 0.002	0.859 ± 0.002

Optimisation in 2D Phase Space of Classifier and PID Cuts

A PID cut is applied to the pion common to both channels and is held constant, the value for this cut is determined through a scan on the signal significance of $K^{\pm} \to \pi^{\pm}\pi^{+}\pi^{-}$. An optimisation is then performed in a 2D phase space across cuts using a BDT (multivariate) classifier, and the PID variables on the remaining two daughter particles ProbNNpi/mu which are the probability of a particle being a pion or muon respectively, both of these particles share the same cut. The scan is performed by taking measurements across the phase space using 40% of the data and MC as a sub-sample to keep training times low with a good level of statistics to combat overtraining. The values required for a measurement of the single event sensitivity in Equation 4.30 are extracted from fits and MC efficiencies. The chosen figure of merit is the predicted signal significance $N_{\pi\mu\mu}/\sqrt{N_{bkg}}$ obtained from the fit model yields within the signal region after fitting to the upper sideband for $K^{\pm} \to \pi^{\pm}\mu^{+}\mu^{-}$, and calculating a signal yield using the existing NA48/2 measurement:

$$N_{\pi\mu\mu} = \frac{\mathcal{B}(K^{\pm} \to \pi^{\pm}\mu^{+}\mu^{-})}{\alpha_{\pi\mu\mu}}, \qquad (4.35)$$

the signal region of $[485, 505]\,\mathrm{MeV}$ is held blinded.

Classifiers are coded using the Toolkit for Multivariate Analysis (TMVA) under the ROOT data analysis framework, a Fortran based library which has been migrated to C++. Rare and normalisation channels are each treated separately using simulated data and the upper sideband of real data, in the region $M_{\pi XX} > 510\,\mathrm{MeV}$, as samples of signal and background respectively. It is assumed that upper mass sideband is representative of data under the signal peak and that any kinematic biases are small. The chosen classifier type for this analysis is called a Boosted Decision Tree (BDT) and involves construction of a tree-like chain of Boolean decisions consisting of cuts to a single input variable at each node as shown in Figure 4.13. This training

eventually leads to the phase space split into signal and background [87]. The process of applying cuts on a variable during decision tree construction is repeated until a stop criterion is met. For this analysis as a compromise between performance and overtraining due to limited statistics, the training options were to set to maximise tree depth to two, and a maximum of 2000 candidate trees being allowed in total. During the training procedure the samples are split, based on the number of events, randomly between being either used for the training itself or for testing of the classifier after completion. Eventually the trees are combined and an average taken which forms the overall classifier.
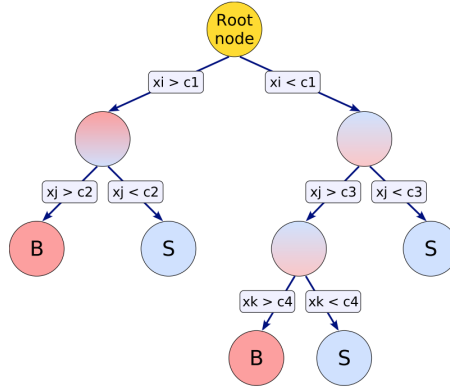
Figure 4.13: A decision tree created from a set of variables x, this tree has a depth of 3. The variable at each node is that which gives the best degree of separation [87, Fig. 18].

The BDT is configurable within TMVA with options being chosen which balance both run time and the separation power of the classifier. The Adaptive Boost (AdaBoost) method is used to enhance the training, the action of *boosting* in this context being that an accurate prediction for the type of a given subset of data can be made based on using a combination of weaker and more inaccurate rules [88], this is useful in accounting for statistical fluctuations in the data. The variables selected for the training mainly consist of χ^2 values from kinematic fits and are:

- $\log\left(p_T\left(K^{\pm}\right)\right)$ - the transverse momentum of the $K^{\pm}$.

- $\text{IP}\chi^2(K^{\pm})$ - the impact parameter χ^2.

- δz of $K^{\pm}$ - the distance between the production and decay vertices of the $K^{\pm}$ in the downstream (positive z direction).

- $\log\left(\min(\text{IP}\chi^2(\pi/\mu))\right)$ - the minimum of daughter impact parameter χ^2 values relative to the kaon decay vertex (all pions for $K^{\pm} \to \pi^{\pm}\pi^{+}\pi^{-}$ and muons for $K^{\pm} \to \pi^{\pm}\mu^{+}\mu^{-}$.

- $\log\left(1 - \text{DIRA}\left(K^{\pm}\right)\right)$ - DIRA being the cosine of the angle between the $K^{\pm}$ momentum and the vector sum of the momenta of all daughters.

- $\log(\text{EV}\chi^2\left(K^{\pm}\right))$ - the decay vertex χ^2 of the $K^{\pm}$ from fits to the three daughter tracks.

The variables are illustrated in Figure 4.14, and the distributions are shown below in Figure 4.15. New trainings are performed for each year between 2015 and 2017

(a) The DIRA angle.   (b) The end vertex χ^2.

(c) δz.
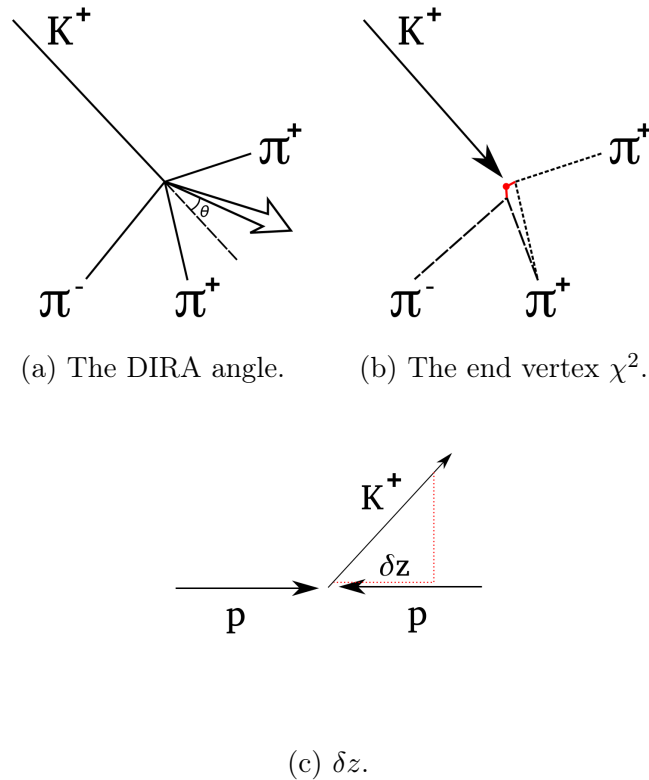
Figure 4.14: Illustrations showing the variables used during the training of the BDT.

using the available MC, in the case of 2017 re-stripped 2016 MC into Stripping29r2

has been utilised. After application of the BDT to the data, an optimal cut with respect to signal significance is found for $K^{\pm} \to \pi^{\pm}\pi^{+}\pi^{-}$ and kept constant for the duration of the overall 2D optimisation process. Although using the same cut for both channels would reduce systematic effects, due to the low predicted signal yield the primary concern was to keep a high level of statistics.
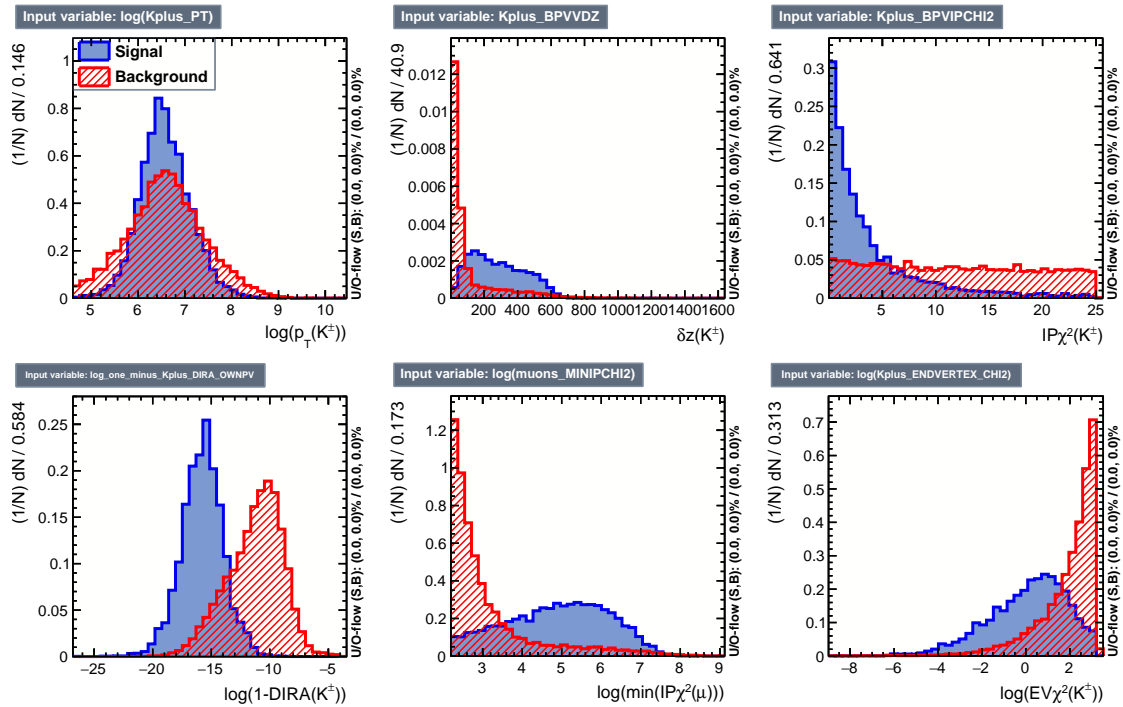
Figure 4.15: Example of distributions of input variables for one of the permutations for $K^{\pm} \to \pi^{\pm}\mu^{+}\mu^{-}$ 2016 Stripping28 data and MC. A permutation in this context is a set of three of the 5 sub-datasets which are used for the training, testing and application. Combinations are cyclic.

To avoid any potential bias in the samples, the data and Monte Carlo are split into five equivalently sized parts, with each cyclic permutation of three forming the sub-samples for training, testing and application respectively in a process known as k-folding [89]. Within the 2D optimisation a BDT cut range of [-0.1, 0.05] is trialled for $K^{\pm} \to \pi^{\pm}\mu^{+}\mu^{-}$ based on the statistics available within this region, the distribution for the 2016 BDT is shown in Figure 4.16. The *Receiver Operator Characteristic* (ROC) curves [90] for the six groups of trainings are shown in Figure 4.17 and Figure 4.18, the 5 k-folds of a given year and channel are comparable as expected.
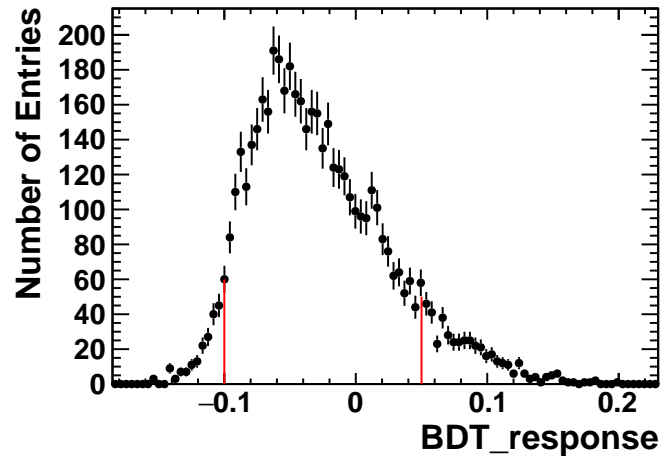
Figure 4.16: Distribution of BDT response variable for the 2016 Stripping28 $K^\pm \to \pi^\pm \mu^+ \mu^-$ data.
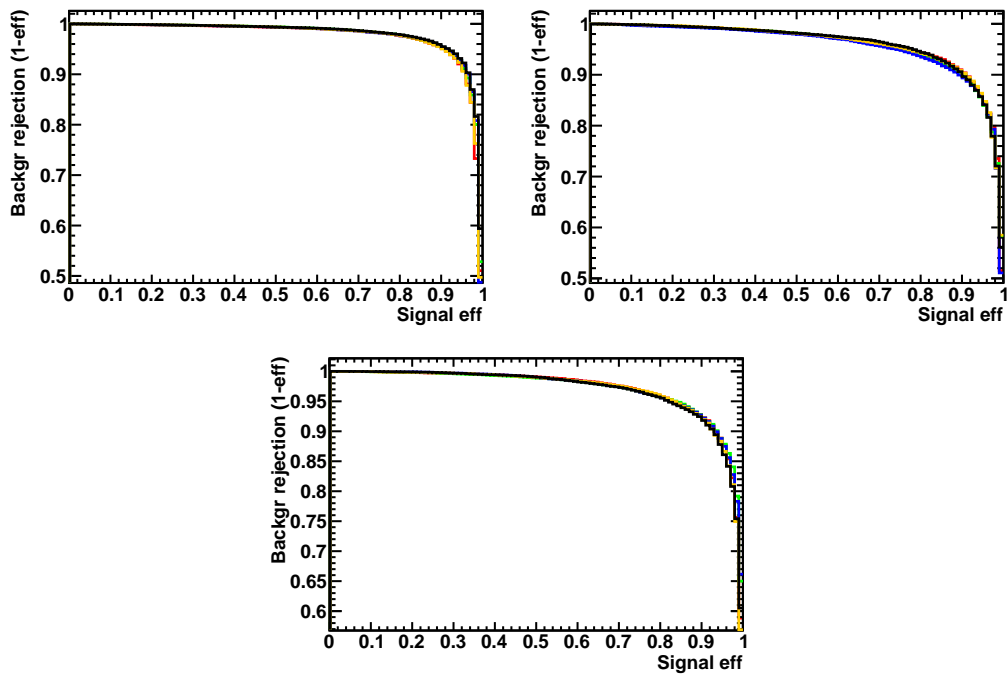
Figure 4.17: Performance of BDTs for $K^\pm \to \pi^\pm \mu^+ \mu^-$ showing separately the performance of each permutation: 2015 (Top Left), 2016 (Top Right) and 2017 (Bottom).
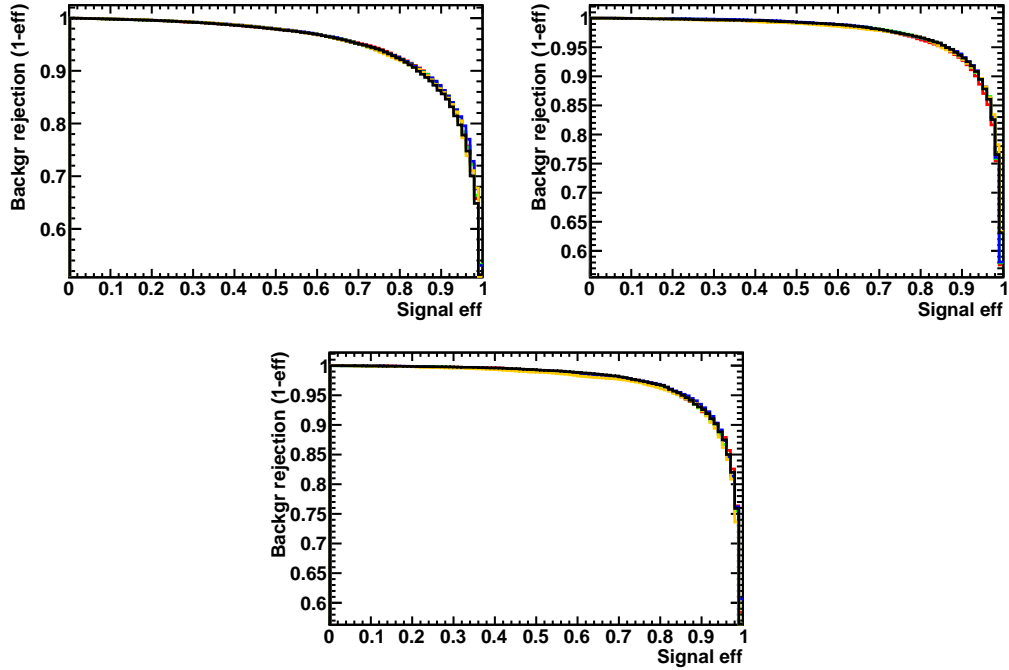
Figure 4.18: Performance of BDTs for $K^{\pm} \rightarrow \pi^{\pm}\pi^{+}\pi^{-}$ showing separately the performance of each permutation: 2015 (Top Left), 2016 (Top Right) and 2017 (Bottom).

For each year a 2D scan was performed in bins of ProbNN and BDT cut values with intervals of 0.01 and 0.05 respectively. The figure of merit used was the estimated significance calculated using the predicted number of signal events using the PDG average for the $K^{\pm} \rightarrow \pi^{\pm}\mu^{+}\mu^{-}$ branching fraction obtained from the final Single Event Sensitivity (SES) value (see Equation 4.35), and the background yield for real data within the signal region. The scans for 2015–2017 are shown in Figure 4.19, from these results the cut values given in Table 4.14 were chosen for the analysis. Although not optimal based on the chosen figure of merit, these cuts represent an acceptable compromise in selection performance that allow a single set of cuts to be used for all years. The efficiencies on MC from the 2D cuts are given in Table 4.15.

(a) 2015 Stripping24.

(b) 2016 Stripping28r1.

(c) 2017 Stripping29r2.

(d) 2018 Stripping34.
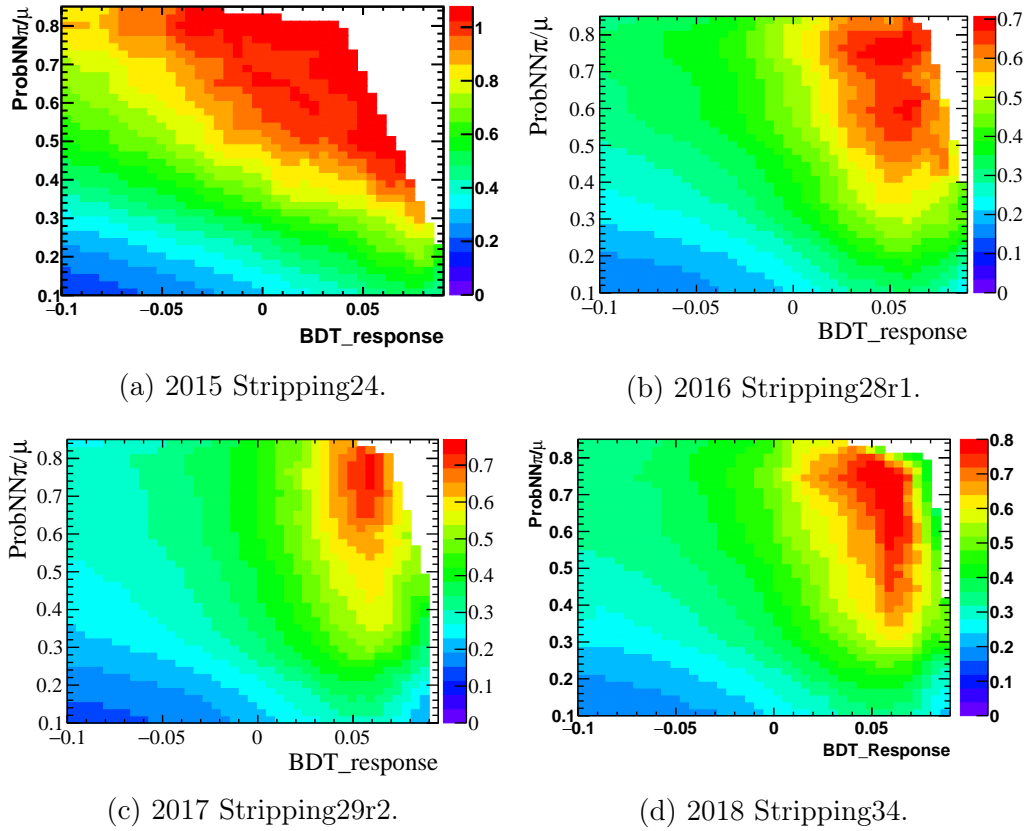
Figure 4.19: 2D offline cut scans of the predicted signal significance across PID variables and BDT response for Run 2 data.

Table 4.14: Cuts chosen for PID of the two π/μ daughters, BDT and ProbNNghost variables in $K^{\pm} \to \pi^{\pm}\mu^{+}\mu^{-}$ and $K^{\pm} \to \pi^{\pm}\pi^{+}\pi^{-}$.

	$\pi^{\pm}$	π/μ
ProbNNghost $<$ x	0.4	0.4
ProbNNπ/μ $>$ x	0.35	0.4
	$K^{\pm} \to \pi^{\pm}\mu^{+}\mu^{-}$	$K^{\pm} \to \pi^{\pm}\pi^{+}\pi^{-}$
BDT_response $>$ x	0.05	0.05

Table 4.15: Efficiencies for the `ProbNN`π/μ `> 0.4`, `ProbNN`$\pi^{\pm}$ `> 0.35`, and `BDT_response > 0.05`, `BDT_response > 0.05` for $K^{\pm} \to \pi^{\pm}\mu^{+}\mu^{-}$ and $K^{\pm} \to \pi^{\pm}\pi^{+}\pi^{-}$ respectively, cuts on each Monte Carlo sample.

	$K^{\pm} \to \pi^{\pm}\mu^{+}\mu^{-}$	$K^{\pm} \to \pi^{\pm}\pi^{+}\pi^{-}$
$\epsilon_{BDT.PID,2015}$	0.471 ± 0.003	0.455 ± 0.004
$\epsilon_{BDT.PID,2016}$	0.289 ± 0.003	0.647 ± 0.003
$\epsilon_{BDT.PID,2017}$	0.292 ± 0.003	0.643 ± 0.003
$\epsilon_{BDT.PID,2018}$	0.300 ± 0.003	0.651 ± 0.003

Application of $K^\pm \to \pi^\pm \mu^+ \mu^-$ BDT to $K^\pm \to \pi^\pm \pi^+ \pi^-$

The classifier for $K^\pm \to \pi^\pm \mu^+ \mu^-$ has also been applied to $K^\pm \to \pi^\pm \pi^+ \pi^-$ to determine the effect on a $K^\pm$ signal. The efficiencies and significances for both channels are compared in Table 4.16 and Table 4.17 showing the effect of the same BDT cut on each with a higher efficiency and high signal significance.

Table 4.16: Efficiencies of the BDTs for $K^\pm \to \pi^\pm \mu^+ \mu^-$ applied to $K^\pm \to \pi^\pm \pi^+ \pi^-$ and $K^\pm \to \pi^\pm \mu^+ \mu^-$ data with the `BDT_response > 0.05` cut.

	$K^\pm \to \pi^\pm \mu^+ \mu^-$	$K^\pm \to \pi^\pm \pi^+ \pi^-$
$\epsilon_{BDT,2015}$	0.767 ± 0.003	0.841 ± 0.003
$\epsilon_{BDT,2016}$	0.591 ± 0.003	0.642 ± 0.003
$\epsilon_{BDT,2017}$	0.594 ± 0.003	0.639 ± 0.003

Table 4.17: Significance of the $K^\pm \to \pi^\pm \pi^+ \pi^-$ signal in data with the application of the $K^\pm \to \pi^\pm \mu^+ \mu^-$ BDT at the cut of `BDT_response > 0.05`.

	$\frac{N_s}{\sqrt{N_s + N_B}}$
BDT, 2015	135 ± 1.1
BDT, 2016	665.3 ± 1.2
BDT, 2017	685.8 ± 1.2

4.2.6   Trigger Efficiencies

Before measuring trigger efficiency the effects of the Global Event Cuts (GECs) need to be taken into account. As the efficiency is correlated to the distribution of background, a different background between $K^\pm \to \pi^\pm \mu^+ \mu^-$ and $K^\pm \to \pi^\pm \pi^+ \pi^-$ would result in different efficiencies. Using the MC samples for $K^\pm \to \pi^\pm \mu^+ \mu^-$ and $K^\pm \to \pi^\pm \pi^+ \pi^-$ the signal distributions for the number of SPD hits were compared to deduce if a new efficiency ratio term for ϵ_{GEC} in the single event sensitivity measurement would be required. Comparing the distributions for both channels within Figure 4.20 there is an obvious difference in the location of the maxima near

to 100, however at the cut value of 450 the distributions are similar, meaning the efficiencies are comparable and have been assumed to give a ratio of one.

To account for any possible difference, MC has been scaled to agree with data in the region below the cut and a systematic contribution assigned based on the change in efficiency for the dominant `nSPDHits < 450` cut this causes. More information and the consequential systematic is outlined in section 4.2.10. The efficiencies are given in Table 4.18.

Table 4.18: The efficiencies related to the GEC cuts on $K^\pm \to \pi^\pm \mu^+ \mu^-$ and $K^\pm \to \pi^\pm \pi^+ \pi^-$ MC obtained after scaling to sWeighted data.

	$K^\pm \to \pi^\pm \mu^+ \mu^-$	$K^\pm \to \pi^\pm \pi^+ \pi^-$
$\epsilon_{GEC,2015}$	0.015 ± 0.001	0.016 ± 0.001
$\epsilon_{GEC,2016}$	0.013 ± 0.001	0.014 ± 0.001
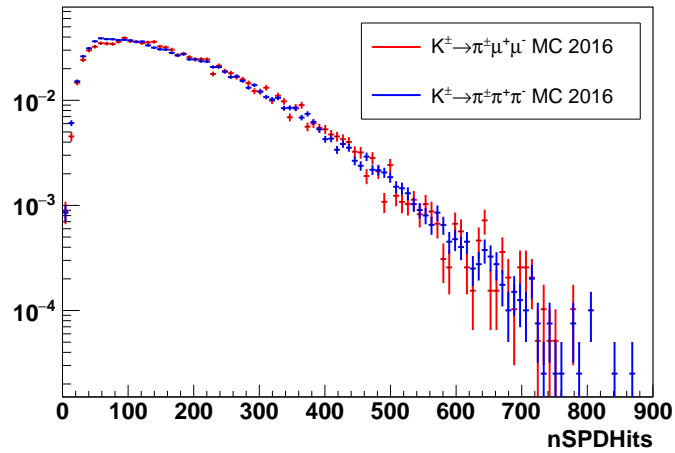
Figure 4.20: Comparison of distributions for the number of SPD hits in 2016 MC.

At the hardware level the three relevant L0 lines of `L0Hadron`, `L0Muon` and `L0DiMuon` have been chosen as they contain cuts optimised for the selection of hadronic decays containing muons, the thresholds for these lines are outlined in Table 4.20. Note due to technical difficulties during the injection of the LHC in 2017 leading to to lower collision rates, the thresholds for this year are much looser when compared to those of 2016 [40]. For calculation of the L0 trigger efficiency the TISTOS method as described in section 3.2.8 is used to estimate the efficiency for the L0 hardware

trigger in $K^\pm \to \pi^\pm \mu^+ \mu^-$ and $K^\pm \to \pi^\pm \pi^+ \pi^-$ [1]. For the purpose of the normalisation we cannot use TOS events for $K^\pm \to \pi^\pm \pi^+ \pi^-$ as they differ significantly (being 'on-signal') when compared to those for $K^\pm \to \pi^\pm \mu^+ \mu^-$. Instead we use both event types for $K^\pm \to \pi^\pm \mu^+ \mu^-$ and TIS only for $K^\pm \to \pi^\pm \pi^+ \pi^-$ at L0. For $K^\pm \to \pi^\pm \mu^+ \mu^-$, as the data are blinded during optimisation, the misID peak is fitted in bins of pseudorapidity $\eta(K^\pm)$ and the number of long tracks $nLongTracks$, the yields from these fits are used to determine an L0 TISTOS efficiency for $K^\pm \to \pi^\pm \mu^+ \mu^-$, an example fit is given in Figure 4.21. The fitting procedure itself is outlined in subsection 4.2.7. In the case of $K^\pm \to \pi^\pm \pi^+ \pi^-$ signal data is fitted. The efficiencies for both channels are summarised in Table 4.19, the uncertainties on these values being from the available statistics. A comparison of yields for 2015–2018 data obtained from fits to $K^\pm \to \pi^\pm \pi^+ \pi^-$ and $K^\pm \to \pi^\pm \mu^+ \mu^-$ misID in the chosen η-nLongTracks binning are given in Table 4.23 and Table 4.24.

Table 4.19:   Efficiencies   for   the   L0   trigger   calculated   using   an $\eta(K^\pm)$-$nLongTracks$ binned TISTOS method and using the misID as a proxy for the $K^\pm \to \pi^\pm \mu^+ \mu^-$ signal. These values are calculated after reconstruction and preselection, and determine the combined efficiency of the `L0Hadron`, `L0DiMuon` and `L0Muon` trigger lines.

	$K^\pm \to \pi^\pm \mu^+ \mu^-$ (MisID)	$K^\pm \to \pi^\pm \pi^+ \pi^-$
2015	0.127 ± 0.008	0.272 ± 0.015
2016	0.132 ± 0.005	0.210 ± 0.006
2017	0.127 ± 0.005	0.183 ± 0.005

Table 4.20: The thresholds for the L0 trigger lines used for $K^\pm \to \pi^\pm \mu^+ \mu^-$ and $K^\pm \to \pi^\pm \pi^+ \pi^-$ [40].

L0 Line	E_T/p_T Threshold		
	2015	2016	2017
Hadron	> 3.6 GeV	> 3.7 GeV	> 3.46 GeV
Muon	> 2.8 GeV	> 1.8 GeV	> 1.35 GeV
DiMuon	> 1.69 GeV ^{2}	> 2.25 GeV ^{2}	> 1.69 GeV ^{2}

For the HLT triggers a scan across all candidate trigger lines was performed on samples of MC to determine which lines were dominant in terms of pion and muon

---

[1]As described in section section 3.2.8, the TISTOS method has been validated externally to check that TIS triggers do not induce any bias.

(a) L0 full decision 'Dec'.

(b) L0 'TIS' events.

(c) L0 full decision 'TOS'.

(d) L0 events that are both 'TIS' and 'TOS'.
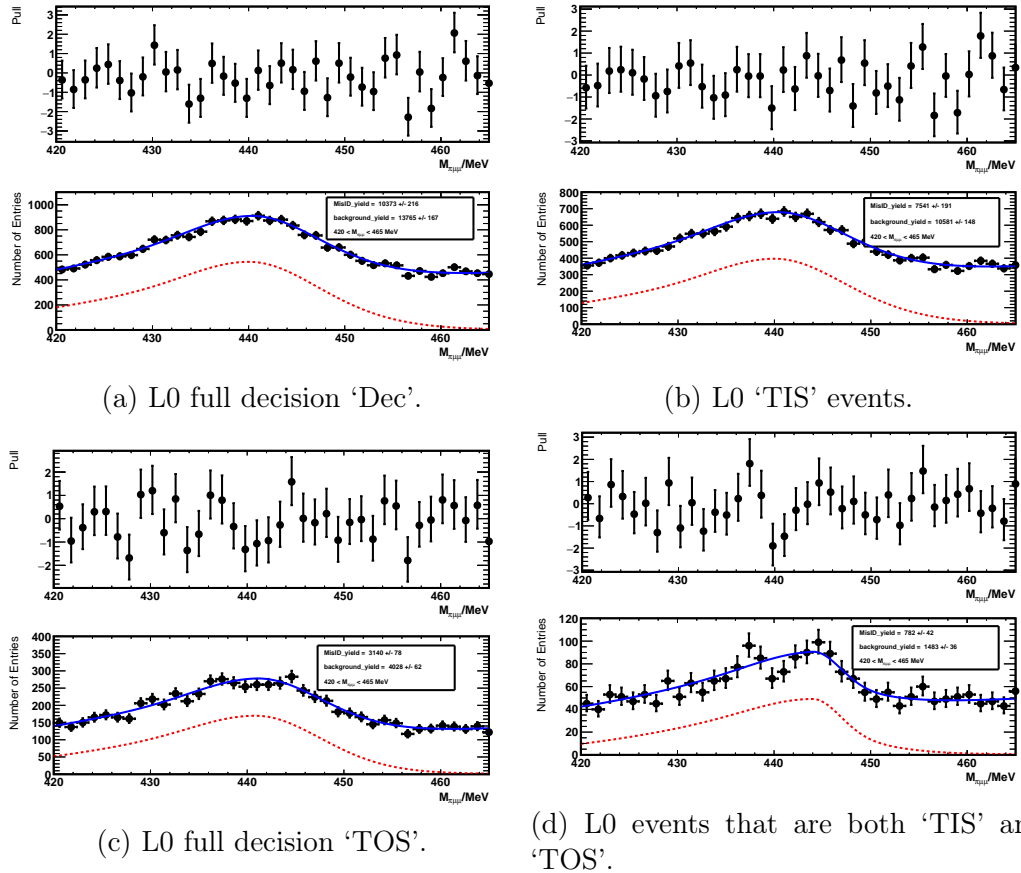
Figure 4.21: Example fits to the MisID peak in the invariant mass range $420 < M_{\pi\mu\mu} < 465$MeV for the 2D bin of $\eta \in [3.5, 4.0]$, $nLongTracks \in [40, 60]$ with pull distributions. A comparable fit quality was achieved across all bins.

selection, as well as ensuring they were not prescaled. The choice of lines are summarised in Table 4.21 and Table 4.22 along with the efficiencies which are obtained using the 2015 and 2016 MC.

Included within those lines chosen for HLT1 are `Hlt1TrackMVA` and `Hlt1TwoTrackMVA` in which a multivariate classifier, trained on single and two track combinations respectively, is utilised. For the case where a candidate contains only a subset of daughters, lines containing tight mass cuts will not be passed. To address this an alternative method is implemented within `Hlt1TwoTrackMVA` in which a constraint is instead applied to the corrected mass [91]:

$$m_{corrected} = \sqrt{m^2 + \left| p'_{T\text{missing}} \right|^2} + \left| p'_{T\text{missing}} \right|^2 . \tag{4.36}$$

Evident within the efficiency for HLT1 is a factor ~ 5 increase due to the introduction of the `DiMuonNoL0` line which includes cuts to select on 'soft' events with low transverse momentum at $p_T < 80\,\text{MeV}$, more optimal for selection of the $K^{\pm}$ which is long lived with a lifetime of $1.2 \times 10^{-8}\,\text{s}$ [92].

In Run 2 new trigger lines were implemented within HLT2 which were of great benefit towards this analysis, these included `Hlt2DiMuonSoft`, again optimised for selection on soft events, and `Hlt2RareStrangeKPiMuMu` optimised for constraining on $K^{\pm} \to \pi^{\pm}\mu^{+}\mu^{-}$ candidates before offline selection. `Hlt2DiMuonSoft` contains additional constraints on the dimuon vertex to ensure it lies within the VELO region, and a constraint on angular separation to lower background from 'clones' [83]. For $K^{\pm} \to \pi^{\pm}\pi^{+}\pi^{-}$ topological trigger lines are used for triggering at HLT2, with the term 'Topo' being used to describe tracks passing additional constraints in χ^2/ndf for impact parameters and lepton identification [42]. The selected Topo lines combine these constraints by implementing a multivariate classifier trained on subsets for the various 'n-body' categories. A full summary of all trigger line thresholds is given

in section A.5.

The thresholds for all trigger lines are listed within the tables in section A.5 and consist of cuts to track fit parameters and kinematic variables. The efficiency of a trigger line is calculated as a fraction of the total number events which passed the pre-selection (or stripping), i.e. the number of events obtained within the tuples constructed by DaVinci. The calculated is cumulative for each level, for example for HLT2:

$$\epsilon_{Hlt2} = \frac{(\text{L0Lines\&\&Hlt2Lines\&\&Hlt2Lines})}{(\text{L0Lines\&\&Hlt2Lines})}. \tag{4.37}$$

Table 4.21: Efficiency in $K^{\pm} \rightarrow \pi^{\pm}\mu^+\mu^-$ of trigger lines for 2015 and 2016 using Monte Carlo.

Trigger Line	$\epsilon_{line,trig,2015}$	$\epsilon_{line,trig,2016}$
Hlt1DiMuonLowMassDecision_TOS	0.075 ± 0.004	0.0436 ± 0.0028
Hlt1DiMuonNoL0Decision_TOS	-	0.473 ± 0.007
Hlt1TrackMVADecision_TOS	0.016 ± 0.002	0.017 ± 0.002
Hlt1TrackMuonDecision_TOS	0.041 ± 0.003	0.034 ± 0.003
Combined	0.094 ± 0.005	0.498 ± 0.007
Hlt2DiMuonSoftDecision_TOS	0.747 ± 0.023	0.844 ± 0.007
Hlt2RareStrangeKPiMuMuDecision_TOS	0.311 ± 0.024	0.506 ± 0.010
Combined	0.788 ± 0.022	0.878 ± 0.006

Table 4.22: Efficiency in $K^{\pm} \rightarrow \pi^{\pm}\pi^+\pi^-$ of trigger lines for 2015 and 2016 using Monte Carlo.

Trigger Line	$\epsilon_{line,trig,2015}$	$\epsilon_{line,trig,2016}$
Hlt1TrackMVADecision_TIS	0.105 ± 0.007	0.100 ± 0.005
Hlt1TwoTrackMVADecision_TIS	0.042 ± 0.004	0.039 ± 0.003
Combined	0.121 ± 0.007	0.116 ± 0.005
Hlt2Topo2BodyDecision_TIS	-	0.040 ± 0.010
Hlt2Topo__Decision_TIS	0.016 ± 0.008	-
Combined	0.020 ± 0.009	0.040 ± 0.010

Table 4.23: Yields obtained from fitting $K^{\pm} \to \pi^{\pm}\pi^{+}\pi^{-}$ data for all years in Run 2.

η	nLongTracks	$N_{sig,2015}$	$N_{sig,2016}$	$N_{sig,2017}$	$N_{sig,2018}$
		Dec			
[2.0, 3.7]	[0.0, 47.0]	4074 ± 101	13098 ± 214	12193 ± 206	18722 ± 275
[2.0, 3.7]	[47.0, 100.0]	5535 ± 116	17673 ± 333	11542 ± 346	23781 ± 371
[3.7, 5.0]	[0.0, 47.0]	4025 ± 98	15621 ± 232	13219 ± 256	17729 ± 277
[3.7, 5.0]	[47.0, 100.0]	5188 ± 155	44890 ± 159	22663 ± 41	21080 ± 630
		TISTOS			
[2.0, 3.7]	[0.0, 47.0]	49 ± 17	193 ± 35	188 ± 36	547 ± 46
[2.0, 3.7]	[47.0, 100.0]	102 ± 17	267 ± 74	336 ± 54	775 ± 54
[3.7, 5.0]	[0.0, 47.0]	82 ± 19	314 ± 36	320 ± 37	740 ± 2
[3.7, 5.0]	[47.0, 100.0]	142 ± 25	446 ± 56	496 ± 3	865 ± 12
		TIS			
[2.0, 3.7]	[0.0, 47.0]	3825 ± 98	11916 ± 215	11595 ± 214	16757 ± 256
[2.0, 3.7]	[47.0, 100.0]	5185 ± 113	15884 ± 329	15392 ± 292	21935 ± 350
[3.7, 5.0]	[0.0, 47.0]	3842 ± 95	12163 ± 246	11919 ± 209	14854 ± 261
[3.7, 5.0]	[47.0, 100.0]	4776 ± 148	37647 ± 103	16927 ± 47	19078 ± 467
		TOS			
[2.0, 3.7]	[0.0, 47.0]	317 ± 32	1520 ± 65	1696 ± 73	2405 ± 85
[2.0, 3.7]	[47.0, 100.0]	313 ± 26	1130 ± 58	1327 ± 61	1665 ± 81
[3.7, 5.0]	[0.0, 47.0]	286 ± 29	3108 ± 83	2757 ± 80	3619 ± 104
[3.7, 5.0]	[47.0, 100.0]	467 ± 46	1839 ± 94	1724 ± 96	2388 ± 137

Table 4.24: Yields obtained from fitting to the misID peak within $K^\pm \to \pi^\pm \mu^+ \mu^-$ data for each year in Run 2.

η	nLongTracks	$N_{misID,2015}$	$N_{misID,2016}$	$N_{misID,2017}$	$N_{misID,2018}$
		Dec			
[2.0, 3.5]	[0.0, 40.0]	2224 ± 86	1557 ± 80	2620 ± 87	3713 ± 107
[2.0, 3.5]	[100.0, 170.0]	209 ± 34	431 ± 50	451 ± 50	716 ± 86
[2.0, 3.5]	[40.0, 60.0]	3219 ± 113	2070 ± 100	3068 ± 104	4733 ± 131
[2.0, 3.5]	[60.0, 100.0]	2967 ± 113	1812 ± 113	2176 ± 113	5507 ± 221
[3.5, 4.0]	[0.0, 40.0]	2736 ± 91	3923 ± 99	3576 ± 73	4913 ± 113
[3.5, 4.0]	[100.0, 170.0]	1036 ± 123	2650 ± 138	2186 ± 129	2429 ± 113
[3.5, 4.0]	[40.0, 60.0]	5738 ± 161	5903 ± 168	5366 ± 176	7593 ± 125
[3.5, 4.0]	[60.0, 100.0]	10944 ± 353	7371 ± 266	5338 ± 201	8056 ± 274
[4.0, 5.0]	[0.0, 40.0]	2126 ± 71	3954 ± 110	3026 ± 92	4817 ± 124
[4.0, 5.0]	[100.0, 170.0]	568 ± 119	3408 ± 241	1957 ± 114	2528 ± 127
[4.0, 5.0]	[40.0, 60.0]	7948 ± 303	4934 ± 185	4239 ± 162	5618 ± 170
[4.0, 5.0]	[60.0, 100.0]	9051 ± 491	6798 ± 284	4570 ± 242	5898 ± 268
		TISTOS			
[2.0, 3.5]	[0.0, 40.0]	15 ± 7	51 ± 15	82 ± 19	81 ± 21
[2.0, 3.5]	[100.0, 170.0]	12 ± 65	28 ± 18	19 ± 7	7 ± 5
[2.0, 3.5]	[40.0, 60.0]	55 ± 16	89 ± 44	64 ± 15	215 ± 37
[2.0, 3.5]	[60.0, 100.0]	32 ± 16	33 ± 13	38 ± 16	107 ± 28
[3.5, 4.0]	[0.0, 40.0]	43 ± 12	60 ± 18	140 ± 26	402 ± 51
[3.5, 4.0]	[100.0, 170.0]	17 ± 12	41 ± 14	66 ± 14	44 ± 13
[3.5, 4.0]	[40.0, 60.0]	114 ± 22	205 ± 30	234 ± 27	488 ± 47
[3.5, 4.0]	[60.0, 100.0]	120 ± 25	72 ± 26	100 ± 21	420 ± 73
[4.0, 5.0]	[0.0, 40.0]	61 ± 15	81 ± 17	76 ± 19	174 ± 25
[4.0, 5.0]	[100.0, 170.0]	20 ± 17	83 ± 30	20 ± 15	50 ± 16
[4.0, 5.0]	[40.0, 60.0]	157 ± 29	266 ± 58	76 ± 20	312 ± 40
[4.0, 5.0]	[60.0, 100.0]	182 ± 40	184 ± 28	85 ± 34	209 ± 37
		TIS			
[2.0, 3.5]	[0.0, 40.0]	1304 ± 71	881 ± 65	1449 ± 68	2123 ± 86
[2.0, 3.5]	[100.0, 170.0]	145 ± 33	407 ± 64	326 ± 43	539 ± 55
[2.0, 3.5]	[40.0, 60.0]	2209 ± 98	1450 ± 85	2165 ± 88	3402 ± 112
[2.0, 3.5]	[60.0, 100.0]	1844 ± 90	1250 ± 62	1396 ± 90	2245 ± 121
[3.5, 4.0]	[0.0, 40.0]	1857 ± 78	2292 ± 79	2146 ± 73	3019 ± 93
[3.5, 4.0]	[100.0, 170.0]	639 ± 62	1958 ± 96	1330 ± 78	2131 ± 152
[3.5, 4.0]	[40.0, 60.0]	7696 ± 231	4383 ± 94	3912 ± 168	5610 ± 110
[3.5, 4.0]	[60.0, 100.0]	4350 ± 220	4832 ± 221	3513 ± 165	5639 ± 221
[4.0, 5.0]	[0.0, 40.0]	1501 ± 85	1999 ± 82	1556 ± 69	2435 ± 95
[4.0, 5.0]	[100.0, 170.0]	211 ± 272	2048 ± 113	1284 ± 86	2181 ± 171
[4.0, 5.0]	[40.0, 60.0]	3494 ± 186	3313 ± 162	2958 ± 142	3733 ± 138
[4.0, 5.0]	[60.0, 100.0]	5571 ± 397	4046 ± 217	2812 ± 183	3839 ± 220
		TOS			
[2.0, 3.5]	[0.0, 40.0]	912 ± 52	739 ± 54	1326 ± 62	1666 ± 70
[2.0, 3.5]	[100.0, 170.0]	73 ± 23	165 ± 36	31 ± 18	40 ± 12
[2.0, 3.5]	[40.0, 60.0]	845 ± 57	636 ± 58	927 ± 62	1326 ± 74
[2.0, 3.5]	[60.0, 100.0]	405 ± 44	323 ± 44	424 ± 71	485 ± 55
[3.5, 4.0]	[0.0, 40.0]	922 ± 48	1769 ± 61	1602 ± 58	2074 ± 69
[3.5, 4.0]	[100.0, 170.0]	229 ± 52	235 ± 34	267 ± 34	243 ± 34
[3.5, 4.0]	[40.0, 60.0]	1382 ± 76	1664 ± 76	1751 ± 79	2319 ± 85
[3.5, 4.0]	[60.0, 100.0]	801 ± 67	1123 ± 82	1036 ± 118	1421 ± 172
[4.0, 5.0]	[0.0, 40.0]	689 ± 55	2142 ± 78	1574 ± 63	2488 ± 81
[4.0, 5.0]	[100.0, 170.0]	71 ± 34	542 ± 83	299 ± 70	261 ± 42
[4.0, 5.0]	[40.0, 60.0]	1261 ± 93	1552 ± 78	1464 ± 84	2081 ± 128
[4.0, 5.0]	[60.0, 100.0]	1112 ± 181	1335 ± 124	937 ± 86	988 ± 74

4.2.7   Fit Models

The fits within this analysis are performed using the *RooFit* library contained within ROOT. To obtain final yields and parameters to model the invariant mass distribution extended fits are performed unbinned.

The proximity of the misID peak to the signal region meant any fit to data required a component to model the distribution. Excluding such a component risked loss of fit accuracy due to the reduced lower mass sideband of $\sim$30 MeV affecting fit stability in this region.

The samples of $K^{\pm} \to \pi^{\pm}\pi^{+}\pi^{-}$ MC were used to determine the shape of the misID distribution by applying a change in mass hypothesis to the daughter particles, setting any combination of two pions to have the mass of two muons. No significant distortion of misID peak in mass distribution due to muon identification requirements is expected because the efficiency related to this identification is relatively insensitive to transverse momentum. A simple script was written to read in each event and perform this substitution using the four momentum information of the three daughters, and referring to the PDG for the muon and pion masses. The results are shown in Figure 4.22 and are fitted using a hybrid PDF consisting of a bifurcated Gaussian (a Gaussian with different widths above and below the mean), and double Crystal Ball (DCB). The form of the single Crystal Ball function is [93, 94]:

$$f(x; \alpha, n, \bar{x}, \sigma) = \begin{cases} e^{-\frac{1}{2}\left(\frac{x-\bar{x}}{\sigma}\right)^2}, & \text{for } \frac{x-\bar{x}}{\sigma} > -\alpha \\ \left(\frac{n}{|\alpha|}\right)^n e^{-\frac{|\alpha|^2}{2}} \left(\frac{n}{|\alpha|} - |\alpha| - \frac{x-\bar{x}}{\sigma}\right)^{-n}, & \text{for } \frac{x-\bar{x}}{\sigma} \leq -\alpha \end{cases} \tag{4.38}$$

where $\bar{x}$, σ are the mean and standard deviation of the Gaussian core and α and n determine the parameters of the single sided power-law tail. Within the fit the power-law components of the Crystal Ball functions are on opposite sides (positive and negative α). In terms of quality of fit, for 2016 MC a χ^2/ndf value of 1.29 was

recorded showing a high level of modelling accuracy.

(a) MC2015   (b) MC2016
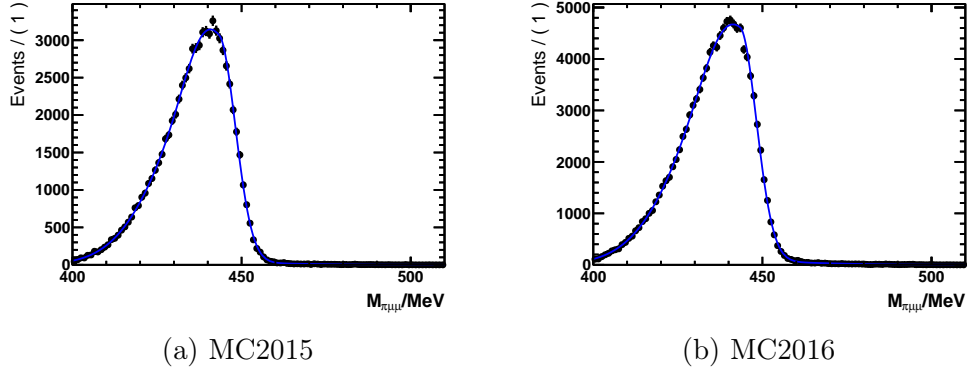
Figure 4.22: Fitting of the double misidentification of pions in $K^{\pm} \to \pi^{\pm}\pi^{+}\pi^{-}$ as muons simulated using MC.

Fitting of the normalisation channel of $K^{\pm} \to \pi^{\pm}\pi^{+}\pi^{-}$ was performed using Hypatia/Ipatia functions which have a hyperbolic core as opposed to the usual Gaussian, and account for uncertainty by using exponential tails [95]. The combinatorial background for the invariant mass distribution of the normalisation channel was modelled using an positive exponential function for all three years of data taking within the range $M_{\pi\pi\pi} \in [475, 515]$MeV after all cuts have been applied. Beyond this range the differences between 2015 and 2016 distributions come into effect.

The standard deviation σ of the signal PDF when fitting to data, along with parameters describing the tail of the misID distribution within the signal region are Gaussian constrained based on fits to MC, further details of these constraints are given in section 4.2.10. The χ^2/ndf values obtained from fitting to $K^{\pm} \to \pi^{\pm}\mu^{+}\mu^{-}$ and $K^{\pm} \to \pi^{\pm}\pi^{+}\pi^{-}$ MC are given in Table 4.25, in general the results show a good level of uncertainty estimation, most values lying close to 1, fits to 2015 MC showing slight overestimation for $K^{\pm} \to \pi^{\pm}\pi^{+}\pi^{-}$. The fits to data are shown in Figure 4.23 and are also tested in terms of fit quality using χ^2/ndf, the results of which are given in Table 4.26 and the signal yields $N_{\pi\pi\pi}$ are summarised in Table 4.27.

Although the data for $K^{\pm} \to \pi^{\pm}\mu^{+}\mu^{-}$ was initially blinded to the analyst whilst

Table 4.25: $\chi^2/$ndf values as a quantitative assessment of the quality of fit for $K^\pm \to \pi^\pm \mu^+ \mu^-$ and $K^\pm \to \pi^\pm \pi^+ \pi^-$ 2015 and 2016 MC.

	2015	2016
$K^\pm \to \pi^\pm \mu^+ \mu^-$	0.922	1.109
$K^\pm \to \pi^\pm \pi^+ \pi^-$	0.622	0.883

Table 4.26: Verification of fit quality for $K^\pm \to \pi^\pm \pi^+ \pi^-$ data performed qunatitatively using the $\chi^2/$ndf test.

Year	$\chi^2/$ndf for $K^\pm \to \pi^\pm \pi^+ \pi^-$ Fit
2015	0.730
2016	1.463
2017	1.778
2018	1.474

choosing the model PDF, the fit was performed on the full rare decay data sample with the invariant mass distribution within the signal region and parameters of the signal distribution being hidden. To model the invariant mass distribution for this dataset, alike to $K^\pm \to \pi^\pm \pi^+ \pi^-$, an Ipatia function is used to fit the signal, combined with an exponential and the misID shape for background to form the total function. A summary of the constraints applied to this fitting function is given in section 4.2.10.

All fits are performed using extended PDFs and return the yields for each event category.

Table 4.27: Signal yields of $K^\pm \to \pi^\pm \pi^+ \pi^-$ data for 2015–2018 with their statistical uncertainties.

	2015	2016	2017	2018
$N_{\pi\pi\pi}$	$(1.127 \pm 0.011) \times 10^4$	$(1.307 \pm 0.004) \times 10^5$	$(1.391 \pm 0.004) \times 10^5$	$(1.193 \pm 0.004) \times 10^5$

4.2.8   Prediction of misID Yield from Efficiencies

The presence of a misID peak in $K^\pm \to \pi^\pm \mu^+ \mu^-$ data provides a means of testing the methods used within this analysis. Testing the behaviour of the misID distribution

(a) 2015 Stripping24.

(b) 2016 Stripping28r1.

(c) 2017 Stripping29r2.

(d) 2018 Stripping34.
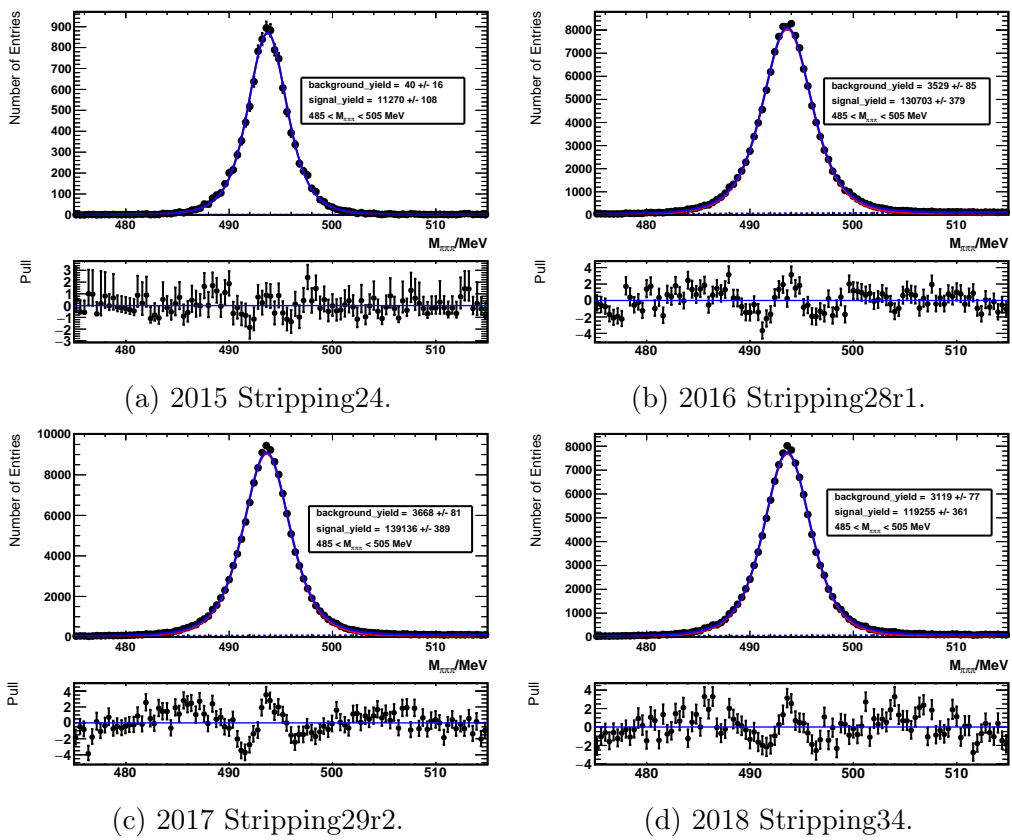
Figure 4.23: Fits to $K^{\pm} \rightarrow \pi^{\pm}\pi^{+}\pi^{-}$ data performed for the years 2015–2018.

is essential to confirm whether the use of this peak as a proxy for the signal when performing the TISTOS method for the L0 trigger efficiency is justified. A prediction for the misID is given using the yield of $K^{\pm} \to \pi^{\pm}\pi^{+}\pi^{-}$ signal in data:

$$N_{misID} \sim \left(\frac{\epsilon^{misID}}{\epsilon^{\pi\pi\pi}} \right) N_{\pi\pi\pi}. \qquad (4.39)$$

Using the MC samples for 2016 a chain of efficiencies is obtained similar to those for the single event sensitivity, up until the point of selection the efficiencies for $K^{\pm} \to \pi^{\pm}\pi^{+}\pi^{-}$ signal and misID are the same and so cancel in any ratio, i.e.:

$$\left(\frac{\epsilon^{misID}}{\epsilon^{\pi\pi\pi}} \right)_{gen} = \left(\frac{\epsilon^{misID}}{\epsilon^{\pi\pi\pi}} \right)_{filt} = 1. \qquad (4.40)$$

To determine the probability of a $K^{\pm} \to \pi^{\pm}\pi^{+}\pi^{-}$ event being misidentified as $K^{\pm} \to \pi^{\pm}\mu^{+}\mu^{-}$, the MC is firstly manually stripped using the same selections as are present within the $K^{\pm} \to \pi^{\pm}\mu^{+}\mu^{-}$ stripping line with the exception of the `isMuon` cut which is applied to candidate muons and is not modelled well within the sample. This gives the selection efficiency ϵ_{sel}^{misID} for the change in mass hypothesis. The efficiency related to the constraint applied by `isMuon` to two of the daughter pions is then determined using the *PidCalib* software which returns an efficiency based on weights obtained from binning data in a p_T, number of tracks and η phase space applying cuts individually to each particle.

The values for these efficiencies are given in Table 4.28. Analogous to the selection efficiency for $K^{\pm} \to \pi^{\pm}\pi^{+}\pi^{-}$ is the combined misID and selection efficiency, $\epsilon_{strip \cdot sel}^{misID}$. As expected this is far lower than the value for $K^{\pm} \to \pi^{\pm}\pi^{+}\pi^{-}$ at two orders of magnitude. Due to the low statistics when passing the $K^{\pm} \to \pi^{\pm}\pi^{+}\pi^{-}$ MC through a $K^{\pm} \to \pi^{\pm}\mu^{+}\mu^{-}$ selection not all of the component efficiencies can be re-calculated for the misID , for the others the pragmatic approach has been adopted that the

results of $K^{\pm} \to \pi^{\pm}\mu^{+}\mu^{-}$ MC can be used, the comparison is performed without application of the PID cuts as these greatly suppresses the misID . The efficiency components used in this comparison are given in Table 4.29.

The 2016 $K^{\pm} \to \pi^{\pm}\pi^{+}\pi^{-}$ data yield was measured to be:

$$N_{\pi\pi\pi} = (1.555 \pm 0.004) \times 10^5. \tag{4.41}$$

The final result using these efficiencies and the yield is given in Table 4.30. The results suggest an incompatibility which motivated checks of all methods within the analysis. As the discrepancy remained after all proposed checks were made, the decision was taken to apply the difference as a correction factor:

$$\beta = 5.25 \pm 1.01 \tag{4.42}$$

giving $\Delta\beta/\beta = 18\%$.

Table 4.28: Selection efficiencies from performing the $K^{\pm} \to \pi^{\pm}\mu^{+}\mu^{-}$ selection (without `isMuon`) within the `KPiMuMuLine` on $K^{\pm} \to \pi^{\pm}\pi^{+}\pi^{-}$ MC, ϵ_{sel}, and the efficiency of the `isMuon == 1.0` cut for MisID, $\epsilon_{\text{isMuon}(\pi\pi)}$.

	$\epsilon_{\text{isMuon}(\pi\pi)}/10^{-2}$	ϵ_{sel}	$\epsilon_{strip \cdot sel}/10^{-3}$
2015	0.2962 ± 0.0005	0.6072 ± 0.0064	1.799 ± 0.004
2016	0.2301 ± 0.0004	0.6051 ± 0.0022	1.392 ± 0.001

Table 4.29: Efficiencies obtained from applying the selection of $K^{\pm} \to \pi^{\pm}\mu^{+}\mu^{-}$ to $K^{\pm} \to \pi^{\pm}\pi^{+}\pi^{-}$ 2016 MC.

	$K^{\pm} \to \pi^{\pm}\pi^{+}\pi^{-}$	MisID
$\epsilon_{strip \cdot sel}(= \epsilon_{strip \cdot sel}^{misID})$	0.4589 ± 0.0017	0.0019 ± 0.0002
ϵ_{Cut}	0.978 ± 0.005	0.972 ± 0.011
ϵ_{Ghost}	0.923 ± 0.001	0.821 ± 0.024
ϵ_{Trig}	0.0014 ± 0.0002	0.0673 ± 0.0015
ϵ_{BDT}	0.837 ± 0.002	0.530 ± 0.035

Table 4.30: Comparison of fitted misID data from the $K^{\pm} \to \pi^{\pm}\mu^{+}\mu^{-}$ invariant mass spectrum with θ_{ij} , Ghost, trigger and BDT cuts applied (No PID cut).

	Data	Predicted
N_{MisID}	$(9.39 \pm 0.03) \times 10^4$	$(1.79 \pm 0.35) \times 10^4$

4.2.9 Blinded Results

Before unblinding a prediction was made to determine the number of events for $K^{\pm} \to \pi^{\pm}\mu^{+}\mu^{-}$ expected for each year in 2015–2017 applying all the cuts selected through the optimisation process and fitting the data. Inserting all the relevant efficiencies into Equation 4.30 and using the pre-analysis efficiencies for 2016 MC for both 2016 and 2017, and the correction factor deduced during the misID investigation, the results in Table 4.31 were obtained.

With the trigger system for 2015 being less optimised for these soft kaon decays the effect is evident in the loss in efficiency, which when combined with statistics gives a yield prediction below a single event, therefore the choice was taken to fully evaluate only 2016 and 2017 data when permission was granted for unblinding. At this stage the total yield for both years was predicted to be:

$$N^{\pi\mu\mu}_{predicted}(2016 - 2017) = 95 \pm 21, \tag{4.43}$$

and with this prediction the move was made to then unblind the data.

Table 4.31: Predicted single event sensitivities, $\alpha_{\pi\mu^{+}\mu^{-}}$, signal yields, and significance values for $K^{\pm} \to \pi^{\pm}\mu^{+}\mu^{-}$ for 2015–2018 data.

Year	$\alpha_{\pi\mu\mu}$	$N_{\pi\mu\mu}$	N_{Bkg}	$\frac{N_{\pi\mu\mu}}{\sqrt{N_{Bkg}}}$
2015	$(2.10 \pm 1.00) \times 10^{-7}$	0.5 ± 0.2	9.3 ± 1.5	0.2 ± 0.1
2016	$(1.98 \pm 0.61) \times 10^{-9}$	48 ± 15	78 ± 14	5.4 ± 1.8
2017	$(1.98 \pm 0.61) \times 10^{-9}$	47 ± 15	75 ± 4	5.4 ± 1.8
2018	$(2.10 \pm 0.70) \times 10^{-9}$	44 ± 14	62 ± 4	5.6 ± 1.8

Toy Studies

Testing of the fit model is mandatory before unblinding of the data can occur, should there be sufficient statistics for a branching ratio measurement the value obtained from fitting for the signal yield may be more or less than expected and as such the model must account for this.

The method for performing this test is a pseudoexperiment known as a *toy study*, and consists of repetitions of dataset generation using an instance of the model PDF.

The dominant uncertainties are expected to be from the normalisation due to lack of knowledge of yields, therefore during generation all yield parameters of the PDF were allowed to fluctuate using a Poisson random number generator. The resultant toy datasets are then fitted with another instance of the same model matching that which is used for the final fit to data. Examination of the pulls then allows the power of the fit to be observed, with a good quality fit showing the pulls for the yields to be Gaussian in distribution with a low value of σ and μ of zero. For $K^{\pm} \to \pi^{\pm}\mu^{+}\mu^{-}$ there are three yields, signal, background and misID which are measured within the signal region.

For this analysis 1,000 toys were created to model 2016 data for each scaling of the SM prediction by 0.1, 1 and 10. Given the compatibility between 2016 and 2017 data as proven through sWeighting, the study is representative of fits to both years and ultimately the two datasets combined. Rather than generate a single dataset as a whole, the yields obtained either from fits to data (in the case of background and misID) or from prediction (for signal) were used to generate proportionally three data subsets which were then combined into a single sample.

The results for the toys are shown in Figure 4.24 and numerical values given in Table 4.32. The test proved essential in ensuring the fit was correctly prepared for unblinding,

revealing and helping to debug an issue where a fraction of the signal yield was mistaken as background due to constraints on the signal width parameter being too tight. Although the mass binning of the toy study shown is below the signal resolution this has no bias on the result as the fit is performed unbinned.

Table 4.32: Mean and RMS values for the pulls of each yield category within the 2016 S28 Toy studies.

| | Yield Pulls | | | | | |
| | Signal | | Background | | MisID | |
$x\mathcal{B}$	μ	RMS	μ	RMS	μ	RMS
0.1	-0.0563	0.9504	0.0922	0.5809	-0.0252	0.7945
1	-0.0030	0.9426	0.0830	0.5892	0.0260	0.7952
10	0.0021	0.9685	0.0794	0.5973	-0.0103	0.8050

4.2.10   Systematics

All contributions to the systematic uncertainty are summarised in Table 4.33. The dominant contribution comes from the PID cut applied to $K^{\pm} \to \pi^{\pm}\mu^{+}\mu^{-}$ and is due to the calibration procedure. Given the use of normalisation channel for the measurement of $K^{\pm} \to \pi^{\pm}\mu^{+}\mu^{-}$ branching ratio, it was asserted that the dominant contributions would cancel within the ratio, and considering the size of systematics in Table 4.33, any effects are expected to be small in comparison and are therefore not considered further. The systematics are assumed to be uncorrelated and so added in quadrature.

Systematics in the Fitting Procedure

For the purpose of simplifying the systematics associated with fitting, constraints are applied to the fit model to minimise the number of free parameters. Firstly an Ipatia function is fitted to the samples of $K^{\pm} \to \pi^{\pm}\pi^{+}\pi^{-}$ MC, the shape parameters are stored and then used for the construction of the signal PDF when performing
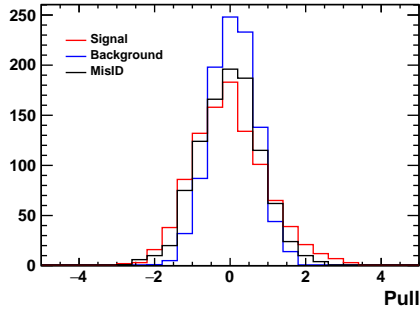
(a) Standard Model Branching Ratio Yield Pulls
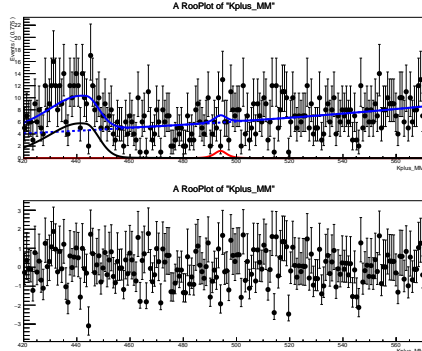
(b) Standard Model Branching Ratio Example Toy
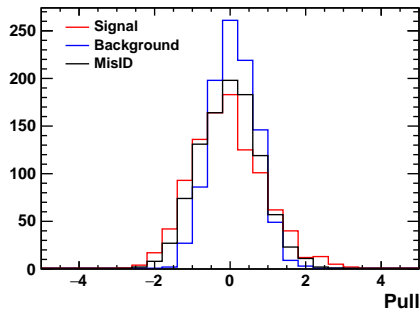
(c) 0.1× Standard Model Branching Ratio Yield Pulls
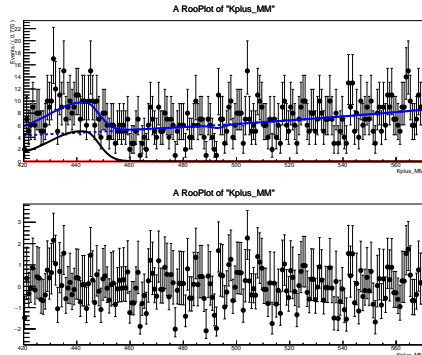
(d) 0.1× Standard Model Branching Ratio Example Toy
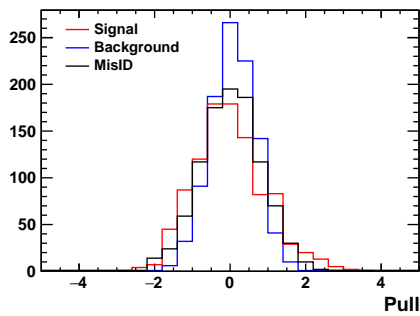
(e) 10× Standard Model Branching Ratio Pulls
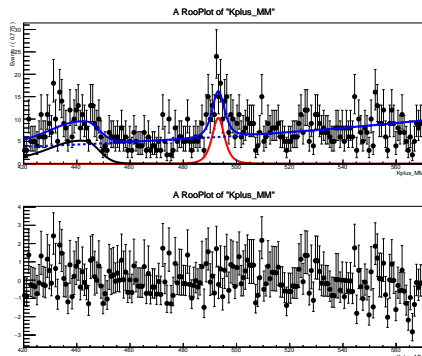
(f) 10× Standard Model Branching Ratio Example Toy

Figure 4.24: Results of toy study to emulate 2016 S28 $K^{\pm} \to \pi^{\pm}\mu^{+}\mu^{-}$ data for various branching ratios, on the left are the pulls for the toys, and the right an example invariant mass distribution from one of the toys.

Table 4.33: Components of systematic uncertainty within the branching ratio measurement of $K^\pm \to \pi^\pm \mu^+ \mu^-$ for 2016–2017 data.

Type	Uncertainty Component/%	
	2016	2017
PDG $K^\pm \to \pi^\pm \pi^+ \pi^-$ Measurement [12]	0.4	0.4
MC Stats	25	25
Modelling of $K^\pm \to \pi^\pm \pi^+ \pi^-$ BDT	0.3	0.1
Modelling of nSPDHits	25	20
MisID Fit	0.1	0.1
Residual Modelling Correction, β (Equation 4.42)	18	18
Modelling of PID	32	32

the fit to $K^\pm \to \pi^\pm \pi^+ \pi^-$ data. During the data fitting, all parameters are held constant with exception of the power of the exponential function describing the combinatorial background, the mean μ which is allowed to float, and the width σ which is Gaussian constrained. The value obtained for σ obtained from fitting to MC is used as the mean μ_i, and the uncertainty on this value for the width σ_i in the Gaussian constraint:

$$F_{sig}(x) = Ae^{cx} + (1-A)\text{Ipatia}(x; \mu, \sigma_s, \lambda, \beta, \alpha, n) \times \text{Gauss}(\sigma_s; \mu(\sigma_s), \sigma(\sigma_s)). \quad (4.44)$$

As the width determined from this fit to data differs by more than that allowed within the Gaussian constrain, an additional multiplicative factor is deduced and used to account for the modelling of the width in simulation. This additional factor is subsequently applied to the equivalent width parameter derived from fits to $K^\pm \to \pi^\pm \mu^+ \mu^-$ simulation when constructing the PDF used to fit $K^\pm \to \pi^\pm \mu^+ \mu^-$ data.

For the component of background due to misID , all parameters describing the invariant mass shape are held constant to those obtained from MC fits, with the exception of those describing the right hand tail passing below the signal region. These parameters are also Gaussian constrained from MC in a manner identical to

those within the signal PDF:

$$
\begin{aligned}
F_{misID}(x) \;=\; & \mathrm{CB}_1(x; \mu, \sigma_1, \alpha_1, n) \\
& +\mathrm{CB}_2(x; \mu, \sigma_1, \alpha_2, n) \times \mathrm{Gauss}(\alpha_2; \mu(\alpha_2), \sigma(\alpha_2)) \times \mathrm{Gauss}(\sigma_2; \mu(\sigma_2), \sigma(\sigma_2)) \\
& +\mathrm{BifGauss}(x; \mu, \sigma_3, \sigma_4) \times \mathrm{Gauss}(\sigma_4; \mu(\sigma_4), \sigma(\sigma_4)) \tag{4.45}
\end{aligned}
$$

The systematic assigned to the misID yield within the signal region is taken from the uncertainty on the yield after fitting. This is largely due to the complexity of the fit model for the misID distribution meaning creation of an alternate model would have proven difficult.

To ensure the choice of fit model for the signal had no influence on the results for single event sensitivity, and ultimately the predicted $K^{\pm} \to \pi^{\pm}\mu^{+}\mu^{-}$ yield, the procedure of fitting to $K^{\pm} \to \pi^{\pm}\pi^{+}\pi^{-}$ and $K^{\pm} \to \pi^{\pm}\mu^{+}\mu^{-}$ data and MC was repeated using alternative models. For testing how choice of signal model influences the final SES values a PDF consisting of a Double Crystal Ball and Gaussian was trialled. The resultant values for single event sensitivity, $\alpha_{\pi\mu\mu}$, and significance, $N_{\pi\mu\mu}/\sqrt{N_{Bkg}}$, are compared to those in Table 4.31, and are given in Table 4.34 and Table 4.35 respectively. To then test the choice of background model, the single event sensitivities were again redetermined using an alternative of a 2nd Order Polynomial, with the signal held as the original Ipatia function, results are given in Table 4.36 and Table 4.37. Due to the values obtained from these results being compatible within the respective uncertainties for each to the chosen model of Ipatia PDF for signal and exponential for background, it was deemed unnecessary to assign a systematic uncertainty for this.

Table 4.34: Single event sensitivities for 2015–2018 data using an alternative signal model of a double Crystal Ball and Gaussian PDF.

	$\alpha_{\pi\mu\mu}$
2015	$(2.2 \pm 1.0) \times 10^{-7}$
2016	$(1.94 \pm 0.61) \times 10^{-9}$
2017	$(1.98 \pm 0.61) \times 10^{-9}$
2018	$(2.11 \pm 0.66) \times 10^{-9}$

Table 4.35: Predicted signal yields and significance values for $K^{\pm} \to \pi^{\pm}\mu^{+}\mu^{-}$ for 2015–2018 data using alternative signal model of double Crystal Ball and Gaussian.

Year	$N_{\pi\mu\mu}$	N_{Bkg}	$\frac{N_{\pi\mu\mu}}{\sqrt{N_{Bkg}}}$
2015	0.4 ± 0.2	6.9 ± 1.3	0.2 ± 0.1
2016	48 ± 15	75.5 ± 4.4	1.1 ± 0.3
2017	47 ± 15	74.3 ± 4.4	1.1 ± 0.3
2018	44 ± 14	62.2 ± 4.1	1.1 ± 0.3

Table 4.36: Single event sensitivities for 2015–2018 data using an alternative background model of a 2nd Order Polynomial PDF.

	$\alpha_{\pi\mu\mu}$
2015	$(2.3 \pm 1.1) \times 10^{-7}$
2016	$(2.19 \pm 0.68) \times 10^{-9}$
2017	$(2.19 \pm 0.66) \times 10^{-9}$
2018	$(2.42 \pm 0.75) \times 10^{-9}$

Table 4.37: Predicted signal yields and significance values for $K^{\pm} \to \pi^{\pm}\mu^{+}\mu^{-}$ for 2015–2018 data using alternative signal model of 2nd Order Polynomial.

Year	$N_{\pi\mu\mu}$	N_{Bkg}	$\frac{N_{\pi\mu\mu}}{\sqrt{N_{Bkg}}}$
2015	0.4 ± 0.2	8 ± 1	0.14 ± 0.07
2016	44 ± 13	77 ± 4	5.0 ± 1.5
2017	43 ± 13	77 ± 4	5.0 ± 1.5
2018	40 ± 13	64 ± 4	5.0 ± 1.6

Modelling of SPD Hits

The modelling of the number of SPD hits within the detector is poorly represented by MC as can be seen in the comparison of 2016 $K^{\pm} \to \pi^{\pm}\pi^{+}\pi^{-}$ MC with sWeighted data in Figure 4.25. The distributions become more comparable when a factor of ~ 20 is applied to the x axis of the MC histogram. The lack of signal peak within data due to the cut at 450 makes this scaling very approximate, as such a systematic has been assigned to account for this, accounting for the effect on the $K^{\pm} \to \pi^{\pm}\pi^{+}\pi^{-}$ GEC efficiency (and as such the $K^{\pm} \to \pi^{\pm}\mu^{+}\mu^{-}$ GEC efficiency due to the compatibility exhibited in both MC samples) due to varying this factor within the range [18, 22].
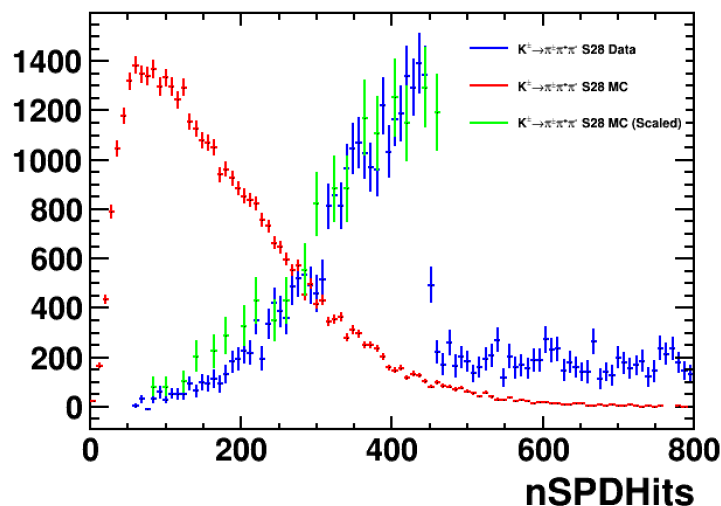
Figure 4.25: Comparison between 2016 sWeighted data and MC for $K^{\pm} \to \pi^{\pm}\pi^{+}\pi^{-}$, showing the effect of scaling the MC by a factor of 20, the method used to determine the GEC efficiencies for $K^{\pm} \to \pi^{\pm}\pi^{+}\pi^{-}$ and $K^{\pm} \to \pi^{\pm}\mu^{+}\mu^{-}$.

Modelling of $K^{\pm} \to \pi^{\pm}\pi^{+}\pi^{-}$ BDT

A systematic for the trained classifier for $K^{\pm} \to \pi^{\pm}\pi^{+}\pi^{-}$ is obtained by plotting the signal yield in bins of BDT chosen to allow suitable precision on the comparisons made to MC.

As there is no significant signal for $K^{\pm} \to \pi^{\pm}\mu^{+}\mu^{-}$ if was seen as inappropriate to

perform the same procedure on the rare decay due to limiting statistics.

The bin with the greatest deviation between the two samples is then used, this deviation is calculated as a percentage with respect to the yield in data and is then assigned to be the uncertainty value on the BDT.

(a) 2015 Stripping24.

(b) 2016 Stripping28r1.

(c) 2017 Stripping29r2.
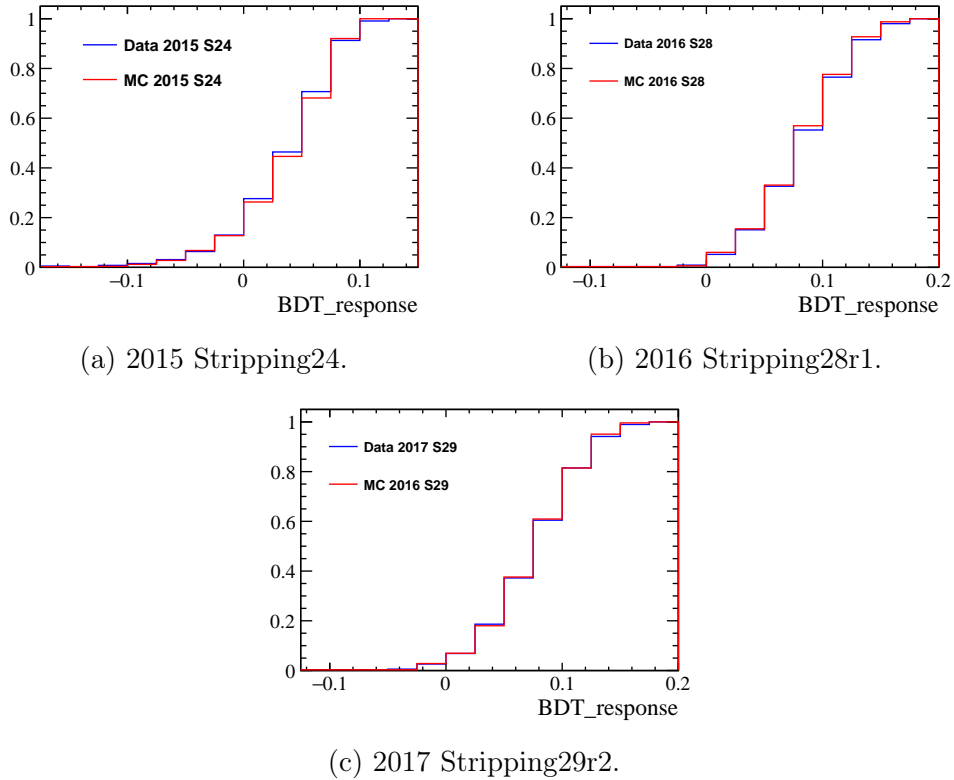
Figure 4.26: Comparison of signal yield distribution in bins of BDT variable for $K^{\pm} \to \pi^{\pm}\pi^{+}\pi^{-}$ data and MC. As 2017 MC was not available 2016 MC was used to train the 2017 BDT and so is shown for the 2017 comparison also.

Table 4.38: Systematic uncertainties for each BDT calculated for $K^{\pm} \to \pi^{\pm}\pi^{+}\pi^{-}$ by finding the maximum difference between the binned BDT response distributions for data and MC. Here Δ is defined as the greatest percentage difference with respect to data.

	BDT Response Bin	MC vs Signal BDT ($\Delta\%$)
2015	[0.050, 0.075]	3.63
2016	[0.075, 0.100]	3.10
2017	[0.125, 0.150]	0.99

Modelling of PID

Although the procedure of correcting the distributions of PID variables in MC ensures a higher compatibility with the data the process is not without its systematic effects. For example, changes in the binning within the four dimensional phase space (see section 3.4) during kernel density estimation could have an impact on the replacement distributions produced by PIDGen. To investigate this a selection of different binnings were used to generate the π/μ ProbNN variables used within this analysis, and new values for the efficiency $\epsilon_{BDT.PID}$ were extracted. It was found that in the case of $K^{\pm} \to \pi^{\pm}\mu^{+}\mu^{-}$ the efficiency varied by up to 32% of that which had been obtained previously.

In order to ensure the selected binning did not effect the value chosen for the optimal cut across the ProbNNμ vs BDT phase space, a scan was performed across the ProbNNμ variable holding all other cut values constant and comparing the maxima for each of the new samples produced by PIDGen. The resultant plot given in Figure 4.27 shows there to be no dependence of optimal value on the binning scheme.
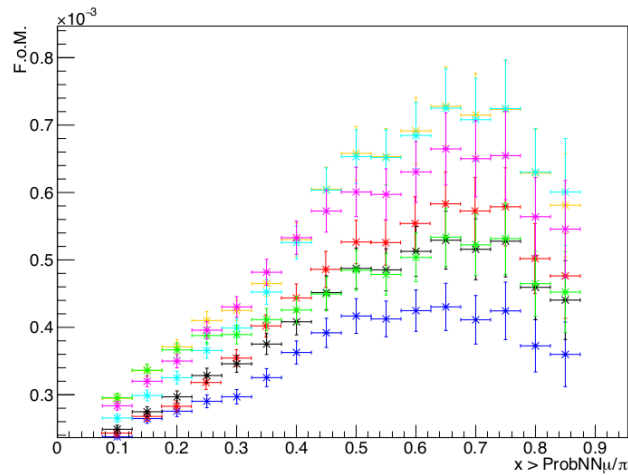
Figure 4.27: Comparison of generated samples for the variable ProbNNμ in $K^{\pm} \to \pi^{\pm}\mu^{+}\mu^{-}$ MC using PIDGen with different binning schemes. Each set of points represents a different binning of the η, nTracks, p and PID variables.

4.2.11   Measurement of Branching Ratio

Due to 2017 data being handled in the exact same manner as 2016, and the confirmation from testing that both datasets share the same kinematic behaviour and efficiency, the decision was made to fit both together after combining the two SES values:

$$\alpha_{2016,2017}^{\pi\mu\mu} = (2.15 \pm 0.02_{stat} \pm 0.79_{sys}) \times 10^{-9}. \qquad (4.46)$$

The results of fitting to the combined data sample for 2016 and 2017 are shown in Figure 4.28, with the yields given in Table 4.39 and the parameters of the fit model in Table 4.40. The χ^2/ndf value of 0.753 suggests slight overestimation of the respective uncertainties.
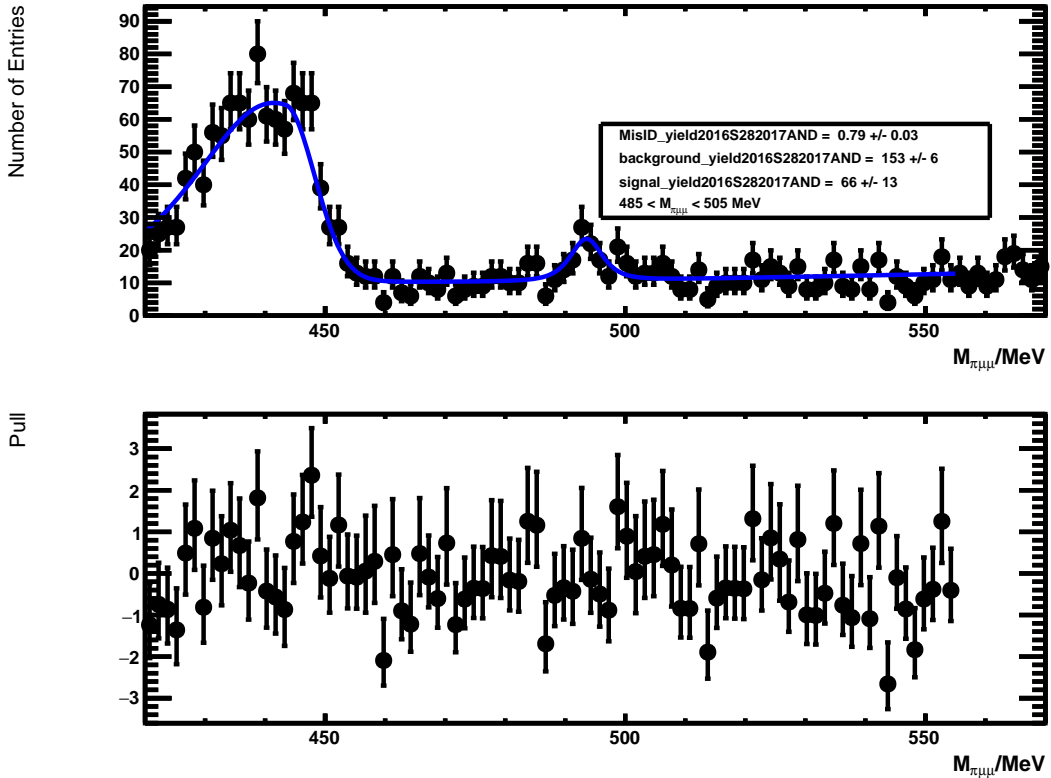
Figure 4.28: Final fits combined 2016 Stripping28 and 2017 Stripping29 data for $K^{\pm} \to \pi^{\pm}\mu^{+}\mu^{-}$.

Combining these fit results with the SES in Equation 4.46, a branching ratio for

Table 4.39: Yields obtained in the region $M_{\pi\mu\mu}[485, 505]\,\mathrm{MeV}$ from fitting the combined Stripping28 and Stripping29r2 $K^{\pm} \to \pi^{\pm}\mu^{+}\mu^{-}$ data for the years 2016 and 2017 respectively and the resulting χ^2/ndf value for this fit.

$N_{\pi\mu\mu}$	66 ± 13
N_{Bkg}	153 ± 6
N_{MisID}	0.79 ± 0.03
χ^2/ndf	0.753

Table 4.40: Fit parameters from the combined fit to 2016 and 2017 $K^{\pm} \to \pi^{\pm}\mu^{+}\mu^{-}$ data. Those without uncertainties have been held constant based on fits to $K^{\pm} \to \pi^{\pm}\pi^{+}\pi^{-}$ data compared with $K^{\pm} \to \pi^{\pm}\mu^{+}\mu^{-}$ MC.

Signal (Ipatia)	
σ	5.02 ± 1.49
μ	493 ± 1
α	4.0
fb	0
l	-2.1
n	1.0
ζ	0
Background (Exponential)	
λ	$(2.02 \pm 1.45) \times 10^{-3}$
MisID (Double Crystal Ball (DCB) + Bifurcated Gaussian (BG))	
μ_{BG}	443
$\sigma_{BG,L}$	15.9
$\sigma_{BG,R}$	4.89 ± 0.02
μ_{DCB}	439
$\sigma_{DCB,1}$	23.0
$\sigma_{DCB,2}$	6.91 ± 0.15
$\alpha_{DCB,1}$	-3.0
$\alpha_{DCB,2}$	7.6
n_{DCB}	1.0

$K^\pm \to \pi^\pm \mu^+ \mu^-$ using the Long track events from the 3.3 fb^{-1} collected by LHCb between 2016–2017 of:

$$\mathcal{B}(K^\pm \to \pi^\pm \mu^+ \mu^-) = (6.3 \pm 1.3_{stat} \pm 2.6_{sys}) \times 10^{-8} \qquad (4.47)$$

was obtained, a value which is compatible with the PDG average given in Equation 4.20.

Chapter 5

Charmed B Meson Physics at LHCb

5.1 Introduction

The LHCb detector was primarily designed for investigating matter-antimatter asymmetry through observation of CP violation in the neutral B^0 meson sector. These particles are heavier than kaons containing as their constituents a $b\bar{d}$ quark-antiquark pair. In addition to these measurements analyses have been performed to determine to high precision the CKM angle β, an angle of one of the unitary triangles mentioned in section 2.5, as part of new physics searches. The two flavour eigenstates of B^0 and $\bar{B}^0$ are the superposition of two mass eigenstates, B_L and B_H respectively, and it is the mass difference between these Δm that drives the oscillation between the particle and anti-particle in B mixing. The phase of these oscillations is proportional to β. The charged counterparts to the neutral B mesons are the $B^\pm$, which are well understood in terms of branching ratio, numerous measurements being performed for the various at B-factories such as LHCb and Belle II. Analogous to these are the B_c mesons which consist of a $\bar{b}$ and a c quark pair, and were first discovered [96] in 1998 at the CDF experiment through the channel $B_c^+ \to J/\psi\, \ell^+ \nu_e l$. Lifetime

measurements were subsequently performed by the D0 [97] and CDF [98] collaborations at the Tevatron, and the LHCb [99] and CMS [100] collaborations at the LHC. The discovery of the B_c^+ marked the finding of the last pseudoscalar meson as predicted by the Standard Model. Measurement of the B_c^+ lifetime by these collaborations matched theoretical prediction, the presence of the charm quark leading to a shorter lifetime than the B meson.

Proposals for the study of B_c^+ mesons at LHCb at Run 1 estimated that around $\times 10^9$ would be produced within the LHCb geometric acceptance per year of data taking, at a total instantaneous luminosity of $\mathcal{L} = 10^{32}\,\mathrm{cm^{-2}\,s^{-1}}$ [101], showing good prospects for the measurement of these particles at a collider experiment and motivating studies of as yet unmeasured channels.

5.1.1   Analysis into $B_c^\pm \to \phi K^\pm$

The branching fraction of the non-leptonic decay $B_c^\pm \to \phi K^\pm$ has not previously been measured. As the LHCb detector is designed for measurement of exclusive decays, studies of processes like this allow the predictions of the Standard Model to be tested.

The theoretical prediction for the branching fraction of this decay is postulated via perturbative Quantum Chromodynamics (pQCD) factorisation [102].

The availability of a measured branching fraction for the analogous decay $B^\pm \to \phi K^\pm$:

$$\mathcal{B}(B^\pm \to \phi K^\pm) = \left(8.8^{+0.7}_{-0.6}\right) \times 10^{-6}, \tag{5.1}$$

makes it an appropriate normalisation channel for analysis of the rarer B_c^+ decay. Using data and simulation the efficiencies are compared as a ratio and give the single event sensitivity of LHCb, $\alpha_{B_c^\pm \phi K}$, to the decay. The expression is deduced

by equating the integrated luminosity terms in the two equations for obtaining $B_c^\pm \to \phi K^\pm$ and $B^\pm \to \phi K^\pm$ yields:

$$N_{B_x^+} = \mathcal{L}\sigma\epsilon\mathcal{B}(B_x^+ \to \phi K^+)$$

$$\frac{N_{B^\pm\phi K}}{\epsilon_{B^\pm\phi K}\sigma(B^+)\mathcal{B}(B^\pm \to \phi K^\pm)} = \frac{N_{B_c^\pm\phi K}}{\epsilon_{B_c^\pm\phi K}\sigma(B_c^+)\mathcal{B}(B_c^\pm \to \phi K^\pm)}.$$

$$\alpha_{B_c^\pm\phi K} = \frac{\mathcal{B}(B_c^\pm \to \phi K^\pm)}{N_{B_c^\pm\phi K}}$$

$$\alpha_{B_c^\pm\phi K} = \frac{1}{N_{B^\pm\phi K}}\frac{\sigma(B^+)}{\sigma(B_c^+)}\frac{\epsilon_{B^\pm\phi K}}{\epsilon_{B_c^\pm\phi K}}\mathcal{B}\left(B^\pm \to \phi K^\pm\right) \qquad (5.2)$$

Compared to $B^\pm \to \phi K^\pm$, $B_c^\pm \to \phi K^\pm$ is more heavily suppressed within the Standard Model. Referring to the Feynman diagrams as shown in Figure 5.1, the normalisation channel can occur through the strong force via a penguin mechanism which makes it only singly Cabibbo suppressed, as the first conversion within the loop can be a $b \to t$ transition, and the second a $t \to s$. However the rarer channel is only possible through the conversion of two quarks into a $W^\pm$ boson, with this mechanism being doubly Cabibbo suppressed. A rough comparison in magnitude is given by the CKM matrix elements for both decays:

$$\left(\frac{|V_{tb}|\,|V_{ts}|}{|V_{cb}|\,|V_{us}|}\right)^2 \sim 20, \qquad (5.3)$$

this combined with the lower production cross section of B_c^+ mesons leads to a significant difference in magnitude between the two branching ratios of ~ 100.
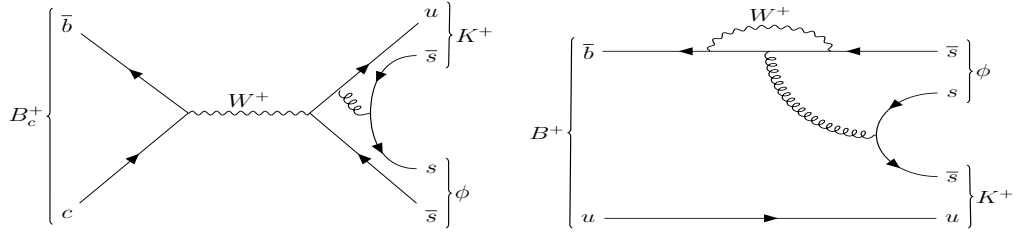
Figure 5.1: Examples of lowest order Feynman diagrams for $B_c^\pm \to \phi K^\pm$ and $B^\pm \to \phi K^\pm$ decays.

5.1.2   Theoretical Prediction for Branching Ratio

As the channel of $B_c^\pm \to \phi K^\pm$ has yet to be measured a prediction for the branching ratio of this decay was made using available results from B physics. The ratio of:

$$R = \frac{\sigma_{B_c^+}\mathcal{B}(B_c^+ \to J/\psi\,\pi^\pm)}{\sigma_{B^+}\mathcal{B}(B^+ \to J/\psi\,K^\pm)} \tag{5.4}$$

has been measured at LHCb [103] to be a value of $(0.61 \pm 0.12)\%$, when combined with the average measurement for $B^+ \to J/\psi\,K^\pm$ from the PDG [12]:

$$\mathcal{B}(B^+ \to J/\psi\,K^\pm) = (1.010 \pm 0.029) \times 10^{-3}, \tag{5.5}$$

and branching fraction predictions obtained from various theoretical models, which combined give a possible range of [104]:

$$\mathcal{B}(B_c^+ \to J/\psi\,\pi^\pm) = [0.34, 2.9] \times 10^{-3}, \tag{5.6}$$

an estimation can be made for the ratio of cross-sections of:

$$\sigma(B_c^+)/\sigma(B^+) = [0.21, 1.81]\% \tag{5.7}$$

which shows numerically the rarity of B_c^+ production over B^+.

The technique of perturbative QCD (pQCD) factorisation has allowed theorists to

predict the branching fraction of many B_c^+ two-body decays [102]. pQCD is the application of perturbation theory within the domain of QCD, taking advantage of the fact that the strong coupling constant, α_s, is small at both low energies and short range interactions. Among these predictions is an estimate for $B_c^\pm \to \phi K^\pm$:

$$\mathcal{B}(B_c^\pm \to \phi K^\pm) = (5.6^{+1.1}_{-0.0}(m_c) \ ^{+1.2}_{-0.9}(a_i) \ ^{+0.3}_{-0.0}(m_0)) \times 10^{-8}, \tag{5.8}$$

with the most dominant error on this value being from the mass of the charm quark, m_c, chiral enhancement factors, m_0, and the Gegenbauer moments, a_i, of the amplitudes from the meson distribution, where these moments are orthogonal Jacobi polynomials $P_n^{\alpha,\beta}(x)$ of the form [105]:

$$P_n^{(\lambda)}(x) = \frac{\Gamma\left(\lambda + \frac{1}{2}\right)}{\Gamma(2\lambda)} \frac{\Gamma(n + 2\lambda)}{\Gamma\left(n + \lambda + \frac{1}{2}\right)} P_n^{\alpha,\beta}(x), \tag{5.9}$$

with the special case that $\alpha = \beta = \lambda - \frac{1}{2}$, $\Gamma(x)$ being the Gamma function.

5.2   Analysis Procedure

With the availability of Run 1 and Run 2 data the objective for this analysis was to determine a branching ratio measurement for $B_c^\pm \to \phi K^\pm$ using the available statistics. However time limitations and awaiting the completion of MC requests for Run 2 instead an initial study to estimate the likely statistical yield that would be obtained in $B_c^\pm \to \phi K^\pm$ at Run 1 is presented. The MC statistics for Run 1 are given in Table 5.1.

Before unblinding of the analysis the capability of LHCb in measurement of the $B_c^\pm \to \phi K^\pm$ decay is deduced by obtaining the single event sensitivity given in Equation 5.2, this is then extrapolated to form a prediction for the signal yield defined as a range

Table 5.1: Run 1 MC statistics processed for $B_c^\pm \to \phi K^\pm$ and $B^\pm \to \phi K^\pm$ after generation, digitisation and reconstruction.

	$B_c^\pm \to \phi K^\pm$		$B^\pm \to \phi K^\pm$	
	Up	Down	Up	Down
2011	5.3×10^5	5.1×10^5	1.8×10^5	2.5×10^5
2012	1.0×10^6	1.0×10^6	5.3×10^5	4.3×10^5

using the theory results outlined in subsection 5.1.2.

5.3   Selection of $B_c^\pm \to \phi K^\pm$ and $B^\pm \to \phi K^\pm$ Events

For both Run 1 and Run 2 data events were read from a stripping line which selects B meson decays to three kaons, `Bc2hhh_KKK_exclLine`, for both rare and normalisation channel, the threshold cuts are listed in Table 5.2.

Cuts are applied to:

- The transverse momentum $p_T(K^\pm)$ of the B_c^+ and the final state kaons, a lower limit being applied as the B_c^+ mesons have low longitudinal momentum decaying within the detector volume.

- The distance of closest approach (DOCA) between the kaons and the decay vertex of the B_c^+.

- Momentum of the kaons $p(K^\pm)$.

- Invariant mass of the three final state kaons M_{hhh}.

- Impact parameter χ^2 of the $K^\pm$ with respect to the B_c^+ decay vertex, $IP\chi^2PV(K^\pm)$.

- Reconstructed track fit χ^2/ndf of the $K^\pm$, Track $\chi^2/\mathrm{ndf}(K^\pm)$.

- χ^2 from fit of the B_c^+ primary vertex, $PV\chi^2(B_c^+)$.

- PID variable for probability of kaons being true kaons, ProbNNk($K^{\pm}$).

- Cosine of the angle between the momentum of the B_c^+ and he reconstructed momentum of the three kaons (DIRA).

- Probability of the reconstructed tracks of the kaons being due to ghosting within the detector, Track ProbGhost($K^{\pm}$).

Table 5.2: Selections applied within stripping to $B_c^{\pm} \to \phi K^{\pm}$ and $B^{\pm} \to \phi K^{\pm}$ data and MC

Bc2hhh_KKK_exclLine	
$p_T(K^{\pm}) > 300\,\text{MeV}$	$KK, K^{\pm}\text{DOCAMAX} < 0.2\text{mm}$
$p(K^{\pm}) > 2500\,\text{MeV}$	$M_{hhh} \in [5998, 6502]$ or $[5098, 5502]\,\text{MeV}$
$\text{IP}\chi^2\text{PV}(K^{\pm}) > 1$	$p_T(B_c^{\pm}) > 1000\,\text{MeV}$
Track $\chi^2/\text{ndf}(K^{\pm}) < 4.0$	$\text{PV}\chi^2(B_c^+) > 150$
ProbNNk($K^{\pm}$) > 0.2	DIRA>0.9999
Track ProbGhost($K^{\pm}$) < 0.5	

Although the stripping line is named for B_c^+ a single data tuple was constructed to contain the full phase space including both B_c^+ and B^+. As opposed to the conventional method for filling decay tuples (using a single decay descriptor matching the exact decay and reading particles from the stripping line), due to both channels sharing the same final state of $K^{\pm}K^+K^-$, a `FilterDecays` object is firstly created to perform the selection of each daughter particle. Within this candidate particles are passed through filters with the generic decay descriptor `[X -> K+ K- K+]CC`, the three kaon daughters being labelled d_1, d_2 and $d_{bachelor}$ respectively. The term 'bachelor' is used to describe the additional kaon which is produced directly as opposed to from the decay of the $\phi(1020)$ meson. To uniquely identify each daughter within the decay descriptor, the convention of assigning a ^ to the particle of interest is used. The particles are then obtained from the output container of the stripping line and are identified by these filters.

The particles labelled d_1 and d_2 are combined within a decay descriptor describing the decay of the $\phi(1020)$, `[phi(1020) -> K+ K-]cc`, which is in turn used as an

argument to then construct a composite object via the `CombineParticles` algorithm, part of the Gaudi framework. The algorithm aims to construct the mother particle to be compatible with the input daughter particles in terms of vertex parameters and four momenta. In addition a threshold is included within the pre-selection cuts and applied to both the mother and the combined daughters, ensuring they both have an absolute mass difference of 400 MeV when compared with the PDG average.

Finally for MC another CombineParticles instance is used to construct the full event chain and perform truth matching on the sample as confirmation that the particles have been identified correctly by the detector.

For this analysis mass regions are defined as cuts to be applied to the single dataset which separate the B_c^+ and B^+ channel samples, these cuts are summarised in Table 5.3. The combined stripping and selection efficiencies for both channels are given in Table 5.4 and obtained from MC. Included within the definition of the stripping line are cuts on `ProbNNk`, the PID variable for kaons. As this variable is not well modelled within MC these cuts are removed when obtaining the efficiencies, and are instead processed using PIDCorr.

Table 5.3: Mass cuts for $B_c^\pm \to \phi K^\pm$ and $B^\pm \to \phi K^\pm$ selection. These are combined with stripping selections to given the efficiencies in Table 5.4.

	$B_c^\pm \to \phi K^\pm$	$B^\pm \to \phi K^\pm$
Full	$M_{B_c^+} \in [6050, 6500]$ MeV	$M_{B^+} \in [5180, 5500]$ MeV
Blinded	$M_{B_c^+} \in [6050, 6200],\ [6350, 6500]$ MeV	-

Table 5.4: Combined stripping and selection efficiencies for 2011–2012 $B_c^\pm \to \phi K^\pm$ and $B^\pm \to \phi K^\pm$ Monte Carlo. The difference in efficiency between channels arises from the different lifetimes of the B^+ and B_c^+, the latter decaying more rapidly affecting the quality of vertex and track fits.

	$B_c^\pm \to \phi K^\pm$	$B^\pm \to \phi K^\pm$
$\epsilon_{strip\cdot sel,2011}$	0.0630 ± 0.0002	0.1606 ± 0.0006
$\epsilon_{strip\cdot sel,2012}$	0.0585 ± 0.0002	0.1489 ± 0.0004

5.3.1 Acceptance Efficiencies

The generation efficiencies obtained from GAUSS are used to determine the fraction of events which fall within the LHCb acceptance. These are given in Table 5.5 and show similar acceptance for $B_c^\pm \to \phi K^\pm$ and $B^\pm \to \phi K^\pm$ of $\sim 20\%$.

Table 5.5: Generation level cut efficiencies for 2011–2012 $B_c^\pm \to \phi K^\pm$ and $B^\pm \to \phi K^\pm$ Monte Carlo.

	$B_c^\pm \to \phi K^\pm$	$B^\pm \to \phi K^\pm$
$\epsilon_{gen,2011}$	0.1615 ± 0.0004	0.1881 ± 0.0024
$\epsilon_{gen,2012}$	0.1579 ± 0.0004	0.1959 ± 0.0008

When cuts are applied to constrain the $\phi(1020)$ resonance for the purpose of classifier training, there is a significant loss in the available statistics. As a result the classifier quality is low making any threshold cuts applied to the resulting BDT variable give rise to a poor efficiency on the signal. Combined with the fact that background levels are already low within $B_c^\pm \to \phi K^\pm$ and $B^\pm \to \phi K^\pm$ the decision was therefore made to use only rectangular invariant mass cuts prior to fitting.

5.3.2 Triggering

Before the L0 trigger efficiency is obtained, efficiencies due to the Global Event Cut (GEC) are found by monitoring the number of events before and after the trigger line selection has been made. The distribution for the number of SPD hits is shown for both 2012 sWeighted data and MC in Figure 5.2. From this comparison the mismodelling of MC for this variable is made obvious and must be accounted for when determining the GEC efficiency. For Run 1, this efficiency is determined by the fraction of events passing the nSPDHits < 600 cut. These efficiencies have been obtained by scaling the SPD hit distribution for MC by a factor of 2 across the hit axis to match the data. This factor is discussed further in subsection 5.7.2. The resulting efficiencies are given in Table 5.6. The results for $B_c^\pm \to \phi K^\pm$ and

$B^\pm \to \phi K^\pm$ are comparable and so the ratio of the GEC efficiencies in the calculation of SES has been approximated to 1 for each year.
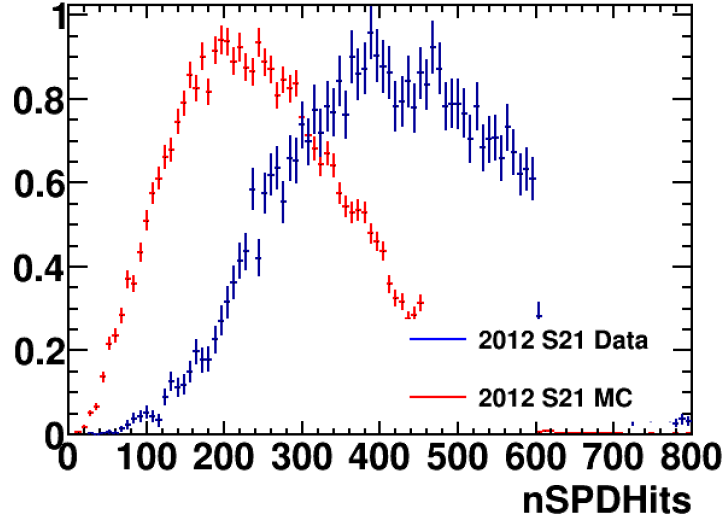
Figure 5.2: Comparison between 2012 sWeighted Data and MC for the number of SPD Hits in $B^\pm \to \phi K^\pm$.

Table 5.6: The efficiencies due to the GECs applied to 2011 and 2012 data before the L0 trigger obtained from MC.

	$B_c^\pm \to \phi K^\pm$	$B^\pm \to \phi K^\pm$
$\epsilon_{GEC,2011}$	0.871 ± 0.002	0.831 ± 0.002
$\epsilon_{GEC,2012}$	0.798 ± 0.002	0.739 ± 0.002

As they share the same final state the same trigger selection has been applied to $B_c^\pm \to \phi K^\pm$ and $B^\pm \to \phi K^\pm$. The requirement for L0 is that either the hadronic line be passed as triggered on signal (TOS), or that the event be triggered across any L0 line but on the rest of the event (TIS). In this case the trigger efficiency is evaluated as the following:

$$\epsilon_{trig}^{\text{L0}} = \frac{N_{TIS|Sel}}{N_{Sel}} + \frac{N_{\text{L0HadronTOS}|Sel}}{N_{Sel}} - \frac{N_{\text{L0HadronTISTOS}|Sel}}{N_{Sel}}$$

$$\epsilon_{trig}^{\text{L0}} = \epsilon_{\text{L0}}^{TIS} + \frac{N_{\text{L0Hadron,TOS\&!TIS}|Sel}}{N_{Sel}}$$

where $N_{TIS|Sel}$, $N_{L0HadronTOS|Sel}$, $N_{\text{L0HadronTISTOS}|Sel}$ and $N_{\text{L0Hadron,TOS\&!TIS}|Sel}$ are the number of TIS events, the number of events passing the hadronic line that are TOS,

TISTOS and TOS but not TIS respectively.

Using relation in Equation 3.6 the TIS efficiency can be determined from the overlap between TIS and TOS. To obtain an expression independent of N_{Sel} (the total number of events before triggering), an unknown in data, the formula for the TISTOS method Equation 3.7 is re-arranged and substituted in:

$$\epsilon_{trig}^{\text{L0}} = \frac{N_{TISTOS|Sel}}{N_{TOS|Sel}} \left(1 + \frac{N_{\text{L0Hadron,TOS\&!TIS|Sel}}}{N_{TIS|Sel}} \right), \qquad (5.10)$$

giving the L0 efficiency in terms of measurable quantities for $B^{\pm} \to \phi K^{\pm}$, labelled in this analysis as a *Trigger Exclusive* method. Given that the TISTOS method is an acceptable technique for determining trigger efficiency across LHCb analyses, and that it takes into account phase space dependency when performed binned, a test was performed to determine whether the ratio $\left(\epsilon_{B_c^+ \phi K} / \epsilon_{B^+ \phi K} \right)_{trig,\text{L0}}$ is equivalent between Equation 5.10 and Equation 3.7. The test was performed unbinned on MC giving the results in Table 5.7 and the efficiency ratios showing agreement to within 0.2%. The decision was therefore made to use the binned TISTOS method.

Table 5.7: Comparison of the L0 trigger efficiency ratio R_{L0} between $B^{\pm} \to \phi K^{\pm}$ and $B_c^{\pm} \to \phi K^{\pm}$ using an unbinned TISTOS method and the Trigger Exclusive method on MC.

	TISTOS	TrigExcl
$\epsilon_{\text{L0,2011}}^{B_c^+}$	0.624 ± 0.016	0.654 ± 0.015
$\epsilon_{\text{L0,2011}}^{B^+}$	0.627 ± 0.015	0.658 ± 0.014
$R_{\text{L0,2011}}$	0.995 ± 0.035	0.994 ± 0.031
$\epsilon_{\text{L0,2012}}^{B_c^+}$	0.589 ± 0.012	0.613 ± 0.011
$\epsilon_{\text{L0,2012}}^{B^+}$	0.599 ± 0.010	0.624 ± 0.010
$R_{\text{L0,2012}}$	0.983 ± 0.026	0.983 ± 0.023

In the case of $B_c^{\pm} \to \phi K^{\pm}$ the absence of a signal yield as predicted from the theoretical branching fraction (see Table 5.14), and the lack of any proxy to represent the signal, meant the L0 efficiency had to be estimated. This is performed under the assumption that the difference between the efficiency from data, and the same

efficiency as measured using MC for $B^{\pm} \to \phi K^{\pm}$ is the same for $B_c^{\pm} \to \phi K^{\pm}$, i.e.:

$$\epsilon_{\text{L0},Data}^{B_c^+\phi K} \sim \frac{\epsilon_{\text{L0},Data}^{B^+}}{\epsilon_{\text{L0},MC}^{B^+}} \epsilon_{\text{L0},MC}^{B_c^+}. \tag{5.11}$$

As $B_c^{\pm} \to \phi K^{\pm}$ and $B^{\pm} \to \phi K^{\pm}$ share the same final state particles of a real ϕ and a real K we expect the PID for both to be the same due to identical modelling. The efficiencies are calculated using a binned TISTOS method and are given in Table 5.9.

Samples of 2011 and 2012 Run 1 MC are used to determine the higher level trigger (HLT) effiencies for $B_c^{\pm} \to \phi K^{\pm}$ and $B^{\pm} \to \phi K^{\pm}$, comparing the number of truth-matched MC events before and after selection on the lines within the corresponding signal mass window. These efficiencies are given in Table 5.10 and Table 5.11. A full summary of all the trigger lines used within this analysis is given in Table 5.8. The HLT2 lines chosen for this analysis select on two or three body decays using the weights collected via a BDT multivariate classifier trained by the HLT group within the collaboration prior to data taking.

Table 5.8: Trigger lines for analysis into the Run 1 data.

L0	Hadron TOS
	Global TIS
HLT1	TrackAllL0 TOS
HLT2	Topo2BodyBBDT TOS
	Topo3BodyBBDT TOS

Table 5.9: L0 binned TISTOS efficiencies using 2011–2017 $B^{\pm} \to \phi K^{\pm}$ Data with the estimates for 2011 and 2012 $B_c^{\pm} \to \phi K^{\pm}$ calculated under the assumption given in Equation 5.11. Results are compared, where appropriate, with the same method applied to 2011 and 2012 MC.

	$B^{\pm} \to \phi K^{\pm}$		$B_c^{\pm} \to \phi K^{\pm}$	
	Data	MC	Data (Estimated)	MC
$\epsilon_{L0,Data,2011}$	0.475 ± 0.020	0.516 ± 0.011	0.433 ± 0.023	0.471 ± 0.012
$\epsilon_{L0,Data,2012}$	0.513 ± 0.012	0.469 ± 0.009	0.477 ± 0.018	0.437 ± 0.010
$\epsilon_{L0,Data,2015}$	0.494 ± 0.016	-	-	-
$\epsilon_{L0,Data,2016}$	0.532 ± 0.006	-	-	-
$\epsilon_{L0,Data,2017}$	0.519 ± 0.006	-	-	-

Table 5.10: HLT1 Level trigger cuts for 2011–2012 $B_c^\pm \to \phi K^\pm$ and $B^\pm \to \phi K^\pm$ Monte Carlo.

	$B_c^\pm \to \phi K^\pm$	$B^\pm \to \phi K^\pm$
$\epsilon_{HLT1,2011}$	0.756 ± 0.004	0.803 ± 0.003
$\epsilon_{HLT1,2012}$	0.756 ± 0.003	0.805 ± 0.002

Table 5.11: HLT2 Level trigger cuts for 2011–2012 $B_c^\pm \to \phi K^\pm$ and $B^\pm \to \phi K^\pm$ Monte Carlo.

	$B_c^\pm \to \phi K^\pm$	$B^\pm \to \phi K^\pm$
$\epsilon_{HLT2,2011}$	0.768 ± 0.004	0.858 ± 0.003
$\epsilon_{HLT2,2012}$	0.829 ± 0.003	0.927 ± 0.002

5.3.3   Removal of Multiple Candidates and PID Efficiency

The decays of $B_c^\pm \to \phi K^\pm$ and $B^\pm \to \phi K^\pm$ are triggered either on $K^\pm \phi$ as signal, or the remainder of the event which in this case is a 3-body state $K^\pm K^+ K^-$ due to the extremely short lifetime of the ϕ resonance. As this final state contains two identical particles the probability of the event being selected above once is significant at around 50%, with the possibility of any pair of opposite sign kaons being candidates to be the daughters of the ϕ as illustrated in Figure 5.3. To ensure
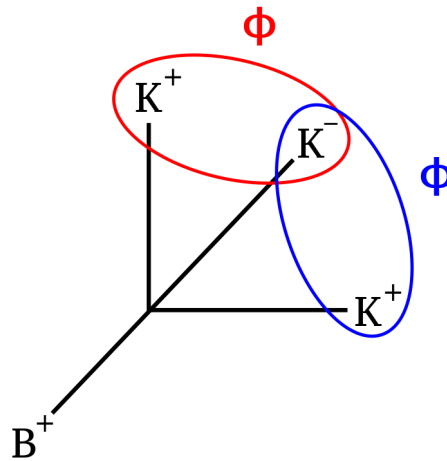
Figure 5.3: The issue of multiple candidates from the decay of $\phi \to K^+ K^-$ in $B_c^\pm \to \phi K^\pm$ and $B^\pm \to \phi K^\pm$.

only a single candidate is used for each event the data is read into a dataframe which

stores the variables from a ROOT TTree as a manipulatable python object, using the *Pandas* library [106], which can be accessed by index and sliced. Contained within the methods for this object is `drop_duplicates`, which is used on the variables of 'eventNumber' and 'runNumber' to remove these multiple candidates. Within the algorithm a duplicate is chosen at random within the dataframe for each combination of event and run number, the others then being removed. For ease the efficiency associated with this process is combined with the PID efficiencies from cut to kaons on the stripping line in Table 5.12 after the MC has been corrected using PIDCorr. Although not demonstrated here due to lack of a signal, systematical uncertainty for PID would be determined by varying the binning of the kinematic variables used to correct the MC (as demonstrated in section 4.2.10). This overall efficiency is therefore defined as:

$$\epsilon_{PID} \cdot \epsilon'_{multi} = \frac{N_{single|strip}}{N'_{strip}} \frac{N_{PID|single}}{N_{single|strip}} \tag{5.12}$$

where N'_{strip} is the number of events obtained from stripping without the PID cut in place, $N_{single|strip}$ is the number of events after removal of multiple candidates, and $N_{PID|single}$ is the number of events after the PID cut has been applied.

Table 5.12: Combined efficiency for the PID cut in the stripping line obtained by correcting the MC using PIDCorr, and the rejection of multiple candidates for 2011–2012 $B_c^\pm \to \phi K^\pm$ and $B^\pm \to \phi K^\pm$ Monte Carlo. The uncertainties are due to the available statistics.

	$B_c^\pm \to \phi K^\pm$	$B^\pm \to \phi K^\pm$
$\epsilon_{PID} \cdot \epsilon'_{multi,2011}$	0.403 ± 0.002	0.404 ± 0.002
$\epsilon_{PID} \cdot \epsilon'_{multi,2012}$	0.399 ± 0.001	0.402 ± 0.001

5.4   Validation of Monte Carlo Samples

The MC samples for 2011 and 2012 Stripping21 were validated using the sWeighting technique for $B^\pm \to \phi K^\pm$. The data samples were fitted and the yields for signal and background used to determine weights which could then be applied to the sample to represent signal only distributions in particular variables. These could then be compared to MC when L0 and Hlt1 cuts had been applied. Comparisons for transverse momentum, impact parameter χ^2 and the cosine of the DIRA angle defined as the angle between the B^+ momentum and combined daughter momenta are shown in Figure 5.4 as characteristic kinematic variables which are also used within selection. The plots show good level of agreement modelling the variables to an acceptable degree of accuracy.

5.5   Fitting Data

The normalisation channel of $B^\pm \to \phi K^\pm$ is fitted using a function consisting of two Ipatia PDFs [95] to model the signal peak and a Chebychev polynomial as a model of the combinatorial background. In the overall fit an acceptable quality was found when the background was modelled using a first order polynomial. The fits for the years 2011–2017 are performed using an unbinned maximum likelihood fit and are shown in Figure 5.5 and the yields summarised in Table 5.13.

Table 5.13: Yields for $B^\pm \to \phi K^\pm$ in 2011–2017 Data.

	$N_{B^+\phi K}$
2011	8322 ± 114
2012	18944 ± 174
2015	5838 ± 92
2016	37591 ± 274
2017	39941 ± 274

(a) 2011 S21 B^+ transverse momentum

(b) 2012 S21 B^+ transverse momentum

(c) 2011 S21 B^+ impact parameter χ^2

(d) 2012 S21 B^+ impact parameter χ^2

(e) 2011 S21 B^+ DIRA

(f) 2012 S21 B^+ DIRA
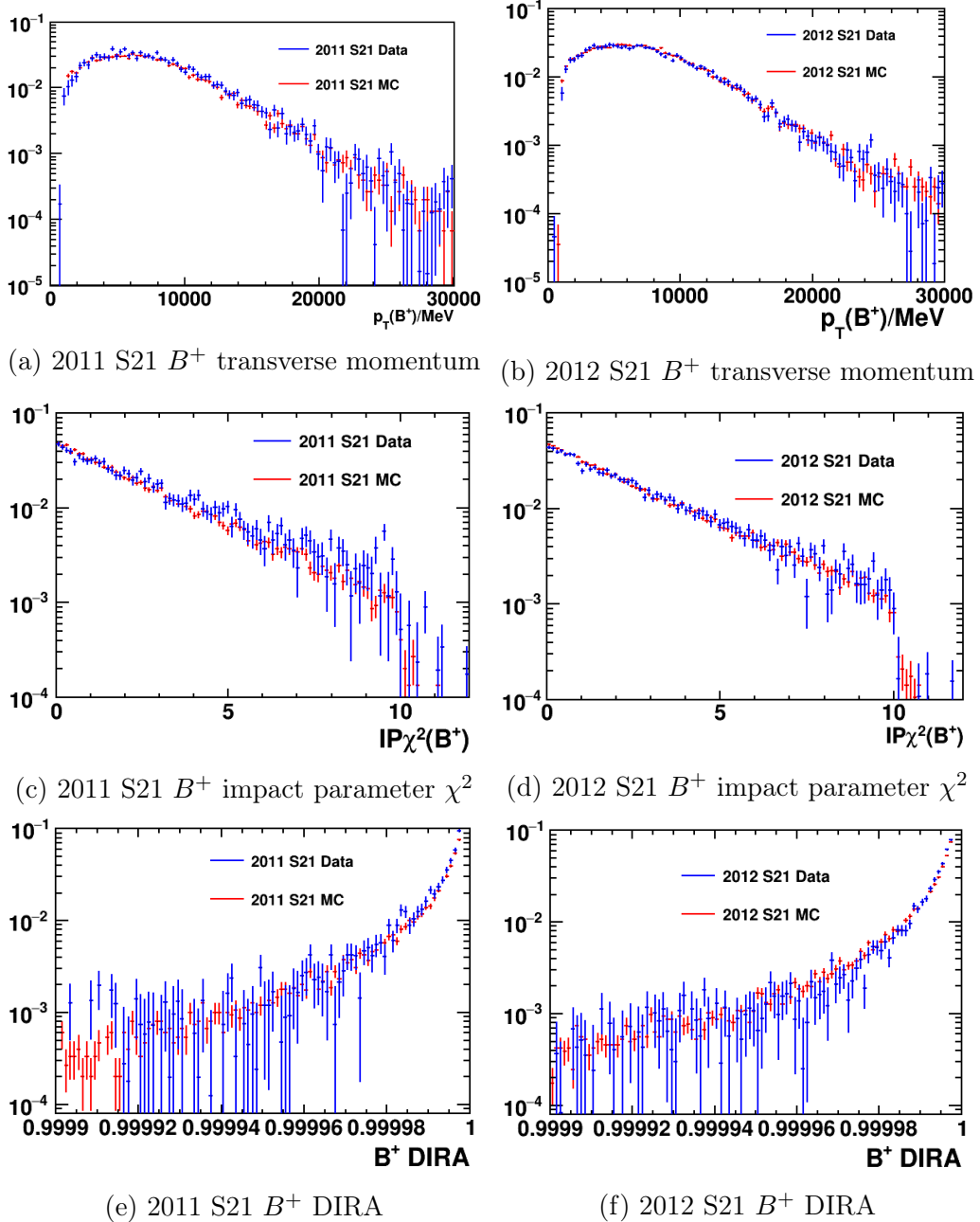
Figure 5.4: Comparisons of select kinematic variables between data after sWeighting has been applied and MC for 2011 and 2012 data, with MC being normalised to data.

(a) 2011 Stripping21

(b) 2012 Stripping21

(c) 2015 Stripping24

(d) 2016 Stripping28r1

(e) 2017 Stripping29r2
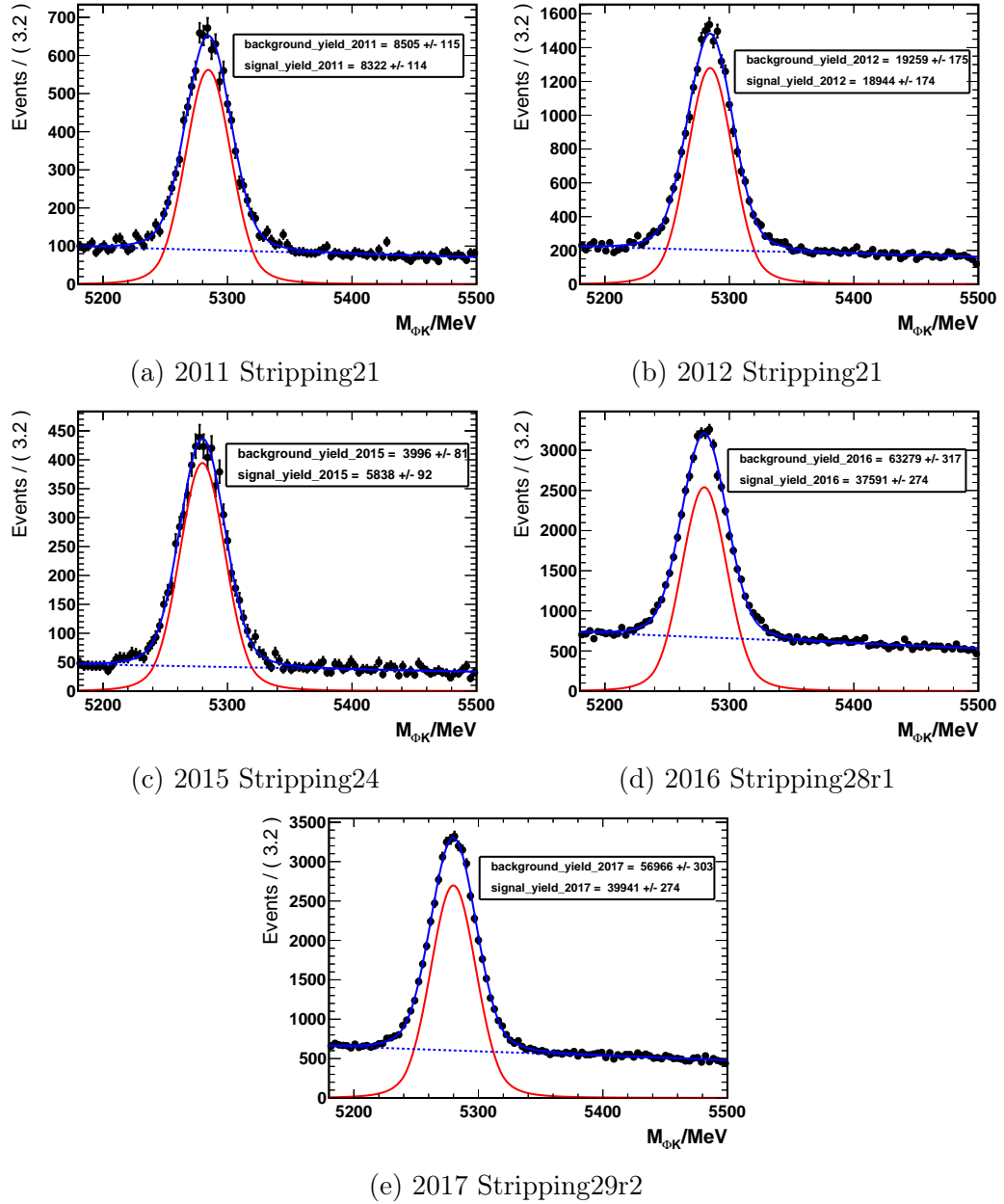
Figure 5.5: Fits performed on the invariant mass distributions for $B^{\pm} \to \phi K^{\pm}$ between 2011–2017, background is modelled using a linear function and the signal consists of a double Ipatia function.

5.6   Predictions During Blinding

After fitting of $B^{\pm} \to \phi K^{\pm}$ and $B_c^{\pm} \to \phi K^{\pm}$ the single event sensitivities for the years 2011 and 2012 were obtained. From these using the predicted branching ratio of $B_c^{\pm} \to \phi K^{\pm}$ from the theory given in Equation 5.8, and the predictions for the ratio of cross sections between B^+ and B_c^+ given in Equation 5.7, an estimate of signal yield for each year was calculated. The results are given in Table 5.14.

Table 5.14: Values for single event sensitivity multiplied by the cross-section ratio, $\alpha_{\phi K} \frac{\sigma(B_c^+)}{\sigma(B^+)}$, the number of background events within the signal region, N_{Bkg}, the predicted signal yield, $N^{pred}_{B_c^+ \phi K^+}$ and predicted signal significance. The predictions for signal and significance are made using the highest and lowest theoretical branching ratios for $B_c^{\pm} \to \phi K^{\pm}$ from Z. Rui et. al. (2014) [104].

	$\alpha_{\phi K} \frac{\sigma(B_c^+)}{\sigma(B^+)}/10^{-9}$	N_{Bkg}	$N^{pred}_{B_c^+ \phi K^+}/10^{-2}$	$\frac{N_S}{\sqrt{N_S+N_B}}/10^{-2}$
2011	4.10 ± 0.37	4933 ± 70	$[3 \pm 1, 25 \pm 9]$	$[4.1 \pm 1.5, 35.2 \pm 12.9]$
2012	1.89 ± 0.16	11365 ± 106	$[6 \pm 2, 54 \pm 20]$	$[5.9 \pm 2.2, 50.2 \pm 18.3]$

5.7   Systematics for $B_c^{\pm} \to \phi K^{\pm}$

To obtain a threshold on the $B_c^{\pm} \to \phi K^{\pm}$ branching ratio a prediction for the cross-section ratio with $B^{\pm} \to \phi K^{\pm}$ is required. The use of theory and prior LHCb measurements as stated in subsection 5.1.2 introduces a number of uncertainties which are included as systematics within the analysis and are among those outlined in Table 5.15. The most dominant contribution to the systematics of this analysis comes from the uncertainty on the ratio in Equation 5.4.

Additional systematics which would be considered in a complete analysis include uncertainties to account for the efficiency assumptions made during the course of the analysis, including accounting for any systematic effects due to kinematical differences between B_c^+ and B^+, and the influence of the different characteristic

Table 5.15:   Dominant sources of systematic uncertainty considered in the measurement of threshold for $B_c^\pm \rightarrow \phi K^\pm$ branching fraction expressed as percentages.

Type	Uncertainty Component/%	
	2011	2012
MC Trigger Modelling	9	9
Modelling of GEC Efficiency	7	9
GEC Efficiency for B_c^+ vs B^+	4	6
MC Sample Size	1.9	1.0
Precision of LHCb R Measurement [103]	20	20
Precision of Known $B^\pm \rightarrow \phi K^\pm$ Branching Fraction [12]	8	8
Precision of Known $B^+ \rightarrow J/\Psi K^\pm$ Branching Fraction [12]	2.9	2.9

cuts applied to each.

Choice of Model to Describe Signal

Prior to unblinding the effect of switching the models describing the signal distribution was also studied with the fits to both rare and normalisation channels being repeated using a double Crystal Ball function. The results are given in Table 5.16 and are compared with Table 5.14. Observing no significant effect in the single event sensitivity, no systematic was assigned.

Table 5.16: Ratio values for 2011–2012 Data using alternative signal model of a Double Crystal Ball, columns as for Table 5.14.

	$\alpha_{\phi K}\frac{\sigma(B_c^+)}{\sigma(B^+)}/10^{-9}$	N_{Bkg}	$N_{B_c^+\phi K^+}^{pred}/10^{-2}$	$\frac{N_S}{\sqrt{N_S+N_B}}/10^{-2}$
2011	3.75 ± 0.37	4896 ± 76	$[3 \pm 1, 27 \pm 10]$	$[4.5 \pm 1.7, 38.5 \pm 14.2]$
2012	1.52 ± 0.13	11317 ± 119	$[8 \pm 3, 67 \pm 24]$	$[7.3 \pm 2.7, 62.5 \pm 22.8]$

5.7.1   Trigger Modelling in Monte Carlo

With the trigger efficiencies being calculated using MC samples beyond the L0 trigger level, a comparison was made between performance of the TISTOS method on data and the 2011 and 2012 MC samples (see Table 5.9). The difference between

the two efficiency values obtained is assigned as the respective systematic for modelling of the trigger.

5.7.2   Modelling of Global Event Cuts in Monte Carlo

When the distributions for the number of SPD hits in $B_c^\pm \to \phi K^\pm$ and $B^\pm \to \phi K^\pm$ are compared, as shown in Figure 5.6, an incompatibility is observed in the width and position of the maximum, giving rise to the differing efficiencies shown in Table 5.6. The cause for this difference could be due to the underlying physics, or due to mismodelling in MC. Therefore the difference in efficiency between $B_c^\pm \to \phi K^\pm$ and $B^\pm \to \phi K^\pm$ has been assigned as a systematic.
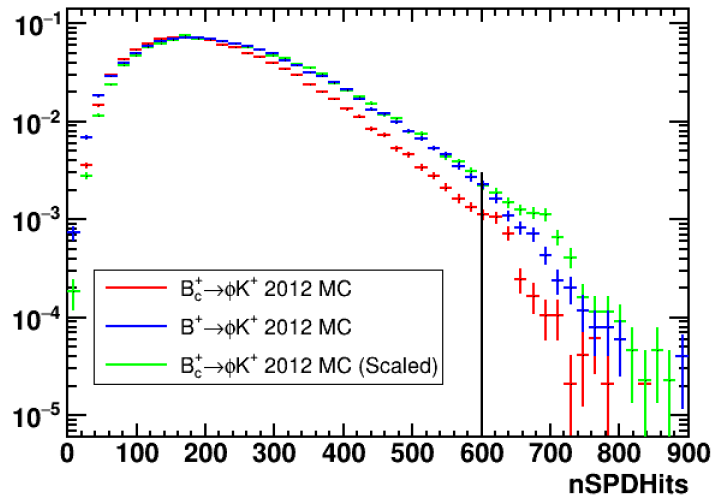
Figure 5.6: Distributions of the SPD hit multiplicity in 2012 $B_c^\pm \to \phi K^\pm$ and $B^\pm \to \phi K^\pm$ MC showing the compatibility between the two distributions after $B_c^\pm \to \phi K^\pm$ has been scaled.

Furthermore the level of precision in determining the factor of 2, which maps the nSPDHit distribution from MC to data, has been investigated. The exact locations of each maximum within the two distributions in Figure 5.2 can only be measured to within a set interval giving rise to an uncertainty on this factor of 12.5%. A systematic uncertainty for the GEC efficiency has been derived by noting its values

when the factor is set to its highest and lowest values within the 12.5% band.

5.8   Final Thresholds on $B_c^{\pm} \to \phi K^{\pm}$ Branching Ratio

With a maximum yield obtained from the ranges within the predictions being only a single event the data for 2011 and 2012 were unblinded and the full unbinned maximum likelihood fit performed. The fit parameters obtained from MC and data for $B_c^{\pm} \to \phi K^{\pm}$ are shown in Table 5.17. As can be seen in Figure 5.7 measurement is consistent with the prediction. For 2012 a negative fluctuation in statistics actually causes the fit model yield to instead appear negative.

Table 5.17: The fit parameters obtained from fitting to $B_c^{\pm} \to \phi K^{\pm}$ MC and final data which yielded no significant signal.

	2011	2012
	Background Polynomial	
p_1	-0.260 ± 0.025	-0.277 ± 0.016
	Signal Double Ipatia Function	
a_1	2.0	2.0
a_2	2.0	2.0
fb	0	0
l	-20	-20
μ	6278.6 ± 0.1	6778.5 ± 0.1
n_1	4.0	4.0
n_2	4.0	4.0
σ	18.60 ± 0.07	18.98 ± 0.05
ζ	0.005	0.005

In the results shown in Table 5.18, the final single event sensitivity (SES) for each year is used to give an estimate of the upper threshold for the $B_c^{\pm} \to \phi K^{\pm}$ branching ratio, i.e. the lowest branching ratio achievable by LHCb, at Run 1. The two independent measurements are then combined to give a value of:

$$\mathcal{B}(B_c^{\pm} \to \phi K^{\pm}) \lesssim (9 \pm 4_{sys} \pm 1_{stat}) \times 10^{-7}, \tag{5.13}$$

the uncertainties arising from the procedure to determine SES value.

Table 5.18: Individual $B_c^\pm \to \phi K^\pm$ branching ratios for 2011 and 2012

$\mathcal{B}\left(B_c^\pm \to \phi K^\pm\right) \lesssim$ x / 10^{-6}	
2011	$1.62 \pm 0.49_{sys} \pm 0.11_{stat}$
2012	$0.78 \pm 0.19_{sys} \pm 0.04_{stat}$
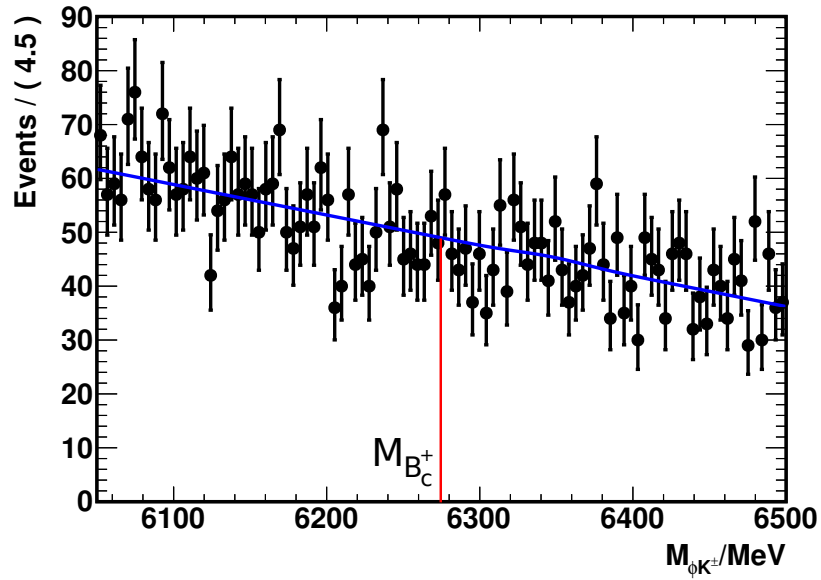
(a) 2011 Stripping 21 Data.
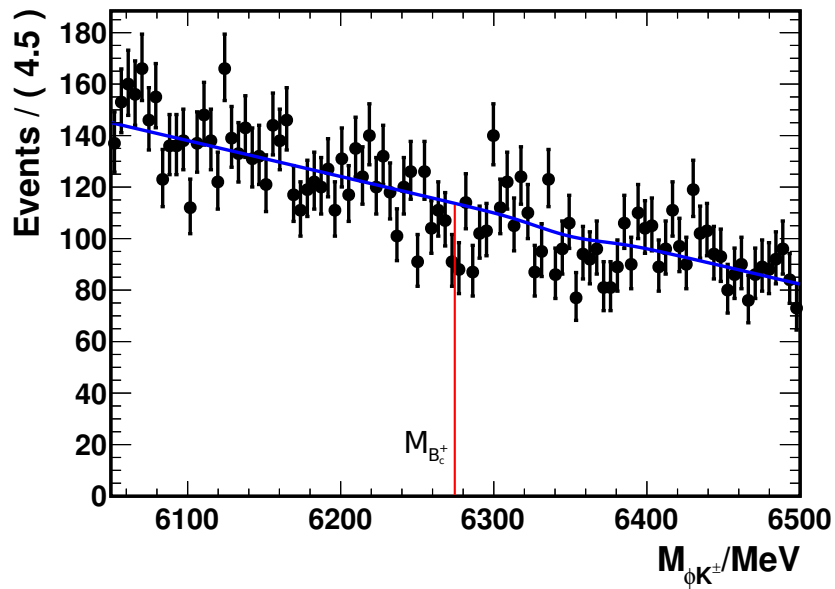
(b) 2012 Stripping 21 Data.

Figure 5.7: The final fits performed on 2011–2012 Stripping21 Run 1 data under the $B_c^\pm \to \phi K^\pm$ selection with removal of multiple candidates.

Chapter 6

Conclusions

This thesis presents studies to determine prospects for measuring the rare kaon decay channel $K^{\pm} \to \pi^{\pm} \mu^{+} \mu^{-}$ at the LHCb experiment, using 3.6 fb^{-1} Run 2 data recorded between 2015 and 2017 at a collision energy of 13 TeV, and measurement of the branching ratio for the decay $B_c^{\pm} \to \phi K^{\pm}$ using 3.2 fb^{-1} of data collected at 7 and 8 TeV.

This is the first observation of $K^{\pm} \to \pi^{\pm} \mu^{+} \mu^{-}$ performed at a collider experiment, with previous measurements having been made at fixed target experiments such as NA48/2. At present the LHCb data does not achieve the level of precision from current measurements [80]. With the anticipated improvements of the LHCb High Level Trigger, the measurements at LHCb could become more competitive. An improvement of $\mathcal{O}(10^4)$ in the statistics is predicted for each year of data taking at Run 3 [75].

Higher experimental precision will allow further constraints to be placed on models describing new physics through measurement of $K^{\pm} \to \pi^{\pm} \mu^{+} \mu^{-}$ testing for higher order loop contributions. As appropriate for an initial measurement, only decays

occurring within the VELO were considered. With the increased data to be recorded at Run 3, this could be expanded to include particle decays downstream of the VELO, increasing the accessible number of $K^\pm \to \pi^\pm \mu^+ \mu^-$ decays by a factor of ~ 10 (see discussion at start of section 4.2). A dedicated trigger line for the lepton flavour violating mode $K^\pm \to \pi^\mp \mu^+ \mu^+$ is already present in data which pushes the new physics search further, e.g. into the hunt for hypothetical heavy neutrinos, when the required level of sensitivity is reached.

In combination with other measurements (e.g. $\Sigma^+ \to p^+ \mu^+ \mu^-$ [107] and $K_s^0 \to \mu^+ \mu^-$ [20]) it is evident that LHCb is indeed capable of investigations into the strange sector beyond its original objective of being an apparatus for the precision measurement of b and c hadron decays and CP violation in the B sector.

A dedicated search for the exclusive final quasi-two body final state $B_c^\pm \to \phi K^\pm$ was performed using $B^\pm \to \phi K^\pm$ as a control mode. Efficient selections based on the control mode data and simulated signal decays were developed. Applying these to the 7 and 8 TeV data recorded between 2011 and 2012, no significant evidence for signal was observed. This non-observation with the resulting level of sensitivity determined by the methods employed, is consistent with theoretical expectation.

Bibliography

[1] Particle Data Group, *CKM Quark-Mixing Matrix*, Phys. Rev. D **98** (2018), no. January 030001, Section 12.1.

[2] ATLAS, G. Aad *et al.*, *Observation of a New Particle in the Search for the Standard Model Higgs Boson with the ATLAS Detector at the LHC*, Phys. Lett. **B716** (2012) 1, `arXiv:1207.7214`.

[3] CMS, S. Chatrchyan *et al.*, *Observation of a New Boson at a Mass of 125 GeV with the CMS Experiment at the LHC*, Phys. Lett. **B716** (2012) 30, `arXiv:1207.7235`.

[4] D. Griffiths, *Introduction to Elementary Particles*, Wiley-VCH, 1987.

[5] S. Prell, *CP Violation at BABAR and BELLE*, eConf **C0307282** (2003), TTH01.

[6] S. Bilenky, *The Standard Model of the Electroweak Interaction*, Lecture Notes in Physics **947** (2018), no. 2 35, `arXiv:0502010`.

[7] M. Tanabashi *et al.*, *Neutrino Masses, Mixing, and Oscillations*, Phys. Rev **D 98** (2018).

[8] H. Fritzsch, M. Gell-Mann, and H. Leutwyler, *Advantages of the Color Octet*

Gluon Picture, Phys. Lett. **47B** (1973) 365.

[9] T. Appelquist, M. Dine, and I. J. Muzinich, *The Static Potential in Quantum Chromodynamics*, Phys. Lett. **69B** (1977) 231.

[10] N. Cabibbo, *Unitary Symmetry and Leptonic Decays*, Physical Review Letters **10** (1963) 531.

[11] L. Maiani, *The GIM Mechanism: Origin, Predictions and Recent Uses*, `arXiv:1303.6154`, Rencontres de Moriond, EW Interactions and Unified Theories, La Thuile, Valle d'Aosta, Italia, 2-9 March, 2013.

[12] Particle Data Group, K. A. Olive *et al.*, *Review of Particle Physics*, Chin. Phys. **C38** (2014) 090001.

[13] SLAC-SP-017, J. E. Augustin *et al.*, *Discovery of a Narrow Resonance in e^+e^- Annihilation*, Phys. Rev. Lett. **33** (1974) 1406, [Adv. Exp. Phys.5,141(1976)].

[14] E598, J. J. Aubert *et al.*, *Experimental Observation of a Heavy Particle J*, Phys. Rev. Lett. **33** (1974) 1404.

[15] C. S. Wu *et al.*, *Experimental Test of Parity Conservation in Beta Decay*, Phys. Rev. **105** (1957) 1413.

[16] BaBar, B. Aubert *et al.*, *Observation of direct CP violation in $B^0 \rightarrow K^+\pi^-$ decays*, Phys. Rev. Lett. **93** (2004) 131801, `arXiv:hep-ex/0407057`.

[17] Belle, Y. Chao *et al.*, *Evidence for direct CP violation in B0 —> K+ pi-decays*, Phys. Rev. Lett. **93** (2004) 191802, `arXiv:hep-ex/0408100`.

[18] NA62, E. Cortina Gil *et al.*, *The Beam and detector of the NA62 experiment at CERN*, JINST **12** (2017), no. 05 P05025, `arXiv:1703.08501`.

[19] LHCb Collaboration, R. Aaij *et al.*, *Search for the Rare Decay $K_s^0 \to \mu^+\mu^-$*, Physics Letters, Section B: Nuclear, Elementary Particle and High-Energy Physics **725** (2013), no. 1-3 15, `arXiv:1209.4029`.

[20] LHCb Collaboration, R. Aaij *et al.*, *Improved Limit on the Branching Fraction of the Rare Decay $K_s^0 \to \mu^+\mu^-$*, `arXiv:1706.00758`.

[21] R. Lindner, *LHCb layout_2. LHCb schema_2*, LHCb-PHO-GENE-2008-002, Feb, 2008.

[22] LHCb Collaboration, R. Aaij *et al.*, *LHCb Detector Performance*, International Journal of Modern Physics A **30** (2015), no. 07 1530022, `arXiv:1412.6352`.

[23] LHCb collaboration, C. Elsässer, *$\bar{b}b$ production angle plots*, 2019. https://lhcb.web.cern.ch/lhcb/speakersbureau/html/bb_ProductionAngles.html.

[24] LHCb Collaboration, A. A. Alves *et al.*, *The LHCb Detector at the LHC*, JINST **3** (2008) S08005, LHCb-DP-2008-001. CERN-LHCb-DP-2008-001.

[25] M. Vesterinen, *Considerations on the LHCb dipole magnet polarity reversal*, Tech. Rep. LHCb-PUB-2014-006. CERN-LHCb-PUB-2014-006, CERN, Geneva, Apr, 2014. On behalf of the LHCb collaboration.

[26] M. G. Van Beuzekom, W. Vink, L. W. Wiggers, and M. Zupan, *Pile-up veto L0 trigger system for LHCb using large FPGA's*, .

[27] The LHCb VELO Group, *Performance of the LHCb Vertex Locator*, `arXiv:1405.7808v`.

[28] J. Libby, *VELO: The LHCb Vertex Detector*, Nuclear Instruments and Methods in Physics Research. Section A: Accelerators, Spectrometers, Detectors and Associated Equipment **494** (2002), no. 1 113 , Proceedings

of the 8th International Conference on Instrumentation for Colliding Beam Physics.

[29] S. Löchner and M. Schmelling, *The Beetle Reference Manual - chip version 1.3, 1.4 and 1.5*, Tech. Rep. LHCb-2005-105. CERN-LHCb-2005-105, CERN, Geneva, Nov, 2006.

[30] LHCb, M. Stahl, *Machine learning and parallelism in the reconstruction of LHCb and its upgrade*, J. Phys. Conf. Ser. **898** (2017), no. 4 042042, `arXiv:1710.08947`.

[31] Hamamatsu Photonics K. K. Editorial Committee, *Photomultiplier Tubes Basics and Applications*, Hamamatsu Photonics K.K. Electron Tube Division, 3 ed.

[32] P. Perret and X. Vilasis-Cardona, *Performance of the lhcb calorimeters during the period 2010-2012*, Journal of Physics: Conference Series **587** (2015) .

[33] K. Inami, *Cherenkov light imaging in particle and nuclear physics experiments*, Nuclear Instruments and Methods in Physics Research, Section A: Accelerators, Spectrometers, Detectors and Associated Equipment **876** (2017) 278.

[34] M. Sannino, S. Cuneo, and M. Ameri.

[35] F. Archilli *et al.*, *Performance of the Muon Identification at LHCb*, Journal of Instrumentation **8** (2013) .

[36] LHCb Collaboration, M. Clemencic *et al.*, *The LHCb Simulation Application, Gauss: Design, Evolution and Experience*, Journal of Physics: Conference Series **331** (2011), no. 3 032023.

[37] M. Clemencic *et al.*, *The LHCb Simulation Application, Gauss: Design, Evolution and Experience*, Journal of Physics: Conference Series **331** (2011), no. PART 3 .

[38] *LHCb Starterkit Lessons: Changes to the Data Flow in Run 2*, Jan, 2019. `https://lhcb.github.io/starterkit-lessons/starterkit-lessons.pdf`.

[39] LHCb Collaboration, LHCb Collaboration, *Trigger Schemes*, Jan, 2019. `http://lhcb.web.cern.ch/lhcb/speakersbureau/html/TriggerScheme.html`.

[40] LHCb, R. Aaij *et al.*, *Design and performance of the LHCb trigger and full real-time reconstruction in Run 2 of the LHC*, JINST **14** (2019), no. 04 P04013, `arXiv:1812.10790`.

[41] S. Tolk, J. Albrecht, F. Dettori, and A. Pellegrino, *Data Driven Trigger Efficiency Determination at LHCb*, Tech. Rep. LHCb-PUB-2014-039. CERN-LHCb-PUB-2014-039, CERN, Geneva, May, 2014.

[42] R. Aaij *et al.*, *The LHCb Trigger and its Performance in 2011*, JINST **8** (2013) P04022, `arXiv:1211.3055`.

[43] V. Gligorov *et al.*, *Swimming : A Data Driven Acceptance Correction Algorithm*, Journal of Physics Conference Series **396** (2012) 2016.

[44] M. Cattaneo, *User Guide*, BRUNEL LHCb Reconstruction Program (2000), Brunel v9r1.

[45] M. Gersabeck, *LHCb Tracking, Alignment and Physics Performance*, PoS **VERTEX2010** (2010) 014. 11 p, LHCb-PROC-2010-065.

[46] S. Benson *et al.*, *The LHCb Turbo Stream*, Journal of Physics: Conference Series **664** (2015), no. 8 082004.

[47] M. Adinolfi *et al.*, *Performance of the LHCb RICH detector at the LHC*, European Physical Journal C **73** (2013), no. 5 1.

[48] A. Poluektov, *Kernel Density Estimation of a Multidimensional Efficiency Profile*, `arXiv:1411.5528arXiv:1411.5528`.

[49] P. Golonka and Z. Was, *PHOTOS Monte Carlo: A Precision Tool for QED Corrections in Z and W Decays*, European Physical Journal C **45** (2006), no. 1 97, `arXiv:0506026`.

[50] A. Ryd *et al.*, *EvtGen A Monte Carlo Generator for B-Physics*, .

[51] C.-H. Chang, C. Driouichi, P. Eerola, and X.-G. Wu, *BCVEGPY: An Event Generator for Hadronic Production of the B_c Meson*, `arXiv:0309120arXiv:0309120`.

[52] D. Müller, M. Clemencic, G. Corti, and M. Gersabeck, *ReDecay: A Novel Approach to Speed up the Simulation at LHCb*, `arXiv:1810.10362arXiv:1810.10362`.

[53] H. Wenzel, J. Yarba, and A. Dotti, *The Geant4 Physics Validation Repository*, Journal of Physics: Conference Series **664** (2015), no. 6 .

[54] A. Heikkinen, N. Stepanov, and J. P. Wellisch, *Bertini intranuclear cascade implementation in GEANT4*, eConf **C0303241** (2003) MOMT008, `arXiv:nucl-th/0306008`.

[55] D. E. Jaffe, K. H. Lo, J. R. Comfort, and M. Sivertz, *Comparison of inclusive particle production in 14.6-GeV/c proton-nucleus collisions with simulation,*

Nucl. Instrum. Meth. **B246** (2006) 309, `arXiv:hep-ex/0511012`, [Erratum: Nucl. Instrum. Meth.B254,340(2007)].

[56] LHCb Collaboration, Ribon, A and others, *Status of Geant4 hadronic physics for the simulation of LHC experiments at the start of LHC physics program*, .

[57] G. Corti *et al.*, *How the Monte Carlo Production of a Wide Variety of Different Samples is Centrally Handled in the LHCb Experiment*, Journal of Physics: Conference Series **664** (2015), no. 7 2.

[58] Tabanashi, M and others (Particle Data Group), *Passage of Particles Through Matter*, Phys. Rev. D **98** (2019), no. January 030001, Section 12.1.

[59] B. R. Martin and G. Shaw, *Particle Physics*, John Wiley and Sons Ltd, 3 ed., 2008.

[60] Y.-S. Tsai, *Pair Production and Bremsstrahlung of Charged Leptons*, Rev. Mod. Phys. **46** (1974) 815, [Erratum: Rev. Mod. Phys.49,521(1977)].

[61] M. Gupta, *Calculation of Radiation Length in Materials*, tech. rep., CERN, Geneva, Jul, 2010. PH-EP-Tech-Note-2010-013.

[62] P. A. M. Dirac, *The Quantum Theory of the Electron*, Proceedings of the Royal Society of London Series A **117** (1928) 610.

[63] J. W. Motz, A. Olsen, and H. W. Koch, *Pair Production by Photons*, Reviews of Modern Physics **41** (1969) 581, RevModPhys.41.581.

[64] H. Burkhardt, *examples/extended/electromagnetic/TestEm6 · master · geant4 / geant4*, Sep, 2018. `https://gitlab.cern.ch/geant4/geant4`.

[65] J. H. Christenson, J. W. Cronin, V. L. Fitch, and R. Turlay, *Evidence for the 2π Decay of the K_2^0 Meson*, Phys. Rev. Lett. **13** (1964) 138.

[66] A. Pich, *CP Violation*, `arXiv:hep-ph/9312297`, [ICTP Ser. Theor. Phys.10,14(1994)].

[67] Tabanashi, M and others (Particle Data Group), *CP Violation in the Quark Sector*, Phys. Rev. D **98** (2019), no. January 030001, Section 13.

[68] NA48, W. Wislicki, *Direct CP violation in neutral kaon decays*, Pramana **62** (2004) 601, `arXiv:hep-ex/0303037`.

[69] V. Cirigliano *et al.*, *Kaon Decays in the Standard Model*, Reviews of Modern Physics **84** (2012), no. 1 399, `arXiv:1107.6001`.

[70] N. H. Christ, X. Feng, A. Portelli, and C. T. Sachrajda, *Prospects for a Lattice Computation of Rare Kaon Decay Amplitudes $K \to \pi l^+ l^-$ Decays*, Physical Review D **93** (2016), no. 11 1, `arXiv:1605.04442`.

[71] G. D'Ambrosio, G. Ecker, G. Isidori, and J. Portolés, *The Decays $K \to \pi l^+ l^-$ Beyond Leading Order in the Chiral Expansion*, Journal of High Energy Physics **1998** (1998), no. 08 0, `arXiv:9808289`.

[72] B. Borasoy, *Introduction to Chiral Perturbation Theory*, Springer Proc. Phys. **118** (2008) 1, `arXiv:hep-ph/0703297`.

[73] S. Scherer, *Introduction to chiral perturbation theory*, Adv. Nucl. Phys. **27** (2003) 277, `arXiv:hep-ph/0210398`.

[74] G. D'Ambrosio, D. Greynat, and M. Knecht, *On the Amplitudes for the CP-Conserving $K^\pm(K_S) \to \pi^\pm(\pi^0)l^+ l^-$ Rare Decay Modes*, `arXiv:00735v1`.

[75] A. A. Alves Junior, M. O. Bettler, K. A. Zarebski *et al.*, *Prospects for Measurements with Strange Hadrons at LHCb*, JHEP **05** (2019) 048, `arXiv:1808.03477`.

[76] S. Friot and D. Greynat, *Long-Distance Contributions in $K \to \pi \ell^+ \ell^-$ Decays*, in *Proceedings, 40th Rencontres de Moriond on Electroweak Interactions and Unified Theories: La Thuile, Val d'Aoste, Italy, Mar 5-12, 2005*, pp. 399–404, 2005. `arXiv:hep-ph/0506018`.

[77] S. Friot, D. Greynat, and E. De Rafael, *Rare Kaon Decays Revisited*, Phys. Lett. **B595** (2004) 301, `arXiv:hep-ph/0404136`.

[78] E865, R. Appel *et al.*, *A New Measurement of the Properties of the Rare Decay $K^+ \to \pi^+ e^+ e^-$*, Phys. Rev. Lett. **83** (1999) 4482, `arXiv:hep-ex/9907045`.

[79] A. Z. Dubnickova *et al.*, *Kaon decay probe of the weak static interaction*, Phys. Part. Nucl. Lett. **5** (2008) 76, `arXiv:hep-ph/0611175`.

[80] NA48/2, J. R. Batley *et al.*, *New Measurement of the $K^+ \to \pi^+ \mu^+ \mu^-$ Decay*, Phys. Lett. **B697** (2011) 107, `arXiv:1011.4817`.

[81] T. Asaka, S. Blanchet, and M. Shaposhnikov, *The nuMSM, dark matter and neutrino masses*, Phys. Lett. **B631** (2005) 151, `arXiv:hep-ph/0503065`.

[82] D. Delepine, G. L. Castro, and N. Quintero, *Effects of heavy Majorana neutrinos in semileptonic heavy quark decays*, Journal of Physics: Conference Series **378** (2012) 012024.

[83] F. Dettori, D. Martinez Santos, and J. Prisciandaro, *Low-p_T Dimuon Triggers at LHCb in Run 2*, tech. rep., CERN, Geneva, Dec, 2017. LHCb-PUB-2017-023.

[84] M. Pivk and F. R. L. Diberder, *$_sPlot$: A Statistical Tool to unfold Data Distributions*, `arXiv:0402083arXiv:0402083`.

[85] K. Massri, *Kaon Identification and Search for Lepton Number Violation in $K^{\pm}$*

Decay-in-Flight Experiments at CERN, PhD thesis, University of Birmingham, 2014, eTheses Bham.

[86] A. Perieanu, *Identification of Ghost Tracks using Neural Networks*, tech. rep., CERN, Geneva, Jan, 2008. LHCb-2007-158. CERN-LHCb-2007-158.

[87] J. Therhaag, *TMVA - Toolkit for multivariate data analysis*, AIP Conference Proceedings **1504** (2012) 1013, `arXiv:0703039`.

[88] S. Robert E. *Explaining AdaBoost*, Empirical Inference: Festschrift in Honor of Vladimir N. Vapnik (2013) 37.

[89] A. Blum, A. Kalai, and J. Langford, *Beating the holdout: Bounds for kfold and progressive cross-validation*, in *COLT99*, January, 1999.

[90] A. Subtil and P. D. Z. Bermudez, *ROC CURVE ESTIMATION : AN OVERVIEW*, .

[91] M. Williams, V. Gligorov *et al.*, *The HLT2 Topological Lines*, Tech. Rep. LHCb-PUB-2011-002. CERN-LHCb-PUB-2011-002, CERN, Geneva, May, 2014.

[92] KLOE, F. Ambrosino *et al.*, *Measurement of the charged kaon lifetime with the KLOE detector*, JHEP **01** (2008) 073, `arXiv:0712.1112`.

[93] J. E. Gaiser, *Charmonium Spectroscopy From Radiative Decays of the J/ψ and ψ'*, PhD thesis, SLAC, 1982, SLAC-0255, UMI-83-14449-MC, SLAC-R-0255, SLAC-R-255.

[94] S. Das, *A Simple Alternative to the Crystal Ball Function*, `arXiv:1603.08591`.

[95] D. Martínez Santos and F. Dupertuis, *Mass distributions marginalized over per-event errors*, Nuclear Instruments and Methods in Physics Research,

Section A: Accelerators, Spectrometers, Detectors and Associated Equipment **764** (2014) 150, `arXiv:1312.5000`.

[96] CDF, F. Abe *et al.*, *Observation of the B_c meson in $p\bar{p}$ collisions at $\sqrt{s} = 1.8$ TeV*, Phys. Rev. Lett. **81** (1998) 2432, `arXiv:hep-ex/9805034`.

[97] M. Abazov *et al.*, *Observation of the B_c Meson in the Exclusive Decay $B_c \to J/\psi\,\pi$*, Physical review letters **101** (2008) 012001.

[98] CDF, T. Aaltonen *et al.*, *Measurement of the B_c^- meson lifetime in the decay $B_c^- \to J/\psi\,\pi^-$*, Phys. Rev. **D87** (2013), no. 1 011101, `arXiv:1210.2366`.

[99] LHCb, R. Aaij *et al.*, *Measurement of the lifetime of the B_c^+ meson using the $B_c^+ \to J/\psi\pi^+$ decay mode*, Phys. Lett. **B742** (2015) 29, `arXiv:1411.6899`.

[100] CMS, A. M. Sirunyan *et al.*, *Measurement of b hadron lifetimes in pp collisions at $\sqrt{s} = 8$ TeV*, Eur. Phys. J. **C78** (2018), no. 6 457, `arXiv:1710.08949`, [Erratum: Eur. Phys. J.C78,no.7,561(2018)].

[101] I. P. Gouz, V. V. Kiselev, A. K. Likhoded, and V. I. Romanovsky, *Prospects for the B_c Studies at LHCb*, `arXiv:0211432v1`.

[102] Z. J. Xiao and X. Liu, *The Two-Body Hadronic Decays of B_c meson in the Perturbative QCD approach: A Short Review*, Chinese Science Bulletin **59** (2014), no. 29-30 3748, `arXiv:1401.0151`.

[103] LHCb Collaboration, R. Aaij *et al.*, *Measurement of B_c^+ Production in Proton-Proton Collisions at $\sqrt{s} = 8$ TeV*, `1411.2943v`.

[104] Z. Rui and Z. T. Zou, *S-Wave Ground State Charmonium Decays of B_c Mesons in the Perturbative QCD Approach*, Physical Review D - Particles, Fields, Gravitation and Cosmology **90** (2014), no. 11 1, `arXiv:1407.5550`.

[105] S. Liao and J. Chen, *Object Recognition with Lower Order Gegenbauer Moments*, Lecture Notes on Software Engineering **1** (2013), no. 4 387.

[106] *Python Data Analysis Library*, Jan, 2019. `http://pandas.pydata.org`.

[107] LHCb, R. Aaij *et al.*, *Evidence for the rare decay* $\Sigma^+ \rightarrow p\mu^+\mu^-$, Phys. Rev. Lett. **120** (2018), no. 22 221803, `arXiv:1712.08606`.

[108] LHCb, R. Aaij *et al.*, *Opposite-side flavour tagging of B mesons at the LHCb experiment*, Eur. Phys. J. **C72** (2012) 2022, `arXiv:1202.4979`.

[109] J. Wishahi, *Schematic Overview of the Underlying Principles of LHCb's Flavour Tagging Algorithms*, Aug, 2016. Flavour Tagging Conference Plots.

[110] *TupleToolMCBackgroundInfo < LHCb < TWiki*, Dec, 2018. `https://twiki.cern.ch/twiki/bin/view/LHCb/TupleToolMCBackgroundInfo`.

Appendices

A.1 An Opposite-Side Tagger for K^0

In productions whereby two particles, one of which is a meson, are created via the pair production of a quark-antiquark pair tagging algorithms can be used to verify the identity of the meson. Algorithms which look directly at the daughters of this particle are known as Same-Side (SS) taggers. Alternatively tagging can be conducted through the measurement of the daughter particles of the other hadron, such procedures then being classed as Opposite-Side (OS) taggers [108].

In the analysis of B_s^0 mesons the technique of OS tagging is used to determine the flavour of the signal B_s^0. Electrons, muons and kaons within the decay chain of the other b-quark hadron are used to identify the particle. This example is illustrated in Figure A1.
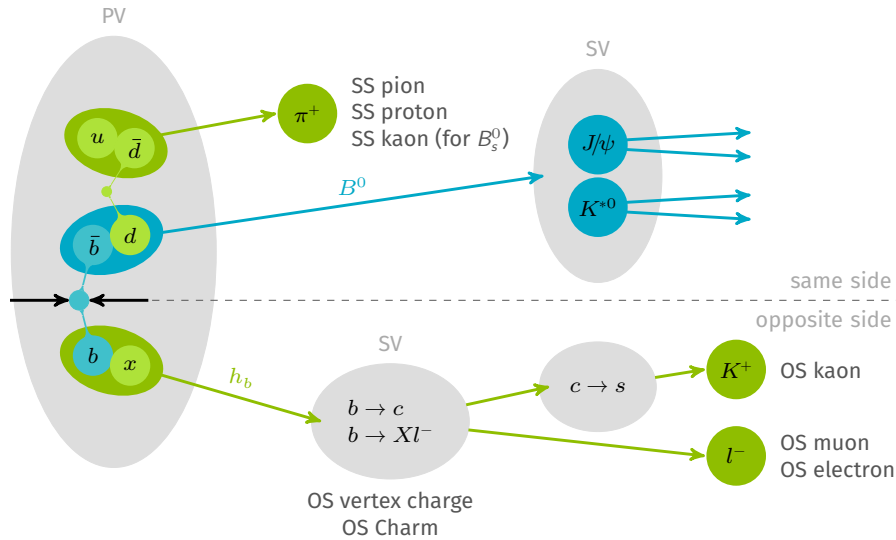
Figure A1: The Same-Side and Opposite-Side tagging of B^0 mesons at LHCb [109].

The aim of this investigation was to explore the prospects for a similar tagging procedure to distinguish between K^0 and $\bar{K}^0$ strange mesons. Using Pythia8 under the LHCb GAUSS environment, candidate channels for an OS tag were investigated via simulation of 2016 data from Run 2. Due to the lack of inclusive MC samples explicitly for strange decays (current software only allowing such productions for b

and c decays) minimum bias MC for 2016 was used in the search for candidates.

A selection was applied to events using DaVinci to obtain the decay tree of the other strange hadron produced alongside K^0 and $\bar{K}^0$ within each candidate event, with both cases being treated independently. Using the LoKi framework a description template for the desired event structure was constructed and imposed via the decay descriptors given in Table 1. The selections apply the further constraint that the other candidate cannot be another neutrally charged particle to ensure an OS tag is possible. From the minimum bias sample size of 24,290 events, a total of 36 combined K^0 and $\bar{K}^0$ decays were observed for interpretation.

Table 1: The decay descriptor used within DaVinci for selections of K^0 and $\bar{K}^0$.

K^0	`(X -> ^K0 ^(Xs -> ^X ^X {^X} {^X})) && ~(X -> K0 X0) && ~(X -> K~0 X0)`
$\bar{K}^0$	`(X -> ^K~0 ^(Xs -> ^X ^X {^X} {^X})) && ~(X -> K~0 X0) && ~(X -> K0 X0)`

A script was run over the candidates to obtain identification information for all the particles involved. The result was a charged 'sister' produced alongside K^0 decays of the $K^*(892)^+$ meson, these then decaying to pions or more kaons:

$$\bar{K}^0 \ (K^*(892)^+ \rightarrow \pi^+ ...) \tag{1}$$

$$\bar{K}^0 \ (K^*(892)^+ \rightarrow K^+ \pi^0) \tag{2}$$

these decays could indeed provide a means of identification, if the charge of the daughter $\pi^\pm / K^\pm$ is measured then the identity of the neutral kaon can be determined as either K^0 or $\bar{K}^0$.

A.2 $K^{\pm}$ Decay Vertices

Distributions for kaon decay vertices of long tracks were obtained using 2012 MC samples for $K^{\pm} \to \pi^{\pm}\pi^{+}\pi^{-}$. The plots in Figure A2 show hitmaps of the vertex locations in the x, y and z planes. Also evident as staggered lines with low hit rate are the VELO planes.

(a) X Projection

(b) Y Projection

(c) Z Projection
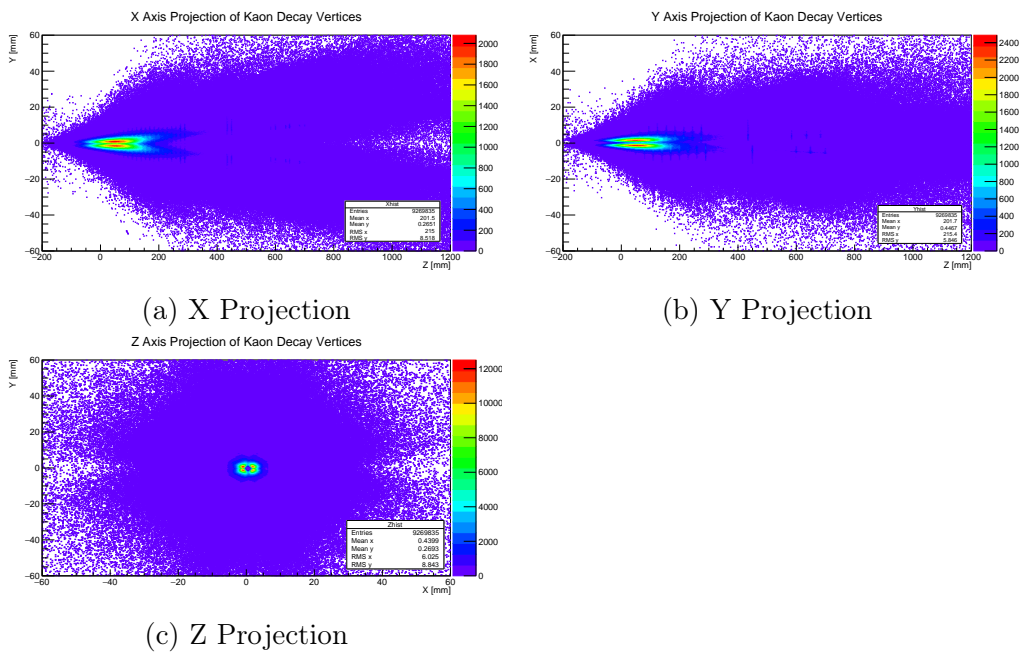
Figure A2: Long tracks charged kaon decay vertices within LHCb.

A.3 $K^{\pm}$ Transverse Momentum

Distribution of the longitudinal momentum of the $K^{\pm}$ in $K^{\pm} \rightarrow \pi^{\pm}\mu^{+}\mu^{-}$ 2016 Stripping28 MC is shown in Figure A3. The average of $\sim 22\,\mathrm{GeV}$ is used for the calculation of $\beta\gamma c\tau$ for kaon flight distance in LHCb.
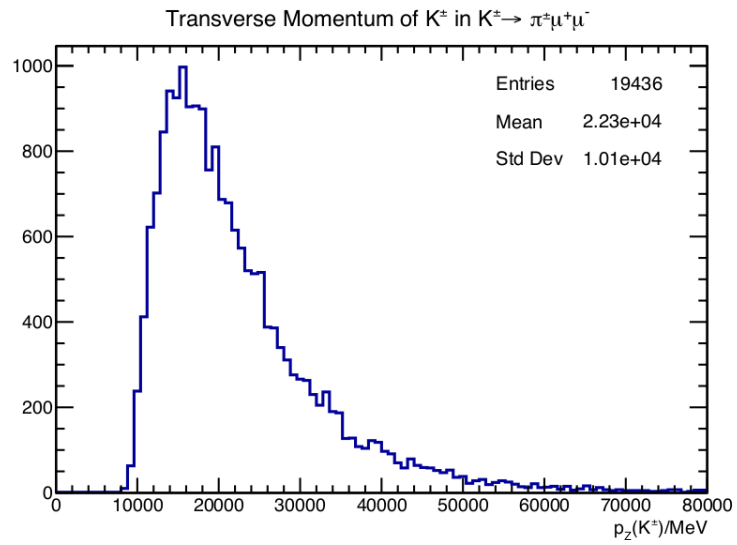
Figure A3: Histogram showing the distribution of longitudinal momentum of the $K^{\pm}$ using 2016 Stripping28 MC.

A.4   Background Information

One of the tools which can be included when processing MC with DaVinci is *TupleToolMCBackgroundInfo* which categorises events based on their source and is useful for studying candidate channels. A tool, unofficially named *MCTruthReader*, was written to scan the events contained within various MC samples including *b*-inclusive, *c*-inclusive, and minimum bias under the $K^{\pm} \to \pi^{\pm}\pi^{+}\pi^{-}$ selection. In addition to returning the category number the decay sequence was also determined. The process of reconstructing the decay chains was carried out using truth information including particle ID and the mother key of the particles, where the mother key is a unique identifier for a given particle species. A sample of results from the scan are given in Table 2. The majority of events are category 60, these contain at least one particle which has been mistaken to be part of the event but is actually due to effects within the detector material, these are known within LHCb as 'ghost' events. The other dominant type is category 40, the label given to partially reconstructed backgrounds [110].

The tool is run as as a ROOT macro:

```
root [0] .L readMCTruth.cc+
root [1] MCTruthReader reader("/disk/file/data.root","Tuple/DecayTree","K_plus",{"pion","piplus","piminus"})
(MCTruthReader &) @0x7fbb4a794048
root [2] reader.readMCTruth()
Extracting Mother & Daughter Information...
Will examine: Kplus -> pion piplus piminus
Decay: 0      ANCESTRY(0->0->0->)      0   ->      pi+    0      pi-    Category: 60
Decay: 1      ANCESTRY(0->0->0->)      0   ->      pi-    0      e+     Category: 60
Decay: 2      ANCESTRY(0->0->0->)      0   ->      pi+    K+     0      Category: 60
Decay: 3      ANCESTRY(0->0->0->)      0   ->      0      pi-    K+     Category: 60
```

It should be noted that during reviews of the performance of TupleToolMCBackgroundInfo by LHCb results are often shown to be inaccurate, and so in the case of this investigation only a prediction for the dominant background categories has been

Table 2: Results of running the *MCTruthReader* macro on samples of MC under $K^{\pm} \to \pi^{\pm}\pi^{+}\pi^{-}$ selection. Shown are the identified decay chains with the 'ancestors' of the parent particle from these chains listed under ANCESTRY. The categories have been obtained using TupleToolMCBackgroundInfo.

			b-inclusive MC 2011 and 2012						
Decay:	0	ANCESTRY(0->0->0->)	0	->	0	0	pi+	Category:	60
Decay:	1	ANCESTRY(0->0->0->)	0	->	0	0	pi-	Category:	60
Decay:	2	ANCESTRY(0->0->0->)	0	->	0	0	e-	Category:	60
Decay:	3	ANCESTRY(0->0->0->)	0	->	pi+	pi+	0	Category:	60
Decay:	4	ANCESTRY(0->0->0->)	0	->	pi-	pi-	pi+	Category:	70
Decay:	5	ANCESTRY(0->0->0->)	0	->	pi-	pi-	pi+	Category:	120
Decay:	6	ANCESTRY(0->0->0->)	0	->	pi-	pi-	pi+	Category:	100
Decay:	7	ANCESTRY(0->0->0->)	0	->	0	pi-	pi+	Category:	60
Decay:	8	ANCESTRY(0->0->0->)	0	->	pi+	0	0	Category:	60
Decay:	9	ANCESTRY(0->0->0->)	0	->	0	pi+	pi-	Category:	60
Decay:	10	ANCESTRY(0->0->0->)	0	->	0	pi+	pi-	Category:	60
Decay:	11	ANCESTRY(0->B*_2+->B*0->)	B0	->	pi-	K-	pi+	Category:	40
Decay:	12	ANCESTRY(0->0->0->)	0	->	0	pi+	pi-	Category:	60
			c-inclusive MC 2010						
Decay:	0	ANCESTRY(0->0->0->)	0	->	pi+	pi+	pi-	Category:	70
Decay:	1	ANCESTRY(0->0->0->)	0	->	pi-	pi-	pi+	Category:	100
Decay:	2	ANCESTRY(0->0->0->)	0	->	pi+	0	pi-	Category:	60
Decay:	3	ANCESTRY(0->0->0->)	0	->	pi-	pi-	p+	Category:	100
Decay:	4	ANCESTRY(0->0->0->)	0	->	e-	pi-	pi+	Category:	100
Decay:	5	ANCESTRY(0->0->0->)	0	->	pi+	pi+	0	Category:	60
Decay:	6	ANCESTRY(0->0->0->)	0	->	0	0	pi-	Category:	60
Decay:	7	ANCESTRY(0->0->0->)	0	->	pi+	0	pi-	Category:	60
Decay:	8	ANCESTRY(0->0->0->)	0	->	0	pi-	e+	Category:	60
Decay:	9	ANCESTRY(0->0->0->)	0	->	pi-	pi-	pi+	Category:	80
Decay:	10	ANCESTRY(0->0->0->)	D*(2010)+	->	pi+	e+	pi-	Category:	40
Decay:	11	ANCESTRY(0->0->0->)	0	->	pi+	0	pi-	Category:	60
Decay:	12	ANCESTRY(0->0->0->)	0	->	pi-	pi-	pi+	Category:	80
			Minimum Bias MC 2011 and 2012						
Decay:	0	ANCESTRY(0->0->0->)	0	->	0	pi+	0	Category:	60
Decay:	1	ANCESTRY(0->0->0->)	0	->	K-	pi-	pi+	Category:	110
Decay:	2	ANCESTRY(0->0->0->)	0	->	0	pi-	0	Category:	60
Decay:	3	ANCESTRY(0->0->0->)	0	->	0	pi-	0	Category:	60
Decay:	4	ANCESTRY(0->0->0->)	0	->	pi+	pi+	pi-	Category:	70
Decay:	5	ANCESTRY(0->0->0->)	0	->	pi+	0	pi-	Category:	60
Decay:	6	ANCESTRY(0->0->0->)	0	->	0	0	0	Category:	60
Decay:	7	ANCESTRY(0->0->0->)	anti-b	->	K-	pi-	pi+	Category:	40
Decay:	8	ANCESTRY(0->0->anti-b->)	B0	->	pi-	e-	pi+	Category:	40
Decay:	9	ANCESTRY(0->0->0->)	0	->	pi-	0	0	Category:	60
Decay:	10	ANCESTRY(0->0->0->)	anti-b	->	pi+	pi+	p -	Category:	40
Decay:	11	ANCESTRY(0->0->0->)	b	->	pi+	pi+	pi-	Category:	40
Decay:	12	ANCESTRY(0->b->B* 0->)	B 0	->	pi-	pi-	pi+	Category:	40

deduced and not the relative proportions of these categories. The study simply acted as a means of validating further the methods used within the analysis.

A.5 Trigger Line Cuts

Hlt1DiMuonNoL0	
Vertex DOCA	< 0.2
Vertex χ^2	< 25
$p(\mu^+\mu^-)$	$> 3\,\text{GeV}$
IP	< 0.4
Track χ^2/ndf	< 4
$M_{\mu^+\mu^-}$	> 0
Mass of Reco. Vertex	$> 220\,\text{MeV}$
IPχ^2	> 9
$p_T(\mu^+\mu^-)$	$> 80\,\text{MeV}$
Hlt1DiMuonLowMass	
Vertex DOCA	< 0.2
Vertex χ^2	< 25
$p(\mu^+\mu^-)$	$> 6\,\text{GeV}$
Track χ^2/ndf	< 4
$M_{\mu^+\mu^-}$	$> 1\,\text{GeV}$
Mass of Reco. Vertex	$> 220\,\text{MeV}$
IPχ^2	> 9
$p_T(\mu^+\mu^-)$	$> 200\,\text{MeV}$
Hlt1TrackMVA	
p_T	$[1,25]\,\text{GeV}$
IPχ^2	> 7.4
Track χ^2	< 2.5
Track Ghost Probability	< 0.2

Hlt1TwoTrackMVA	
p_T	$>500\,\mathrm{MeV}$
p	$>5\,\mathrm{GeV}$
Track χ^2/ndf	<2.5
IPχ^2	$>4\,\mathrm{mm}$
η	[2,5]
DIRA Angle	>0
M_{corr}	$[1,10^6]\,\mathrm{GeV}$
Combination p_T	$>2\,\mathrm{GeV}$
Vertex χ^2	<10
'MatrixNet' Classifier Threshold	>0.95
Classifier Variables	Vertex χ^2
	χ^2-distance from Primary Vertex
	$\sum_i p_{Ti}$ of Basic Particles
	No. Particles with IP$\chi^2<16$
Hlt1TrackMuon	
p_T	$>570\,\mathrm{MeV}$
p	$>5.7\,\mathrm{GeV}$
Track χ^2/ndf	<3
IPχ^2	>7.4
Hlt1TrackAllL0	
p_T	$>1.8\,\mathrm{GeV}$
p	$>10\,\mathrm{GeV}$
Track χ^2/ndf	<3
IP	$<0.1\,\mathrm{mm}$
IPχ^2	>16
Track χ^2/ndf	<3
No. VELO Hits	>9
No. Tracks Missing VELO	<3

Hlt2DiMuonSoft	
Track χ^2	< 10
$M_{\mu^+\mu^-}$	$[0,1]\,\mathrm{GeV}$
IP	$> 0.3\,\mathrm{mm}$
IPχ^2	$[9, 10^{12}]$
Track Ghost Probability	< 0.4
μ ProbNNμ	> 0.05
μ ID	IsMuon
Vertex χ^2	< 25
$\rho = \sqrt{\delta x^2 + \delta y^2}$	$> 3\,\mathrm{mm}$
δz	$< 650\,\mathrm{mm}$
$\mu^+\mu^-$ DOCA	$< 0.3\,\mathrm{mm}$
$\theta_{\mu^+\mu^-}$	$> 2\,\mathrm{mrad}$
IP$_{\mu^+\mu^-}/\delta z$	$< 1/60$
Hlt2RareStrangeKPiMuMu	
Track χ^2/ndf	< 3
Track Ghost Probability	< 0.3
μ IPχ^2	> 25
μ ID	IsMuon
$\pi^\pm$ IPχ^2	> 25
$K^\pm$ DOCA	$< 2\,\mathrm{mm}$
$p_T(K^\pm)$	$< 500\,\mathrm{MeV}$
$K^\pm$ Vertex χ^2	< 25
IPχ^2 $(K^\pm)$	< 36
$K^\pm$ DIRA Angle	> 0.9
$\tau(K^\pm)$	$> 10\,\mathrm{ps}$
$\Delta M_{K^\pm}$	$500\,\mathrm{MeV}$
Hlt2Topo2BodyBBDT and Hlt2Topo3BodyBBDT (Run 1)	
p_T	$> 500\,\mathrm{MeV}$
p	$> 5\,\mathrm{GeV}$
Track χ^2/ndf	< 2
IPχ^2	> 16
DOCA	< 0.2
χ^2-distance	> 100
M	2-Body $[2.5,7]\,\mathrm{GeV}$
	3-Body $[3, 7]\,\mathrm{GeV}$
$\sum_i p_{T_i}$	2-Body $> 7\,\mathrm{GeV}$
	3-Body $> 8\,\mathrm{GeV}$
Flight Distance χ^2	> 1000
Classifier Threshold	> 0.4
Classifier Variables	M
	DOCA
	IPχ^2
	M_{corr}
	χ^2-distance
	p_T
	Minimum p_T of Decay Tree
	$\sum_i p_{T_i}$ Decay Tree

Hlt2Topo2Body and Hlt2Topo3Body (Run 2)	
p_T	$>\ 200\,\text{MeV}$
p	$>\ 3\,\text{GeV}$
Track χ^2/ndf	$<\ 4$
IPχ^2	$>\ 16$
l^+l^- ProbNNl	$>\ 0.1$
M_{corr}	$[1,\ 10]\,\text{GeV}$
Track χ^2/ndf	$<\ 3$
τ	$>\ 0\,\text{ps}$
Combined η	$[2,\ 5]$
Vertex χ^2	$<\ 1000$
χ^2-distance	$>\ 16$
Classifier Threshold	2-Body $>\ 0.997$
	3-Body $>\ 0.995$
Classifier Variables	No. Particles $(K^{\pm}\ \vert\ K_s^0\ \vert\ \Lambda_0)$
	M_{corr}
	Vertex χ^2
	$\sum_i p_{T_i}(K^{\pm}\vert K_s^0\vert\Lambda_0)$
	η
	Flight Distance χ^2
	$\text{Min}(p_T(K^{\pm}\vert K_s^0\vert\Lambda_0))$
	No. $K^{\pm}$ with IP$\chi^2 <\ 16$